Transverse momentum spectra and cross sections of charged particles in pp collisions measured with ALICE

Dissertation
zur Erlangung des Doktorgrades
der Naturwissenschaften

vorgelegt beim Fachbereich Physik
der Johann Wolfgang Goethe-Universität
in Frankfurt am Main

von
Edgar Pérez Lezama
aus Tehuacán, México

Frankfurt am Main (2018)
(D 30)

Vom Fachbereich Physik der Johann Wolfgang Goethe-Universität
als Dissertation angenommen.

Dekan: Prof. Dr. Michael Lang

Gutachter: Prof. Dr. Alberica Toia
                                Prof. Dr. Henner Büsching

Datum der Disputation: 13er Juni 2019

Abstract

The production cross section and the transverse momentum distribution of charged particles is measured in pp collisions at $\sqrt{s} = 2.76$ TeV, 5.02 TeV, 7 TeV and 13 TeV, as well as for Pb-Pb collision at $\sqrt{s_{NN}} = 5.02$ TeV and Xe-Xe at $\sqrt{s_{NN}} = 5.44$ TeV in ALICE at the LHC. The measurement is performed in the transverse momentum region of $0.15 < p_T < 50$ GeV/c and in the pseudorapidity range of $|\eta| < 0.8$. The precision of the measurement has been substantially enhanced as a result of the improved corrections, by taking into account a more realistic particle composition in the MC simulations. As a result, the systematic uncertainties have been reduced by more than a factor two in all systems and energies.

The average transverse momentum $\langle p_T \rangle$ results show a faster-than-linear increase with the center-of-mass energy and follow a similar trend with respect to previous measurements. The analysis of the p_T spectra in multiplicity intervals show a weak center-of-mass energy dependence when they are compared to their respective inelastic (INEL) pp measurement. The average multiplicity as a function of the collision energy shows a quadratic trend, and the comparison with other ALICE multiplicity measurements exhibits a remarkable agreement, within uncertainties.

The transverse momentum spectra in pp collisions are compared to state-of-the-art MC simulations, EPOS LHC and PYTHIA 8 event generators; none of them is able to reproduce the distributions over the full p_T range.

The differential cross section in pp collisions is an essential observable for the study of the Quark Gluon Plasma (QGP) created in ultra-relativistic heavy-ion collisions. The absence of a medium formation in pp collisions serves as an essential baseline for studies of particle production and suppression due to parton energy-loss in the QGP. Since pp collisions at $\sqrt{s} = 5.44$ TeV were not measured by ALICE, the pp reference at this energy was constructed by using a power law interpolation between the $\sqrt{s} = 5.02$ TeV and 7 TeV data. The pp results are compared to the particle production in Pb-Pb collisions at $\sqrt{s} = 5.02$ TeV and Xe-Xe collisions at $\sqrt{s_{NN}} = 5.44$ TeV.

The nuclear modification factor R_{AA} for Pb-Pb and Xe-Xe collisions was calculated and a strong suppression of high-p_T particles is observed in central collisions. The R_{AA} in different systems allows for a differential study of the parton energy loss in the QGP. The comparison of the R_{AA} in multiplicity intervals between the two systems provide insights into the path length dependence of a parton that propagates in the medium.

Zusammenfassung

Einleitung

Die Quantenchromodynamik (QCD) ist die fundamentale Theorie stark wechselwirkender Teilchen, die die Existenz einer Phase freier Quarks und Gluonen vorhersagt, das sogenannte Quark-Gluon-Plasma (QGP). Das QGP existierte im frühen Universum einige Mikrosekunden nach dem Urknall. Experimentell kann es für eine kurze Zeitperiode in relativistischen Schwerionenkollisionen erzeugt werden. Nach der initialen Kollision befinden sich die Quarks und Gluonen in einer Vor-Gleichgewichtsphase, die $\tau \sim 3\,\text{fm}/c$ andauert. Das QGP formt sich nach der Vor-Gleichgewichtsphase und existiert für ungefähr $3 < \tau < 6\,\text{fm}/c$. Die Temperatur des Systems fällt aufgrund der Expansion des Mediums ab und die Quarks und Gluonen binden sich zu farbneutralen Hadronen. Diese werde später in den Experimenten detektiert.

Es gibt zahlreiche Observablen, die Informationen über die Parameter des QGP liefern können. Eine dieser Observablen die als Signatur des QGP gilt, ist das sogenannte "Jet-Quenching" welches ursprünglich von Bjorken vorgeschlagen. Jet-Quenching beschreibt die Abschwächung oder das komplette Verschwinden von Hadronen, als Konsequenz des Medium-induzierten partonischen Energieverlusts. Der Energieverlust ΔE eines Teilchens im Medium liefert wichtige Informationen über die Eigenschaften des Plasmas. ΔE hängt von der Energie E, der Masse m und der Ladung des Teilchens ab dass das Plasma durchquert, sowie von den Eigenschaften des Plasmas: Temperatur T, Teilchen-Wechselwirkungs-Kopplung α und Dicke L.

Experimentell kann der partonische Energieverlust durch die Unterdrückung von Jets und Teilchen mit hohem Transversalimpuls (p_{T}) im Medium untersucht werden. Die Unterdrückung von Teilchen wird mit dem nuklearen Modifikationsfaktor R_{AA} charakterisiert, welcher definiert ist als das Verhältnis zwischen den Teilchenspektren in Kern-Kern-Kollisionen (QCD-Medium) und in pp-Kollisionen (QCD-Vakuum). Für einen fairen quantitativen Vergleich, wird der pp Wirkungsquerschnitt mit der nuklearen Überlappfunktion T_{AA} skaliert. Diese ist proportional zur Zahl der Nukleon-Nukleon-Kollisionen und umgekehrt proportional zum inelastischen Wirkungsquerschnitt einer Nukleon-Nukleon-Kollision: $T_{\text{AA}} = N_{\text{coll}}/\sigma_{\text{inel}}^{\text{NN}}$. Sie wird mit dem Glauber-Modell berechnet. Der nukleare Modifikationsfaktor ist definiert als $R_{\text{AA}} = \frac{\mathrm{d}^2 N_{\text{ch}}^{\text{PbPb}}}{\mathrm{d}\eta\mathrm{d}p_{\text{T}}}/(\langle T_{\text{AA}}\rangle \times \frac{\mathrm{d}^2 \sigma_{\text{ch}}^{\text{pp}}}{\mathrm{d}\eta\mathrm{d}p_{\text{T}}})$. Bei nicht vorhandener Abschwächung von Teilchen mit hohem Transversalimpuls ist der nukleare Modifikationsfaktor gleich eins.

Andererseits, wenn im Vergleich zum pp-Spektrum weniger Teilchen in Kern-Kern-Kollisionen gemessen werden, signalisiert ein $R_{\text{AA}} < 1$ das Vorhandensein einer Teilchenunterdrückung. Der R_{AA} beinhaltet nicht nur Unterdrückungseffekte, sondern zusätzlich Effekte durch Strahlung im Anfangs- und Endzu-

stand der Kollision. Der nukleare Modifikationsfaktor gemessen in Proton-Nukleus-Kollisionen kann helfen, diese Effekte von denen der Teilchenunterdrückung zu unterscheiden.

Das Transversalimpuls-Spektrum geladener Teilchen in pp-Kollisionen ist eine wichtige Observable zum Testen von perturbativer QCD, zum Tunen phänomenologischer Modelle, und dient als Referenzgröße für die Untersuchung der Teilchenunterdrückung in Schwerionenkollisionen. Bevor die Ergebnisse der LHC-Experimente vorlagen wurde angenommen, dass das QGP nur in "großen" Systemen so wie jenen in Schwerionenkollisionen, erzeugt werden kann. In "kleinen" Systemen, so wie jenen in Proton-Proton und Proton-Kern-Kollisionen, wurden keine kollektiven Effekte erwartet. Die experimentellen Ergebnisse jedoch zeigten die Existenz des kollektiven Flusses in kleinen Systemen. Das Studium weitreichender azimuthaler Zweiteilchenkorrelationen über einen weiten Pseudorapiditätsbereich in pp-Kollisionen mit hoher Teilchenmultiplizität liefert Informationen über die Dynamik der Teilchenerzeugung in kleinen und dichten QCD-Systemen. Ergebnisse des CMS-Experiments zeigten, dass Zweiteilchen-Korrelationsfunktionen einen Pseudorapiditätsbereich von $|\eta| \approx 4$ überspannen. Dieser Effekt wird als "Ridge" bezeichnet. Der Ridge wurde zuerst in Cu-Cu und Au-Au-Kollisionen am RHIC und Pb-Pb-Kollisionen am LHC beobachtet. Es wurde geschlussfolgert, dass der hydrodynamische kollektive Fluss eines stark wechselwirkenden und sich ausbreitenden Mediums für die weitreichenden Korrelationen verantwortlich ist.

ALICE

Der Large Hadron Collider des CERN erreicht die höchsten Kollisionsenergien aller bisherigen Teilchenbeschleuniger und liefert den Experimenten seit seiner Inbetriebnahme Proton-Proton (pp), Blei-Blei (Pb-Pb) und Xenon-Xenon (Xe-Xe) Kollisionen. Das ALICE-Experiment ist auf das Studium von QGP in Pb-Pb und Xe-Xe-Kollisionen konzentriert, misst aber auch pp- und p-Pb-Kollisionen. Die pp-Kollisionen dienen dabei als wichtige Referenzmessung um nukleare Effekte in p-Pb- und Pb-Pb-Kollisionen zu untersuchen. Darüber hinaus, lassen sich Vorhersagen von störungstheoretischer QCD und Monte-Carlo-Modellen überprüfen. Messungen in Pb-Pb-Kollisionen ermöglichen es die Mechanismen des Energieverlusts zu untersuchen und das QGP zu charakterisieren.

Der Silizium-Detektor ITS (Inner Tracking System) ist der innerste Detektor von ALICE. Er besteht aus sechs zylindrischen Lagen positionssensitiver Detektoren, die für Kollisionen mit einem Interaktionsvertex innerhalb von 10 cm entlang der Strahlachse (z) eine Akzeptanz von $|\eta| < 0.9$ bis $|\eta| < 2$ abdecken. Die für die inneren Lagen notwendige hohe Auflösung und Präzision wird mittels mikrostrukturierter Detektoren aus Silizium mit zweidimensionaler Auslese erreicht. Die ersten beiden Lagen bilden den Silizium-Pixel-Detektor (SPD), die folgenden zwei den Silizium-Drift-Detektor (SDD). Bei großen Radien zum Interaktionspunkt ist eine weniger hohe Auflösung nötig, weswegen zwei Lagen Silizium-Streifen-Detektoren (SSD) benutzt werden.

Die Spurendriftkammer TPC (Time Projection Chamber) ist der Haupt-Spurfindungsdetektor des zentralen Teils des ALICE-Detektors liefert, zusammen mit dem ITS und den anderen zentralen Detektoren, eine Messung des Impuls geladener Teilchen mit guter Separation von Spuren, Teilchenidentifikation und Vertexbestimmung. Die TPC ist ein zylindrischer Detektor mit einem inneren Radius von 80 cm und einem äußeren Radius von ungefähr 250 cm und einer Länge von 500 cm in

Strahlrichtung. Um mehrfache Streuung und Sekundärteilchen-Produktion zu minimieren, ist die Materialbelegung der TPC so gering wie möglich (3% X_0 um $\eta = 0$). Beim Durchgang durch den Detektor ionisieren geladene Teilchen das Gas. Durch das elektrische Feld driften Elektronen zu den Endkappen des Detektors, wo ihre Ankunftsposition auf der präzise gemessen wird. Durch Kombination dieser Information mit der akkuraten Messung der Ankunftszeit kann die komplette Trajektorie im Raum für alle die TPC durchquerenden geladenen Teilchen präzise bestimmt werden.

Der V0-Detektor ist ein Kleinwinkeldetektor bestehend aus zwei Szintillator-Arrays, die sich auf beidem Seiten des Kollisionspunkts von ALICE befinden, V0A und V0C. Der V0A-Detektor befindet sich 330 cm vom Kollisionspunkt in positiver z-Richtung (gegenüber dem Myon-Spektrometer). Der V0C ist an der Vorderseite des Hadronenabsorbers fixiert, 90 cm vom Kollisionspunkt. Die Rapiditätsbereiche sind $2.8 > \eta > 5.1$ für den V0A und $-3.7 < \eta < -1.7$ für den V0C. Die V0-Detektoren erfüllen verschiedene Funktionen. Während der Datennahme liefern sie den zentralen Detektoren einen Minimum-Bias-Trigger (MB), einen Multiplizitäts-Trigger (MT), einen Trigger auf semizentrale (CT1), sowie auf zentrale Kollisionen (CT2) in pp und Kern-Kern-Kollisionen (V0-AND Modus). Der V0-Detektor kann außerdem p-Gas-Trigger (PG) bereitstellen, für Interaktionen zwischen Strahlteilchen mit dem Restgas in der Vakuumkammer. In pp-Kollisionen beträgt die Effizient des V0, auf beiden Seiten zumindest ein geladenes Teilchen zu detektieren ungefähr 84$. Ferner nimmt der V0-Detektor an der Luminitätsmessung mit einer Präzision von besser als 10% teil.

Analyse

Die Analyse basiert auf primäre geladene Teilchen, die ein Signal in der TPC und im ITS hinterlassen, welche in pp-Kollisionen bei $\sqrt{s}$ = 2.76 TeV, 5.02 TeV, 7 TeV und 13 TeV gemessen wurden. In ALICE wurde eine Reihe von Spurauswahlkriterien entwickelt, um Spuren primärer Teilchen der besten Qualität zu selektieren. Um vollständig korrigierte Transversalimpuls-Spektren zu erhalten, müssen die Roh-Verteilungen auf verschieden Aspekte korrigiert werden: Detektor-Ineffizienzen, Kontaminierung mit Sekundärteilchen und die p_T-Auflösung.

Die Korrektur der Rekonstruktionseffizienz primärer Teilchen basiert auf Monte-Carlo-Informationen von Simulationen mit Hilfe des PYTHIA-Ereignis-Generators. Die Spurfindungseffizienz für die oben definierten Kollisions-energien ist im Bereich von 60-70%. Es ist bekannt, das MC-Generatoren den Hauptteil der Erzeugung (bei niedrigen Impulsen) der einzelnen Teilchensorten nicht gut beschreiben, insbesondere wird die Hyperon-Erzeugung erheblich unterschätzt. Die Korrektur der Teilchenzusammensetzung benutzt Messungen der Produktion geladener Pionen, Kaonen, Protonen und Lambda-Baryonen (als Proxy für geladene Hyperonen) um deren Mengen in Daten zu bestimmen. Die Spurfindungseffizienz wird dann bestimmt, indem die Zusammensetzung der primären Teilchen neu gewichtet wird. Der Korrekturfaktor ist bei $p_T \approx 2.5\,\mathrm{GeV}/c$ am größten, hauptsächlich aufgrund der Sigma-Hyperonen, da bei diesen Impulsen die Anteile die größte Diskrepanz zu denen aus den MC-Generatoren zeigen. Der maximale Korrekturfaktor für pp-Kollisionen bei $\sqrt{s} = 13$ TeV, 7 TeV, 5.02 TeV und 2.76 TeV ist jeweils 8%, 3%, 6% und 5%.

Sekundärteilchen sind definiert als Teilchen aus dem schwachen Zerfall von Kaonen, Λ-Hyperonen

und Myonen, sowie Teilchen, die aus der Wechselwirkung mit dem Detektormaterial stammen. Die mit den Spurauswahlkriterien selektierten Teilchen enthalten nicht nur Primärteilchen. Einige Sekundärteilchen verbleiben und müssen aus den Datensätzen subtrahiert werden.

Ein erheblicher Anteil der Sekundärteilchen aus schwachen Zerfällen kommt aus dem Zerfall ungeladener seltsamer Teilchen, wie K^0 oder Λ. Da die MC-Ereignis-Generatoren die Erzeugung seltsamer Teilchen unterschätzen, wird der Anteil primärer und sekundärer Teilchen mit Hilfe der Verteilung des transversalen Abstands nächster Annäherung (DCA_{xy}) von Teilchen in Daten und Monte-Carlo-Simulationen abgeschätzt. Es wird dabei angenommen, dass die DCA_{xy}-Verteilung primärer und sekundärer Teilchen verschiedene Formen haben, insbesondere an den Rändern da Sekundärteilchen aus Zerfällen und Wechselwirkungen mit dem Detektormaterial nicht an der Position des primären Interaktionspunkts entstehen und dadurch eine breitere DCA_{xy}-Verteilung haben. Die Korrekturfaktor unterscheiden sich nicht stark in pp-Kollision bei $\sqrt{s}$ = 13 TeV, 7 TeV und 5.02 TeV. Sie haben Werte zwischen 1.2 bei niedrigem p_T und 1.6 bei $p_\mathrm{T} > 1\,\mathrm{GeV}/c$. Der größten Korrekturen treten in pp-Kollisionen bei $\sqrt{s}$ = 2.76 TeV auf mit Werten zwischen 1.5 bei niedrigem p_T und 1.9 oberhalb $1\,\mathrm{GeV}/c$.

Die Messung der p_T-Verteilungen bei sehr großen Impulsen erfordert eine Korrektur der p_T-Auslösung, da der Transversalimpuls geladener Teilchen aus der Krümmung der Spuren in dem ITS und der TPC rekonstruiert wird. Mit zunehmendem p_T wird die Krümmung gerader. Für Spuren mit geringem Transversalimpuls ($p_\mathrm{T} < 1\,\mathrm{GeV}/c$) ist die Auflösung durch Mehrfachstreuung dominiert, zwischen den Datensätzen ist kein signifikanter Unterschied zu erwarten. Die Auflösung hat ihren optimalen Werte von $\sigma(p_\mathrm{T})/pt \approx 1\%$ bei $p_\mathrm{T} = 1\,\mathrm{GeV}/c$. Bei höheren Impulsen verschlechtert sich die Auflösung und nimmt für $p_\mathrm{T} = 50\,\mathrm{GeV}/c$ Werte zwischen 3 und 4% an.

Ergebnisse

Die differentiellen Wirkungsquerschnitte geladener Teilchen werden für inelastische pp-Kollisionen bei $\sqrt{s}$ = 2.76 TeV, 5.02 TeV, 7 TeV und 13 TeV in der Akzeptanzregion $|\eta| < 0.8$ im Transversalimpulsbereich $0.15\,\mathrm{GeV}/c < p_\mathrm{T} < 50\,\mathrm{GeV}/c$ gemessen. Die Messungen stimmen innerhalb der systematischen Unsicherheiten mit publizierten Ergebnissen überein. Der größte Unterschied ist geringer als 10% bei ungefähr $1\,\mathrm{GeV}/c < p_\mathrm{T} < 4\,\mathrm{GeV}/c$. Der Unterschied rührt her von der Korrektur der Teilchenzusammensetzung, die in diesem Transversalimpulsbereich stark durch Λ-Hyperonen beeinflusst ist. Die Transversalimpuls-Spektren werden für alle Kollisionsenergien mit Erwartungen von den EPOS und PYTHIA MC-Generatoren verglichen; Keiner von beidem gibt die Spektrumsform über den gesamten p_T-Bereich korrekt wider. Die Verhältnisse der Transversalimpuls-Spektren geladener Teilchen bei verschiedenen Kollisionsenergien, sowie die der zugehörigen Spektren aus den MC-Simulationen werden berechnet. Die Verhältnisse von $\sqrt{s}$ = 5.02 TeV zu 2.76 TeV, sowie von $\sqrt{s}$ = 13 TeV zu 7 TeV zeigt eine signifikante Verhärtung der Spektren. In erstem Fall ist das Verhältnis zwischen 2.5 und 3 für $p_\mathrm{T} > 10\,\mathrm{GeV}/c$, während es in letzterem bei einem Wert von 2 stagniert. Die EPOS-LHC und PYTHIA 8 MC-Generatoren beschreiben den beobachteten Verhärtungs-Trend über den gesamten untersuchten p_T-Bereich.

Der mittleren Transversalimpuls $\langle p_\mathrm{T} \rangle$ für inelastische pp-Kollisionen für die einzelnen Kollisionsen-

ergien wurde aus den Transversalimpuls-Spektren berechnet.Die modifizierte Hagedorn-Funktion wurde benutzt um das Transversalimpuls-Spektrum zu fitten, und um den Bereich $p_\mathrm{T} < 0.15\,\mathrm{GeV}/c$ zu ergänzen. Ein zunehmender Trend von $\langle p_\mathrm{T}\rangle$ als Funktion von $\sqrt{s}$ wurde beobachtet. Die Ergebnisse sind etwas höher als vorherige Messungen in pp- und $\mathrm{p}\overline{\mathrm{p}}$-Kollisionen der gleichen Energie in einem größeren η-Bereich. Die PYTHIA-Simulationen stimmen mit den experimentellen Daten innerhalb der Unsicherheiten nur für $\sqrt{s} = 2.76$ TeV und 5.02 TeV überein; bei den höheren Kollisionsenergien wird $\langle p_\mathrm{T}\rangle$ klar überschätzt. EPOS zeigt ein anderes Verhalten: die Werte von $\langle p_\mathrm{T}\rangle$ stimmen bei $\sqrt{s} = 7$ TeV und 13 TeV am besten mit den experimentellen Daten überein, während sie bei niedrigeren Energien unterschätzt werden.

Die Analyse der p_T-Spektren in Multiplizitätsintervallen im Vergleich zu den jeweiligen Messungen in inelastischen pp-Kollisionen zeigt eine schwache Abhängigkeit von der Kollisionsenergien. EPOS und PYTHIA reproduzieren die Verhältnisse der Spektren in Multiplizitätsbereichen zu den in Minimum-Bias-Messungen qualitativ, beschreiben sie aber nicht im Detail. Die mittlere Teilchenzahl als Funktion der Kollisionsenergie zeigt einen quadratischen Trend und stimmt gut mit anderen Multiplizitätsmessungen von ALICE überein.

ALICE nahm Daten aus Xe-Xe-Kollisionen bei $\sqrt{s_\mathrm{NN}} = 5.44$ TeV auf, jedoch stehen keine Daten aus pp-Kollisionen der selben Energie zur Verfügung. Daher ist die Konstruktion eines pp-Räferenz-Spektrum notwendig, um den nuklearen Modifikationsfaktor zu erhalten. Eine Interpolation zwischen den pp-Daten bei $\sqrt{s} = 5.02$ TeV und $\sqrt{s} = 7$ TeV wurde benutzt unter der Annahme eines Potenzgesetzes als Funktion von $\sqrt{s}$. Die MC-Generatoren wurden als Gegenprobe zur Interpolationsmethode herangezogen und die maximale Abweichung als systematische Unsicherheiten verwendet.

Die nuklearen Modifikationsfaktoren in Pb-Pb und Xe-Xe-Kollisionen wurden berechnet. Sie zeigen eine starke Teilchenunterdrückung in zentralen Kollisionen im Vergleich zu periphären. Für zentrale Xe-Xe-Kollisionen $(0-5\%)$ beträgt die mittlere Zahl der an der Kollision teilnehmenden Nukleonen $\langle N_\mathrm{part}\rangle = 236 \pm 2$, in Pb-Pb-Kollisionen bei 10-20% Zentralität hingegen $\langle N_\mathrm{part}\rangle = 263 \pm 4$. Trotz des klaren Unterschieds zwischen den $\langle N_\mathrm{part}\rangle$-Werten, zeigen die Verhältnisse des nuklearen Modifikationsfaktors beider Systeme eine bemerkenswerte Übereinstimmung. Im Vergleich von 30-40% Xe-Xe und 40-50% Pb-Pb-Kollisionen, erlauben die großen systematischen Unsicherheiten es nicht eine definitive Schlussfolgerung zu ziehen. Die Kompatibilität des nuklearen Modifikationsfaktors bei vergleichbaren Werten der mittleren Teilchenzahl ist in Übereinstimmung mit Ergebnissen der Untersuchung des teilweisen Impulsverlusts von Partonen mit hohem Impuls am RHIC und dem LHC. In dem einfachen Ansatz des radiativen Energieverlusts kann der mittlere Energieverlust als proportional zum Quadrat der Weglänge des Partons im Medium, sowie zur Dichte der Streuzentren angenommen werden.

*To my beloved family and
especially to Lotte for all your support.*

Contents

Chapter 1

Introduction

The Standard Model of particles

The current understanding of the fundamental constituents of the Universe, the elementary particles and the forces between them, is included in the Standard Model (SM). The elementary particles in the Standard Model are divided mainly into two groups, the fermions with half-integer spin and the bosons with an integer spin. Fermions that constitute all the matter, are divided into quarks (up, down, charm, strange, top, bottom) and leptons (electron, electron neutrino, muon, muon neutrino, tau, tau neutrino) and pairs from each classification are grouped together to form a generation. The particles in each generation exhibit similar physical properties but the particle masses increase from generation I to III, as shown in Figure 1.1.

The gauge bosons are the force carriers that mediate the strong, weak and electromagnetic fundamental interactions. The strong interaction is the mechanism responsible for binding quarks that form protons and neutrons, and for binding them inside the nucleus. The force range is limited to a couple of fm (size of the nucleus). The strong force is mediated by the exchange of gluons (massless particles) that interact only between quarks, anti-quarks and other gluons. The Quantum ChromoDynamics (QCD) is the theory that describes this type of interactions, as explained in Section 2.

The weak interaction is the mechanism responsible for the decay of unstable particles and nuclei, for example, the decay of a neutron ($n \rightarrow p + e^- + \overline{\nu}_e$). The intrinsic strength for the weak interaction is $\alpha_w \sim 1/30$, larger than the one from QED. However, the large masses of the associated $W^\pm$ and Z^0 bosons mean that at relatively low-energy scales the weak interaction is significantly weaker than QED.

The electromagnetic force originates from the electromagnetic charge of the particles. In the Standard Model of electroweak interactions, the electric charge is the third component of the weak isospin. The electromagnetic interaction is mediated via exchange of spin-1 virtual photons. The theory that describes electromagnetic interactions is the Quantum ElectroDynamics (QED), which is an abelian gauge theory with the symmetry group U(1). The intrinsic strength of the electromag-

netic force is given by the size of the fine-structure constant $\alpha_{\text{em}} = 1/137$.

The last added particle of the Standard Model was the Higgs boson, discovered in 2012 by the ATLAS and CMS experiments at the LHC [1, 2]. The Higgs boson has a mass $m_H \approx 125$ GeV. Unlike the other fundamental particles and gauge bosons, the Higgs boson is a spin-0 scalar particle and provides the mechanism by which $W^\pm$ and Z^0 bosons acquire mass.

The relative strength of the fundamental interactions are:

- strong interaction: 1

- electromagnetic interaction: 10^{-2}

- weak interaction: 10^{-13}

- gravity: 10^{-38}

Figure 1.1: Fundamental particles of the Standard Model divided into fermions and bosons for each generation. The current mass, charge and spin are quoted for each of them.

Quantum Chromodynamics

Quantum Chromodynamics (QCD) is the gauge field theory that describes the strong interaction between quarks and gluons. QCD is the SU(3) component of the SU(3)×SU(2)×U(1) Standard Model. The QCD-Lagrangian is written as:

$$\mathcal{L}_{\text{QCD}} = \overline{q}(i\gamma^\mu \partial\mu - m_q)q + g_s \overline{q}\gamma^\mu T_a A_\mu^a q - \frac{1}{4}F_{\mu\nu}^a F_a^{\mu\nu} \tag{1.1}$$

where $q, \overline{q}$ are the quark-field (3-vector in color space) spinors of a given flavor and mass m_q. The γ^μ are the Dirac γ-matrices. The A_μ^a correspond to the gluon fields, with a running from 1 to 8 kinds

of gluons. Gluons transform under the adjoint representation of the SU(3) color group. The T_a are the eight 3×3 matrices and are the generators of the SU(3) group, commonly represented by the Gell-Mann matrices ($T_a = \lambda_a/2$). They incorporate the fact that a quark-gluon interaction rotates the quark's color in the SU(3) space. The g_s is the QCD coupling constant. The last term is the field tensor $F_{\mu\nu}^a$ given by

$$F_{\mu\nu}^a = \partial_\mu A_\nu^a - \partial_\nu A_\mu^a - g_s f^{abc} A_\mu^b A_\nu^c \tag{1.2}$$

where the f^{abc} are the structure constant of the SU(3) group.

The local gauge symmetry SU(3) of QCD implies a conserved color charge. In addition, for each quark flavor the difference between quark and anti-quarks flavors is conserved. It implies also a conservation of the electric charge and the baryon number $B = 1/3 \times (n_q - n_{\bar{q}})$.

The fundamental parameters of QCD are the coupling constant g_s (or $\alpha_s = g_s^2/4\pi$) and the quark masses m_q. The renormalization in QCD is similar to that of QED. In QCD the running coupling constant α_s is given by:

$$\alpha_s(Q^2) = \frac{4\pi}{\beta_0 \cdot \ln(Q^2/\Lambda_{QCD}^2)} \tag{1.3}$$

where the β_0 value is dependent on the number of colors n_c and the number of quark flavors n_f as: $\beta_0 = \frac{11}{3}n_c - \frac{2}{3}n_f$; the Q^2 is the energy scale where the constant is tested; and Λ_{QCD} is a constant that is referred as the QCD scale parameter, that must be determined from experimental data or lattice QCD calculations. Λ_{QCD} defines the point at which perturbative QCD (pQCD) is applicable ($\alpha_s \ll 1$). The most commonly used value is $\Lambda_{QCD} \approx 200$ MeV.
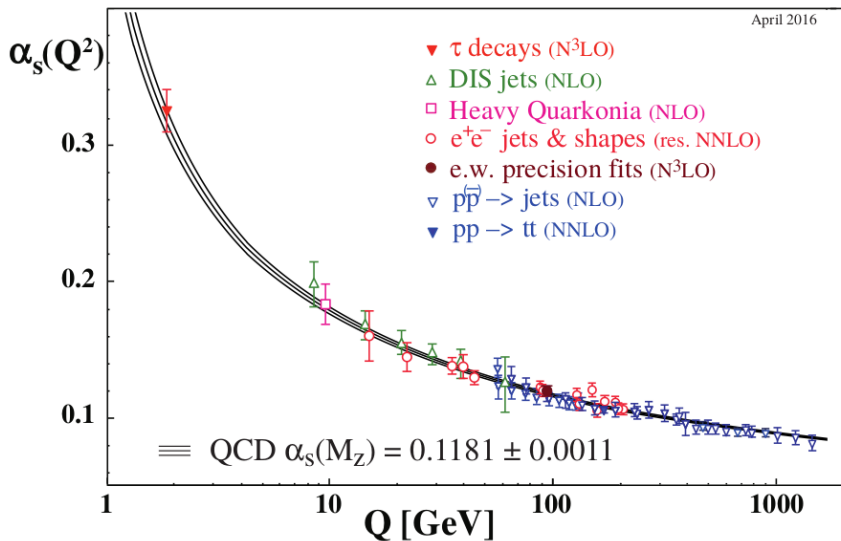

Figure 1.2: Compilation of the measurements and QCD calculations on the running coupling constant α_s as a function of the energy scale Q. Figure taken from [3].

Figure 1.2 shows the running coupling constant α_s as a function of the energy scale Q from different measurements and QCD calculations. At large energy scales when compared to Λ_{QCD}, i.e.

small distances, α_s becomes small. This is known as asymptotic freedom and in this regime, perturbative QCD calculations are applicable. For large distances or at the low momentum scale, the QCD coupling constant becomes large. For this reason, QCD processes are not calculable using perturbation theory. Nevertheless, recently there has been significant progress with the computational technique of lattice QCD where quantum-mechanical calculations are performed on a discrete lattice of space-time points.

One of the features of QCD at low-energy is color confinement where free quarks or free gluons do not exist in nature and instead, they are always bound into colorless hadrons. In a color singlet state, the interaction between partons gets stronger as the distance between them gets larger. In the case of a quark pair, a new quark-antiquark pair will be created when they are pulled apart beyond certain limit. The Lund string-fragmentation model is based on this breaking parton strings and creations of new partons.

The partonic cross sections can be calculated from perturbative QCD and related to hadrons by using the parton distribution functions (PDFs) and fragmentations functions (FF) [4], obtained from experimental values of DIS and jet fragmentations, respectively.

Parton Distribution Function (PDFs)

A precise knowledge of the Parton Distribution Functions (PDFs) of a proton is important to make accurate predictions for the Standard Model processes at hadron colliders. The parton distribution function $f_i(x, Q^2)$ gives the probability of finding a parton (quark or gluon) of flavor i carrying a momentum fraction x in the proton at an energy scale of the hard interaction Q.

The PDFs can not yet be calculated from first principles but are determined from a wide range of experimental data. Information about the PDFs of the proton can be extracted from deep inelastic lepton-nucleon scattering (DIS), such as fixed-target electron-proton and electron-neutron scattering. The general procedure to determine PDFs starts with a parametrization of the non-perturbative PDFs at a low scale and fits to several set of experimental data (DIS data) are performed subject with the constraints imposed by the theoretical framework of QCD such as the DGLAP evolution equations [5]. The outcome of this procedure is a set of PDFs at a particular Q^2 scale.

Figure 1.3 shows the extracted PDFs at $Q^2 = 10 \text{ GeV}^2$ obtained from fits to experimental data from HERA (Hadron Elektron Ring Anlage) [6], where electrons were collided against protons at center-of-mass energies between $\sqrt{s} = 225 - 318 \text{ GeV}$. The results show that the contributions from gluons and sea quarks become large towards low values of x with respect to the valence quarks (u_v, d_v), as expected. At large x, the valence quarks dominates approximately as $u_v(x) \approx 2d_v(x)$.

Fragmentation functions (FFs)

The hadronization process turns partons, produced in hard-scattering reactions (i.e. at large Q^2), into a colorless non-perturbative hadronic bound state. Within the QCD standard framework, processes with an observed hadron in the final-state can be described in terms of perturbative hard
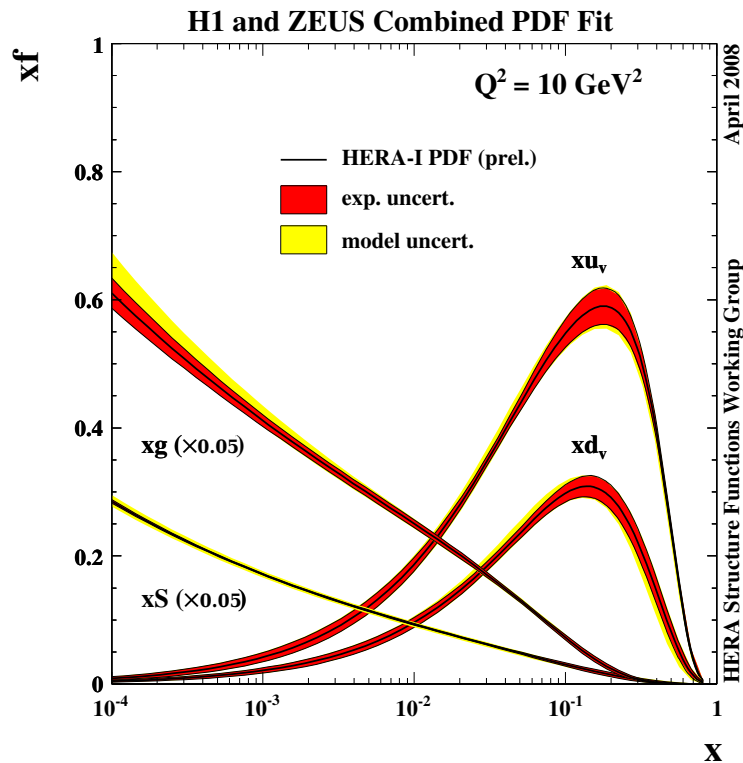
Figure 1.3: Proton PDFs at $Q^2 = 10$ GeV^2 determined from a wide range of experimental data. PDFs of the valence quarks are denoted as u_v and d_v. The sea quarks ($\overline{u}, \overline{d}, s, c, b$) and the gluons contributions are scaled down by a factor 20. Figure taken from [6].

scattering cross sections and non-perturbative but universal functions: the parton distribution functions are responsible for the partonic structure of the hadrons in the initial state just before the interaction and the fragmentation functions (FFs) describe the subsequent hadronization process. The function $D_i^h(z)$ describes the probability that the parton i fragments into a hadron h carrying a fraction z of the parton's momentum [3].

There are two main processes that contribute to parton production after the collisions: the gluon emission by a parton and the splitting of a gluon into a quark-antiquark pair. Hadronization takes place at small scales ($\sim \Lambda_{QCD}$) which makes it a non-perturbative effect. Data from electron-positron annihilation provide the cleanest experimental source for the measurement of fragmentation functions, but is unable to disentangle the FFs of quarks from anti-quarks. Therefore, the best source for quark-antiquark, as well as for flavor, separation is provided from semi-inclusive DIS (performed at much lower scales than for e^+e^- annihilation). In addition, charged hadron production data in hadronic collisions are sensitive to (anti-)quark fragmentation functions.

The phase diagram of nuclear matter

The state of strongly interacting matter in which the quarks and gluons are not longer confined to color-neutral hadrons has been theoretical predicted by QCD from lattice gauge theory [7,8], and assumed to exist in the early stages of the universe and in neutron stars [9]. This state is called

Quark Gluon Plasma (QGP) and is reached when sufficient high temperatures and/or densities are present.

Figure 1.4 shows the lattice QCD calculations for the energy density ε/T^4 as a function of the temperature T, obtained for staggered fermions and different number of flavors. Near the critical temperature of $T_c \approx 173$ MeV, the energy density for 2-flavor QCD calculations exhibit an abrupt variation ($\Delta T/T_c \leq 0.1$), which indicate the transition from hadronic matter to the QGP. For the case of 3-flavor QCD calculations, the critical temperature was found to be lower, $T_c \approx 154$ MeV. At large temperature values ($T > 2T_c$), the energy density is clearly lower than the Stefa-Boltzmann limit of a free gas, which indicates that quarks and gluons in the QGP are strongly interacting. The temperature regimes at which some heavy-ion experiments (SPS, RHIC and LHC) focus are shown in the figure too.
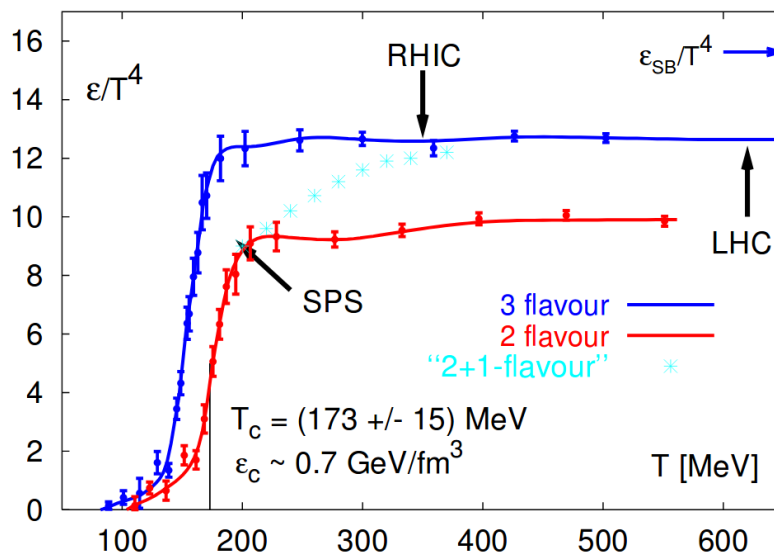

Figure 1.4: The temperature T dependence of the energy density ε/T^4 from numerical solutions of the QCD equations on lattice. The red and blue distributions represent the results with two quark flavors (up and down) and three flavors (up, down and strange), respectively. The light blue star points are for the realistic case when the strange quark mass is roughly 150 MeV larger than the up and down masses. Figure taken from [10].

A sketch of the phase diagram of QCD for nuclear matter in terms of the baryo-chemical potential μ_b and temperature T is show in Figure 1.5. The baryo-chemical potential μ_b measures the imbalance between quarks and anti-quarks in the system, where high μ_b values mean stronger bias favoring quarks over anti-quarks. At values of $\mu_b \approx 1$ GeV and T close to zero is the region where ordinary matter in nature exists. The transition to the QGP phase is expected to be a continuous crossover (second-order transition) for small values of μ_b and temperature of around $T \approx 155$ MeV [11], and becomes a first-order phase transition[1] only beyond a critical value for the baryo-chemical potential [10, 12]. The boundary of the first order phase ends at the critical point, as predicted by Lattice QCD calculations [13], but experimentally has not been proven to exist.

At very high densities ($\mu_b \gg \mu_0$) and low temperatures, a phase of color-superconducting quark matter is expected. It is a degenerate Fermi gas of quarks with a condensate of Cooper pairs near

---

[1]They involve a discontinuous change in density.

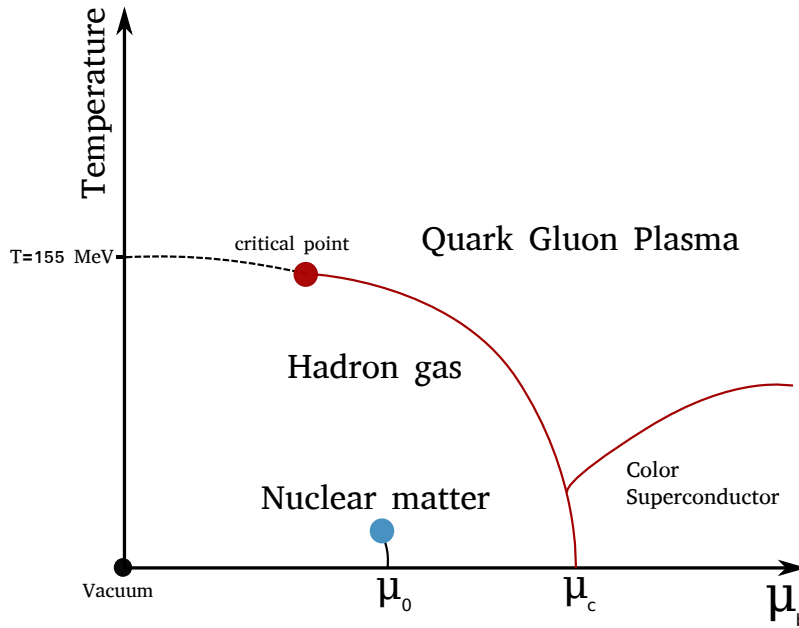the Fermi surface that induces color Meissner effects [14].

Figure 1.5: Sketch of the QCD phase diagram in the temperature-chemical potential $(T - \mu)$ plane of nuclear matter.

The dedicated heavy-ion experiments at Relativistic Heavy Ion Collider (RHIC), BNL and at the LHC, try to obtain the temperature and chemical potential that can be compared to the Lattice calculations. The usual experimental method is to determine the temperature and baryon chemical potential of the fireball at the time of chemical freeze-out. This involve statistical fits to the ratios of hadron abundances measured in the experiments, and extract T and μ_B such that the χ^2 per degree of freedom for the fits is closest to unity [15].
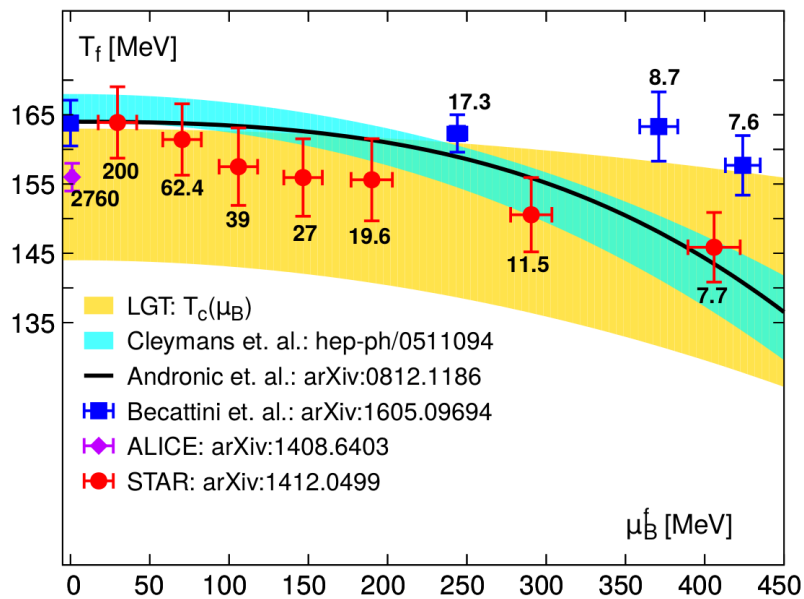

Figure 1.6: Calculations for temperature and baryon chemical potential, obtained from heavy-ion experiments (RHIC and LHC) and from Lattice QCD . Figure taken from [16].

The heavy ion data from RHIC and the LHC suggested that the T and μ_B values are consistent with

predictions from finite temperature QCD Lattice calculations. A summary of the measurements and the predictions is shown in Figure 1.6. The yellow band correspond to the Lattice estimate of the chiral curvature line, while the blue band and black line correspond to different statistical model fits to data. The blue points represent the predictions from a transport model fit to the LHC data for different center-of-mass energies of heavy-ion collisions [16]. The Statistical Model [17,18] give as results $T = 165$ MeV, $\mu_b = 32$ MeV and a system volume of $V = 2400 \; fm^3$, well in agreement with lattice calculations.

Evolution of heavy-ion collisions

Figure 1.7 shows schematically the evolution of a heavy-ion collision in the space-time $(z-t)$ plane. A typical heavy-ion collisions starts with the incoming nuclei in opposite directions at velocities close to the speed of light, and with a deformed shape due to the Lorentz contraction in the laboratory frame rest. At the initial nuclear collision $0 \leq \tau < 0.3$ fm/c, the system is dominated by hard and semi-hard particle production processes which are described in terms of the Color-Glass-Condensate (CGC) [19,20].

After the initial period, the quarks and gluons are in a pre-equilibrium stage that last for as long as 2-3 fm/c. After the pre-equilibrium period, the formation of the QGP starts ($3 < \tau < 6$ fm/c) where quarks and gluons are deconfined and governed by soft collisions. During this period the expansion and the thermalization of the QGP can be described by viscous hydrodynamic equations [21].

The next phase is reached when the QGP expands and reduce the energy density ($T < T_c$) enough that allows the free partons to hadronize, this is called the "hadron gas" stage. Then, the hadrons continue expanding and interacting as time progresses. When the inelastic interactions between partons stops and the particle abundances are fixed, the system is in the "chemical freeze-out" period. The study of the measured yield of particles can give insights into the temperature of the chemical freeze-out.

The "kinetic freeze-out" is the moment when even elastic collisions cease. The particle momenta are fixed at this point and and they freely stream towards the detectors. Both freeze-outs happen after a time of $\tau > 10$ fm/c, approximately.

Jet quenching and parton energy loss in the QGP

The fragmentation of a highly energetic parton produces a collimated stream of hadronic products. These final state hadrons constitute a "jet". Jet production in hadronic collisions is a hard QCD process. An elastic $(2 \rightarrow 2)$ or inelastic $(2 \rightarrow 2 + X)$ scattering of two partons results in the production of two or more partons in the final state, where the leading particle (particle with the largest energy) radiates gluons that later create pairs of quark-antiquark. The hadrons in a jet move in an approximately the same direction that produces a characteristic "jet cone" shape.

Experimentally, jets can be identified based on the radius R from the center of the jet cone. The jet radius is calculated in terms of the (η, ϕ) variables [23]. The main goal of the jet reconstruction is
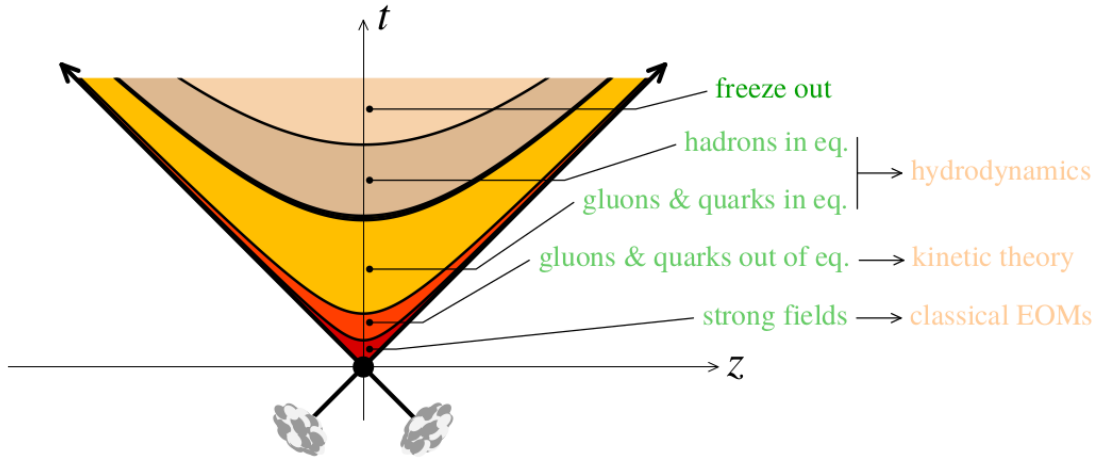
Figure 1.7: Evolution of the fireball in a heavy-ion collisions and the commonly used approaches to describe the stages. Hyperbolic lines show the regions of constant proper time $\tau = \sqrt{t^2 - z^2}$. Figure taken from [22].

to obtain the total momentum of the original hard parton.

One of the signatures of the QGP is the effect of "jet quenching", as proposed by Bjorken [24]. Jet quenching is the attenuation or complete disappearance of the hadrons that compose a jet, as a consequence of the medium-induced partonic energy loss in the QGP. The energy loss ΔE of a particle in the medium provides important information on the plasma properties. ΔE depends on the energy E, mass m, and charge of the particle traversing the medium and on the plasma properties; temperature T, particle-interaction coupling α and thickness L [23, 25].

Figure 1.8 shows schematically a hard scattering between two quarks that originate two jets; one quark is propagating in the QGP and suffers energy loss due to gluon radiation and the other quark escapes earlier to the vacuum where finally both hadronize and are detected as two jets. However, one jet will be quenched with respect to the other. The most used variables to characterize the interactions of a particle in the mediums are:

- the *mean free path* $\lambda = 1/(\sigma\rho)$, where σ is the cross section of the particle-medium interaction and ρ is the medium density[2].

- the *Debye mass* $m_D(T) \sim gT$ is the inverse of the screening length of the chromo-electric fields in the medium. It characterizes the momentum exchange with the medium.

- the *transport coefficient* $\hat{q} = \langle q_T^2 \rangle / \lambda = m_D^2 / \lambda$ gives information about the scattering power of the medium by the average transverse momentum squared per unit of path-length. It combines the thermodynamical (m_D, ρ) and dynamical (σ) properties of the medium.

- the *opacity* $N = L/\lambda$ or number of scatterings suffered by a particle traversing a medium of thickness L.

In general, the total energy loss of a particle is the sum of two mechanisms, the collisional and radiative energy loss; $\Delta E = \Delta E_{\text{coll}} + \Delta E_{\text{rad}}$. The **Collisional energy loss** (ΔE_{coll}) is due to elastic scattering of the high energy parton with the QGP constituents and relevant for low momentum partons. It depends linearly on the medium thickness and logarithmically on the parton energy.

---

[2]For an ideal gas: $\rho \propto T^3$

The stopping power depends quadratically on temperature: $dE/dx \propto \sqrt{\varepsilon} \propto T^2$ [26]. The collisional energy becomes an important component for heavy quarks, while for gluons and light quarks has low influence. Figure 1.9 (left) shows an example diagram of partons that suffer collisional energy loss.
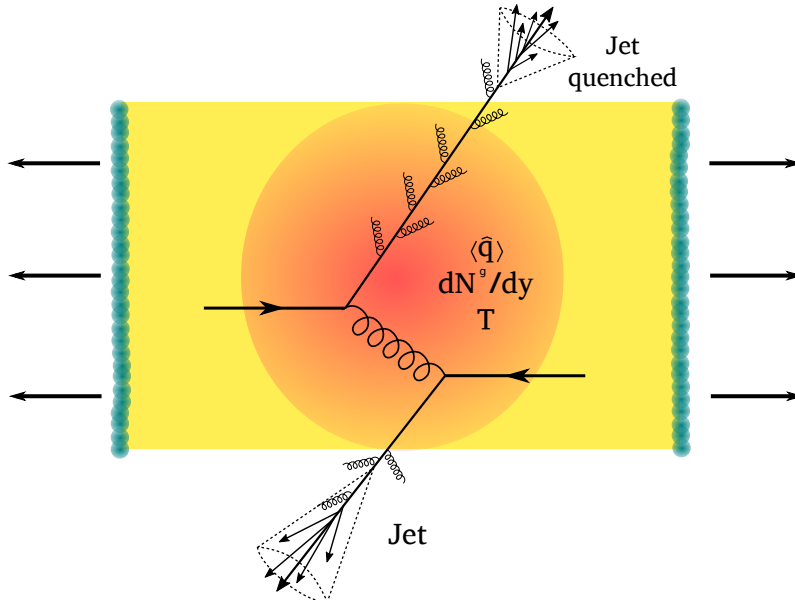

Figure 1.8: Schematic view of heavy-ion collision and the "jet quenching" in the QGP created. Two quarks suffer a hard scattering: one travels directly to the vacuum, radiates gluons and hadronizes into a jet, the other quark goes in the other direction through the dense and hot medium created (characterized by transport coefficient $\widehat{q}$, gluon density dN^g/dy and temperature T), it suffers energy loss via medium-induced gluonstrahlung and then fragments outside into a quenched/reduced jet.

The **Radiative energy loss** ($\Delta E_{\rm rad}$) through inelastic scatterings (medium-induced gluon radiation) is the major component for parton energy loss in the QGP. It dominates for parton energies of $E \gg m, T$; where m is the mass of the parton and T is the medium temperature. According to the medium thickness, two different regimes can be distinguished. For a thin medium ($L \ll \lambda$), the particle suffers at most one single scattering and the energy loss is described by the Bethe-Heithler (BH) formula (see eq.1.4). For the case of a thick medium ($L \gg \lambda$), the opacity is large, i.e. there are N scatterings and the Landau-Pomeranchuk-Migdal (LPM) (see eq.1.5) coherent effect reduces the amount of radiation compared to N times the BH distribution [25]. Figure 1.9 (right) shows an example of radiative energy loss process where a parton losses energy by emitting a gluon caused by the interaction with the medium.

$$\Delta E_{BH} \approx \alpha_s \hat{q} L^2 \ln\left(\frac{E}{m_D^2 L}\right) \tag{1.4}$$

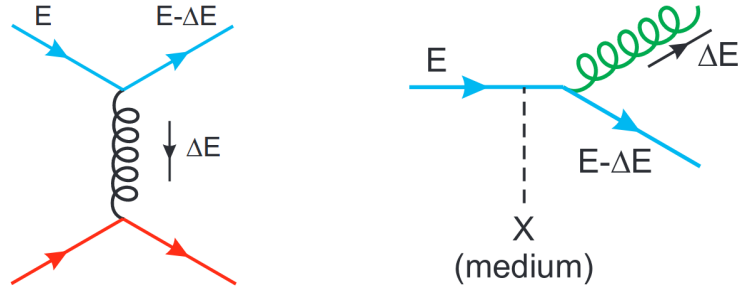$$\Delta E_{LPM} \approx \alpha_s \hat{q} L^2 \tag{1.5}$$

Figure 1.9: Diagrams for the collisional (left) and radiative (right) energy loss (ΔE) of a quark with an energy E experiences when traversing through the QGP. Figure taken from [25].

Experimentally, parton energy loss can be studied in terms of the suppression of jets and high-p_T particles in the medium. The suppression of particles is characterized by the nuclear modification factor R_AA, defined as the ratio of the particle spectrum in nucleus-nucleus collisions (QCD medium) to the spectrum in pp collisions (QCD vacuum). For a fair quantitative comparison, the pp cross section is scaled by the nuclear overlap function T_AA which is proportional to the number of nucleon-nucleon collisions and inverse-proportional to the inelastic cross section of a nucleon: $T_\mathrm{AA} = N_\mathrm{coll}/\sigma_\mathrm{inel}^\mathrm{NN}$, calculated from Glauber model.

$$R_{AA} \sim \frac{\text{``hot/dense QCD medium''}}{\text{``QCD vacuum''}} = \frac{\mathrm{d}^2 N_\mathrm{ch}^\mathrm{PbPb}/\mathrm{d}\eta\mathrm{d}p_\mathrm{T}}{\langle T_\mathrm{AA}\rangle \times \mathrm{d}^2\sigma_\mathrm{ch}^\mathrm{pp}/\mathrm{d}\eta\mathrm{d}p_\mathrm{T}} \tag{1.6}$$

In the absence of suppression of high-p_T particles, the nuclear modification factor is equal to unity. On the contrary, when fewer particles are measured in nucleus-nucleus collisions with respect to the scaled pp spectrum, then $R_\mathrm{AA} < 1$ as a clear signature of suppression. R_AA not only includes particle suppression effects but, in addition, initial and final state effects. Therefore, the nuclear modification factor with proton-nucleus data can help to disentangle these effects from the particle suppression mechanism.

The experiments at RHIC [27–30] and LHC [31–34] have provided clear evidence of the suppression of charged hadrons in central ultra-relativistic heavy-ion collisions. Figure 1.10 shows R_AA for Pb-Pb collisions at $\sqrt{s} = 2.76$ TeV for nine centrality classes, measured with ALICE. In peripheral collisions (70-80%), a small suppression is observed with an overall value of $R_\mathrm{AA} \sim 0.7$ for high-p_T particles. In central collisions (0-5%), a strong suppression is observed for particles at $p_\mathrm{T} \sim 6-7$ GeV/c.
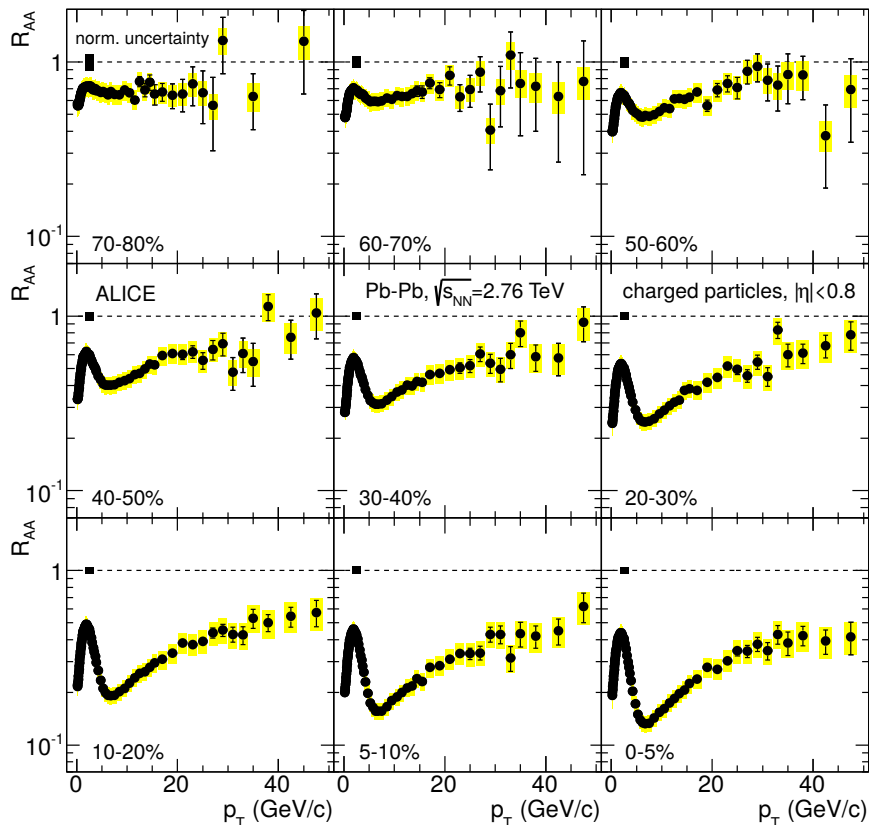
Figure 1.10: Nuclear modification factor R_{AA} of charged particles measured in Pb-Pb collisions at $\sqrt{s} = 2.76$ TeV for nine centralities with ALICE [32]. The colored boxes represent the systematic uncertainties and the vertical lines are the statistical errors. The normalization uncertainty is shown as a box at unity.

Event classification in pp

In hadron-hadron (or more specific proton-proton) scattering, the interactions can be classified by the characteristics of the final states. The interactions can be elastic or inelastic. In the elastic case, both protons emerge intact and no new particles are produced ($p_1 + p_2 \longrightarrow p'_1 + p'_2$). Figure 1.11 a) shows a diagram of an elastic collision in the $\eta - \phi$ map.

In an inelastic interaction, the protons (color singlets) exchange a color octet gluon as they approach each other. As they move apart, they exchange another gluon to become colorless and form two separate systems. However, the particles in the final state do not need to be identical to the initial state in a single-gluon exchange [35]. At the LHC energies, MultiParton Interactions (MPIs) become important and many single-gluon interactions can occur which can produce the same initial state particles in the final state.

Elastic scattering are achieved via the exchange of a glueball-like Pomeron, the final state and initial state particles are identical. The exchange of Pomerons can excite a hadron and can result in the outgoing state preserving the internal quantum numbers of the incoming particles but having higher mass. This is known as quasi-elastic scattering.

Inelastic collisions can be diffractive. The most common description of diffraction is in the Regge

theory. In Regge theory, diffraction proceeds via the exchange of Pomerons [36]. The Pomeron is a color singlet object with the quantum numbers of the vacuum, which dominates the elastic scattering amplitude at high energies. In diffractive scattering, the energy transfer between the two interacting protons remains small, but one or both protons dissociate into multiple-particle final state with the same internal quantum numbers of the initial colliding protons.

When only one of the incoming protons dissociates then the interaction is called Single Diffractive(SD) ($p_1 + p_2 \longrightarrow p'_1 + X_2$ or $p_1 + p_2 \longrightarrow X_1 + p'_2$). Figure 1.11 b) shows a sketch of a SD process, where one of the protons remains intact while the other produce a spray of particles at large η. When both protons break apart, the process is Double Diffractive (DD) ($p_1 + p_2 \longrightarrow X_1 + X_2$), as shown in Figure 1.11 c).

Figure 1.11 d) shows a different event topology that arises when two Pomerons are exchanged. It is the case of a Central Diffraction (CD) process ($p_1 + p_2 \longrightarrow p'_1 + X + p'_2$).

In the Non-Diffractive (ND) interactions, shown in Figure 1.11 e), there is exchange of color charge which results afterwards in a larger number of produced hadrons. The ND interactions are the dominant process in pp interactions with around 70% of all interactions at the LHC [37].

The total cross section in pp collisions σ_{total} is the sum of the processes described above, given as:

$$\sigma_{\text{total}} = \sigma_{\text{elastic}} + \underbrace{\sigma_{\text{SD}} + \sigma_{\text{DD}} + \sigma_{\text{CD}} + \sigma_{\text{ND}}}_{\sigma_{\text{INEL}}} \tag{1.7}$$

The detectors like ALICE, at hadron colliders, usually cover a limited acceptance range around $\eta = 0$. Therefore, elastic collisions are practically invisible to the detectors. The SD events can be detected with a single-arm trigger. For DD and ND collisions, they can be studied with a double-arm trigger.
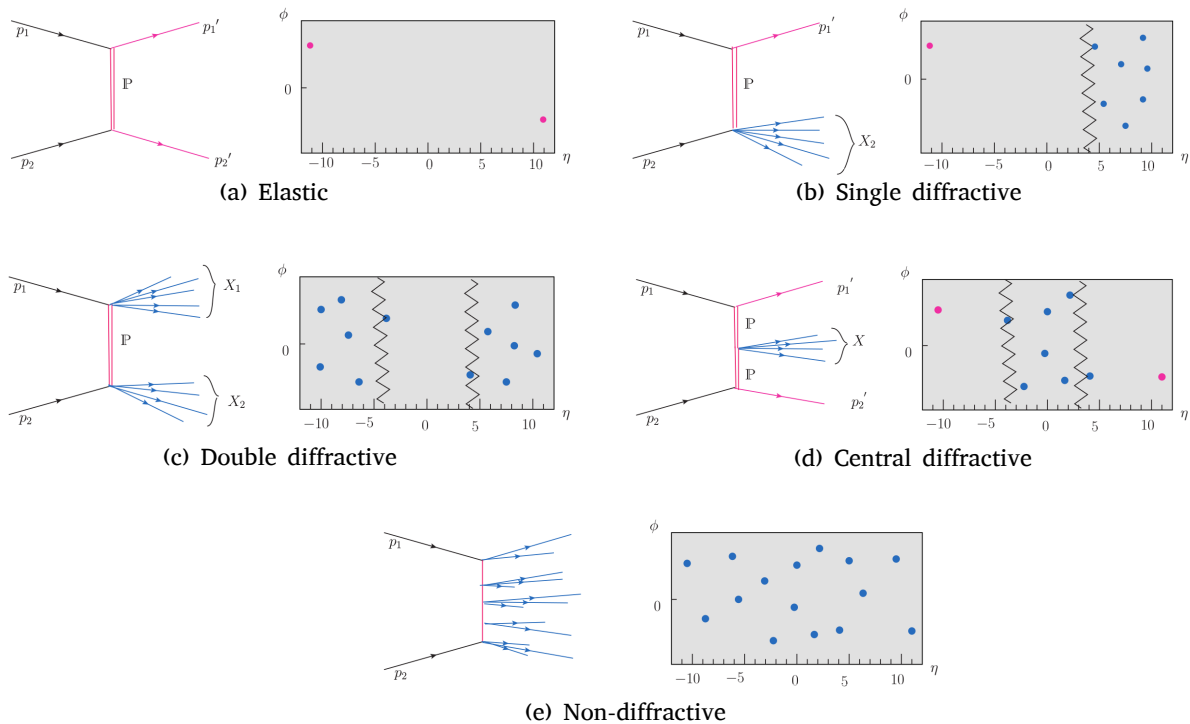
Figure 1.11: a) Diagram for elastic scattering and $\phi - \eta$ map of the distribution of the final state particles. b) Single diffractive for the rapidity window between $-10 < \eta < 3.5$. c) Double diffraction process for the window $-3.5 < \eta < 4$. d) Central diffractive process in two rapidity gaps between $-10 < \eta < -2.5$ and $2.5 < \eta < 10$. e) Non-diffractive process, where there is no rapidity gap, particles are uniformly distributed over ϕ and η. Figure taken from [35].

Collectivity in pp collisions

Before the results from the LHC experiment became available, the idea was that the QGP could only be created in "large" systems, such as those formed in heavy-ion collisions. In "small" systems, such as those created in proton-proton and proton-nucleus collisions were not expected to shows collective behavior [38]. The experimental results [39–42] showed the existence of flow in small systems.

The study of long-range two-particle azimuthal correlations at large pseudorapidity in high final-state particle multiplicity in pp collisions provides information on the dynamics of particle production in small and dense QCD systems. Results from the CMS experiment showed that two particle correlation functions extend over a wide pseudorapidity range ($|\eta| \approx 4$), known as the "ridge" (Figure 1.12). The ridge was first observed in Cu-Cu [43], Au-Au [43] and Pb-Pb [44] collisions at RHIC and LHC experiments respectively. The conclusion was that the hydrodynamic collective flow of a strong interacting and expanding medium is responsible for the long-range correlations [40].
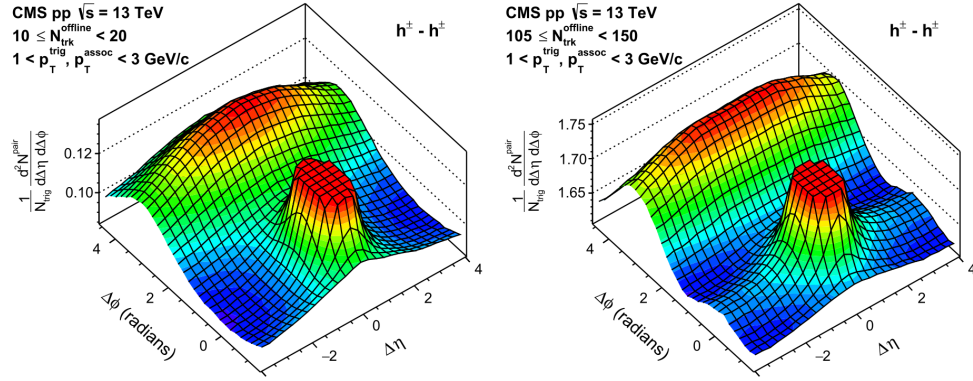
Figure 1.12: Two-particle correlation functions for inclusive charged hadrons for low (left) and high (right) multiplicity ranges in pp collisions at $\sqrt{s} = 13$ TeV. Plot taken from [40].

Another experimental observation that hints at collectivity in small systems is the strangeness enhancement and multi-strange particle production in pp collisions as a function of multiplicity. Figure 1.13 shows how the particle production for identified particles (K_S^0, Λ, Ξ and Ω) increases with respect to the π spectra as the multiplicity increases. There is a smooth transition between the pp, p-Pb and Pb-Pb results. The mass and the multiplicity dependence of the spectral shapes are explained by assuming an increasingly larger collective expansion of the system in the final state [45].

Some theoretical approaches try to explain the collectivity signature in high multiplicity pp collisions. One of them introduces the medium formation idea to explain the collectivity, as in the "One fluid to rule them all" concept [38]. The model describes a common hydrodynamic origin of the experimentally observed flow patterns in high-energy pp, p-Pb and Pb-Pb collisions. Other approaches do not use the formation of a medium, but consider a proton-proton collision as a superposition of multiple partonic interactions. For example, the flow patterns can be reproduced in PYTHIA at the partonic state just before hadronization by the length minimization of the color string between partons [46], mechanism denoted as Color Reconnection.
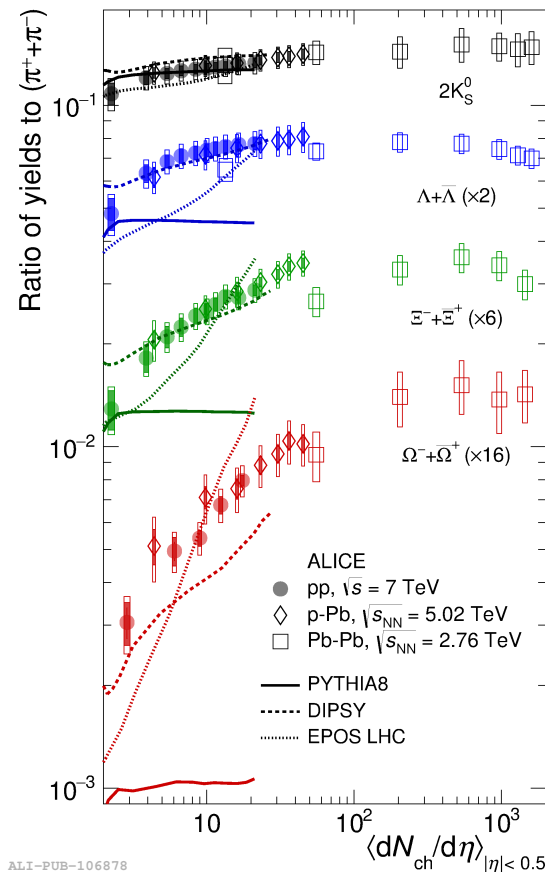
Figure 1.13: p_T-integrated yields ratios for different particles to pions ($\pi^+ + \pi^-$) as a function of multiplicity $\langle dN_{ch}/d\eta \rangle$. Plot taken from [45].

PYTHIA

PYTHIA is a QCD inspired event generator used to produce sets of outgoing particles created in the collisions between two incoming particles (protons, leptons or nuclei).

Figure 1.14 shows the complexity that an event generator like PYTHIA has to face in order to describe or include all the physics mechanisms that play a role in a proton-proton collision [47]. The main physics components in PYTHIA are:

- **Parton Distribution Functions (PDFs)**: Provide the partonic flux from the two initial colliding hadrons, as explained in Section 2.1.

- **Hard Scattering**: It is described by pQCD and involves high-momentum transfer phenomena. A hard scattering is one of the main features in a proton-proton collision. The colliding partons can be valence quarks, sea quarks or gluons. Strong and electroweak processes are implemented in terms of the matrix elements (ME) for the transition from an initial to a final state.

- **Parton showers (PSs)**: In a hard scattering, the branching of a single external parton into two partons is called a parton shower. The flavor and the four momentum are locally conserved, which means that a parton may either split into two partons or not. They can come
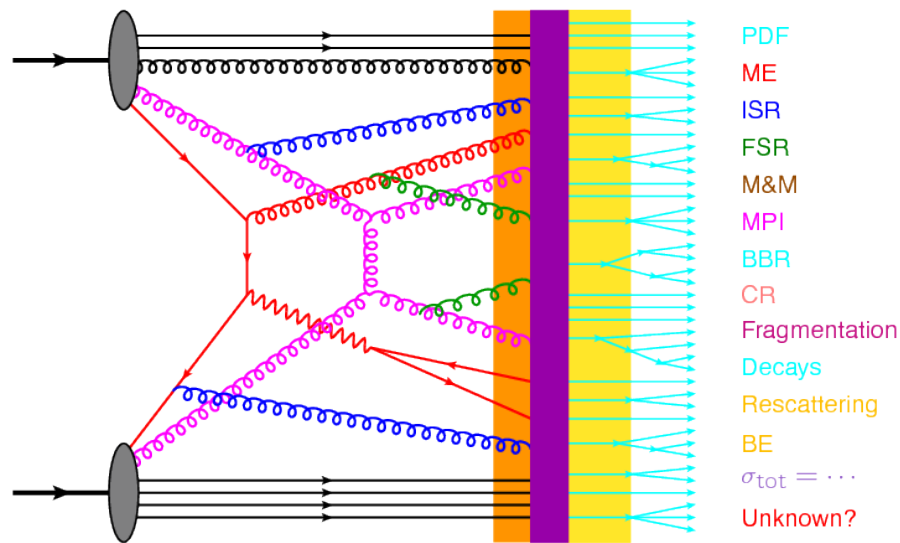
Figure 1.14: Schematic overview of the components in the generation of an event, for example a proton-proton collisions. Figure taken from [47].

from space-like Initial-State Radiation (ISR) and time-like Final-State Radiation (FSR) [48,49]. In addition, Bremsstrahlung radiation caused by accelerating charged particles from the collisions can be described in terms of parton showers (PSs).

- **MutiParton Interactions (MPI)**: The partons may suffer not only one but multiple collisions within one single proton-proton collision. A typical hadron-hadron collision may contain between 4-10 interactions at LHC energies. MPI contain the QCD processes $2 \to 2$, the sum of $qq' \to qq'$, $q'\overline{q} \to q'\overline{q}$, $q\overline{q} \to gg$, $qg \to qg$, $gg \to gg$ and $gg \to q\overline{q}$, and dominated by t-channel gluon exchange contributions [50]. In PYTHIA, the interactions are generated in an ordered sequence of falling p_T until a predefined lower-p_T cut is reached.

- **Beam-Beam remnants (BBR)**: After a hard scattering collision, what is left are the beam remnant partons with flavours given by the remaining valence quarks plus the sea quarks needed for flavor conservation [50].

- **Color Reconnection (CR)**: Is a mechanism that tries to describe the interaction between colored partons during the hadronization stage. The partons are connected via strings, where at one end has a quark and at the other end an anti-quark. With CR the color connections are rearranged between the final-state partons in such a way that the string configuration will converge to a minimum total length. This leads to a reduction in the produced multiplicity when the parton system hadronizes, i.e., for a large number of MPIs, the charged particle multiplicity is smaller when CR is turned on than when CR is off [51]. The motivation to introduce CR as a mechanism in PYTHIA was to explain the increase of the $\langle p_T \rangle$ as a function of the charged particle multiplicity, as observed by UA1 [52]. Figure 1.16 shows schematically

the difference between a hard scattering with and without CR.

- **Hadronization**: In PYTHIA, hadronization is described by the Lund string fragmentation model which is based on the dynamics of one-dimensional strings that are stretched between colored partons (see Figure 1.15). When the confined potential stored in the string is large, it produces break-ups and creates a new quark-antiquark pair. The system then contains new partons connected by a shorter string and an iterative process is followed until the strings are small enough to produce hadrons.

- **Decays**: In PYTHIA, many of the primary hadrons are unstable and decay further at different timescales, according to the known branching ratios [3].

- **Diffraction**: Diffractive collisions are described in terms of exchange of Pomerons. Single, double, central and non-diffractive processes are included in PYTHIA [35], as described in Section 6.
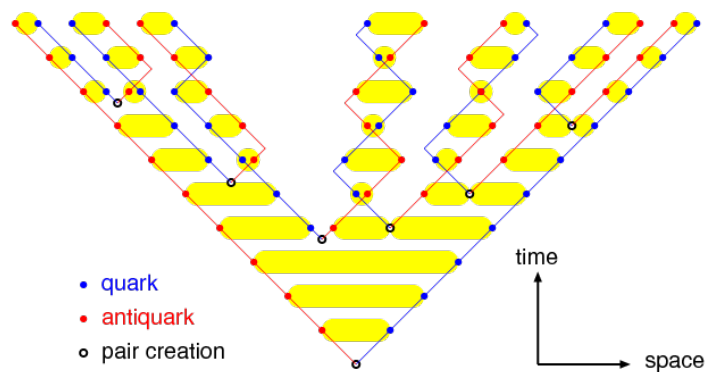

Figure 1.15: Schematic view of the Lund string fragmentation in a quark-antiquark interaction. The iterative string breaking is the basis of hadronization in PYTHIA. Figure taken from [53].
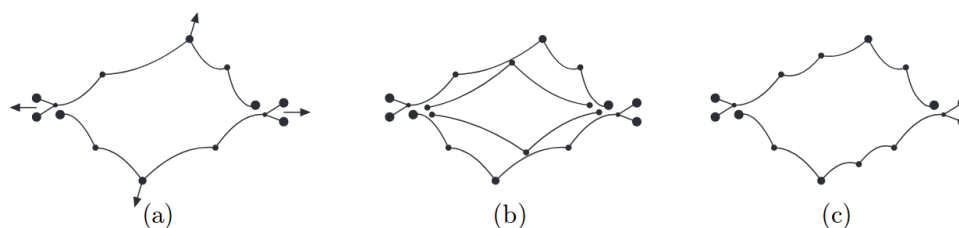

Figure 1.16: **(a)** In a hard gluon-gluon interaction, the outgoing gluons will be colour-connected to the initial projectile and target remnants. Initial state radiation may give extra gluons "kinks" ordered in rapidity. **(b)** A second hard interaction is expected to be connected to the beam remnants and, as a consequence, would create an almost doubled multiplicity. **(c)** In the CR mechanism it is assumed that the gluons are color reconnected, with the shortest total string length possible. This implies that a minimum number of hadrons share the transverse momentum of the parton. Figure taken from [53].

For this thesis, the PYTHIA8 Monash 2013 tune was used as default, specifically the version 8.210 [54, 55]. It uses Minimum Bias, Drell-Yan and underlying-event data from the LHC experiments to constrain the parameters for the Initial-State-Radiation and the MultiParton Interactions. The energy scaling is constrained by the SPS and Tevatron data [56].

EPOS LHC

EPOS is another Monte Carlo event generator for Minimum Bias hadronic interactions, used for proton-proton and heavy-ion collisions, and cosmic ray air shower simulations. The name stands for **E**nergy conserving quantum mechanical approach, based on **P**artons, parton ladder, strings, **O**ff-shell remnants, and **S**plitting of parton ladders. A detailed description of the technical and the physical basis of EPOS is given in [57, 58]. The main features are summarized in the following:
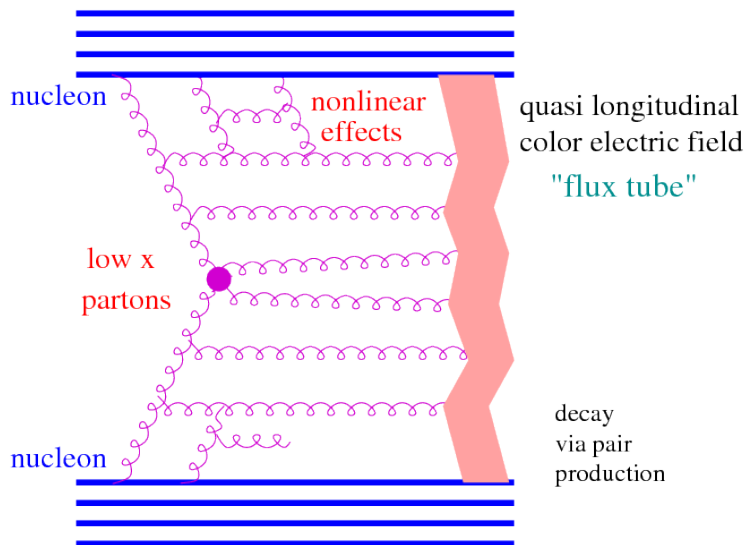

Figure 1.17: Elementary interaction in the EPOS model where each parton-parton interaction creates a parton ladder. Figure taken from [59].

- **Basic principles**: In EPOS, the multiple interactions are based on Parton-Based Gribov Regge Theory [58] and pQCD. It is a consistent quantum mechanical multiple scattering model, based on partons and strings. Cross sections and particle productions are calculated consistently taking into account energy conservation.

- **Parton Ladder**: In a proton-proton interaction, many elementary collisions can happen in parallel. An elementary collision is seen as a "parton ladder", also referred to as Pomeron. A parton ladder represents parton evolutions from the projectile and the target side towards the center (small x) [59]. A ladder may be considered as a quasi-longitudinal color field "flux tube". The flux tube can decay via creation of a quark-antiquark pair, which later will be bound to form hadrons. Figure 1.17 shows a schematic example of an elementary interaction in EPOS.

- **MutiParton Interactions**: Are described by the exchange of more than two parton ladders in parallel, as long as energy conservation is still fulfilled.

- **Collective Hadronization**: The hydrodynamical evolution in EPOS is performed event-by-event with initial conditions based on strings and not on partons, i.e. given by the distribution of Pomerons which correspond to color flux tubes. At an early proper time τ_0, long before hadrons are formed, there is a differentiation between string segments in dense areas (larger

than some critical density ρ_0 segments per volume unit) and those in low density areas. The high density areas are referred to as "core" and the low ones as "corona". The core is made up of different clusters of string segments in a given η slice and is considered to have collective properties like Bjorken expansion in longitudinal direction with additionally some transverse momentum. Particles freeze out at a given energy density ($\varepsilon_{\mathrm{FO}}$), acquiring at that moment a collective radial flow [60].

EPOS LHC is tuned (single set of parameters) to reproduce any kind of hadronic interaction from 1 to 210 nucleons in the energy range from 40 GeV (laboratory frame) to more than 1000 TeV center-of-mass energy. The EPOS LHC v3400[3] differs from previous EPOS 2.x [61] and EPOS 3.x (in develop) in that it does not include the complete 3-D hydro calculation followed by the hadronic cascade [59]. EPOS 2.x or 3.x take large computing time to generate a central Pb-Pb collision, while EPOS LHC takes a fraction of a second, but on the contrary, EPOS LHC has less predictive power and should not be used for precise studies on p_{T} distributions or particle correlations in heavy-ion collisions. For the case of pp and p-Pb minimum bias analysis, EPOS LHC is a good alternative.

---

[3]Open version available with the HepMC interface CRMC at: http://www.auger.de/ rulrich/crmc.html

Chapter 2

The ALICE detector at the LHC

The Large Hadron Collider (LHC)

The LHC is at the moment the largest particle accelerator in the world. The idea of the project started in 1984 and was approved in 1994, but the construction work in the underground tunnel started in 2001. Before the LHC, CERN[1] had the LEP[2] that worked from 1989 to 2000. After dismantling of the LEP, the LHC used the same underground tunnel of 27 km circumference [62], located under the the Swiss-French border area close to Geneva at a depth of 50 to 175 m.

The LHC is a synchrotron that accelerates two counter-rotating beams in separate beam pipes. Each beam rotates many thousand times around the ring until it reaches enough energy to collide. The largest achievable acceleration energies are 7 TeV for protons and 2.76 TeV per nucleon for lead ions, therefore providing collisions at $\sqrt{s} = 14$ TeV and $\sqrt{s_{\mathrm{NN}}} = 5.5$ TeV [63], respectively.

To keep the beam focused and to bend it through the ring, the LHC has 1232 dipoles of 14.3 m length. They contain superconducting magnets which operate at a temperature of 1.9 K. In the LHC, 392 quadrupoles maintain the beam focused, each with a length between 5 and 7 m. Powered by a maximum current of 11.7 kA, the dipoles can provide a magnetic field from 0.535 T during the injection (beam energy of 450 GeV) up to 8.4 T during the collisions(energy of 7 TeV) [63].

The LHC accelerator chain starts with a proton source from a bottle of hydrogen gas at LINAC 2, or a source of ions (Pb) at LINAC 3. The ions are passed through an electric field to strip off some of the electrons, leaving only positive charged particles to enter the accelerator. LINAC 2 and 3 use radio-frequency cavities to charge cylindrical conductors. The protons or ions pass through the conductors, which are alternately charged positive or negative. The conductors behind them push the particles and the conductors ahead of them pull, causing the particles to accelerate. Small quadrupole magnets ensure that the beam remains focused. At the end of this step, protons reach the energy of 50 MeV and lead ions up to 4.2 MeV/u [64]. The Proton Synchrotron Booster is composed by four superimposed synchrotron rings that receive beams of protons from the linear

---

[1]Centre Européen pour la Recherche Nucléaire.
[2]Large Electron Positron Collider

accelerator LINAC 2 at 50 MeV and accelerate them to 1.4 GeV, and ready to be injected into the Proton Synchrotron (PS). Lead ions after LINAC 3 are instead sent to the The Low Energy Ion Ring (LEIR) where they are transformed into short and dense beam-bunches suitable for the injection to the LHC. At the end of the LEIR, lead ions have an energy of 72 MeV/u. The Proton Synchrotron (PS) is the next stage for protons and ions where they are accelerated up to 25 GeV and 6 GeV/u, respectively. They are next injected into the Super Proton Synchrotron (SPS) where protons get an energy of 450 GeV and ions of 177 GeV/u. The Large Hadron Collider is the last stage in the accelerator chain where the beams get their maximum energy [62–64]. Figure 2.1 shows schematically the acceleration process described previously and the four big experiments that record data during the collisions.

The LHC has two high luminosity[3] experiments, ATLAS and CMS receive a peak luminosity of $L = 10^{34}$ cm$^{-2}s^{-1}$ in proton operation. In addition to these high luminosity experiments, the LHC has two low luminosity experiments: LHCb for B-physics, that aims a peak luminosity of $L = 10^{32}$ cm^{-2}s^{-1} and one ion dedicated experiment ALICE, that aims $L = 10^{27}$ cm^{-2}s^{-1} for nominal Pb-Pb operation [63].
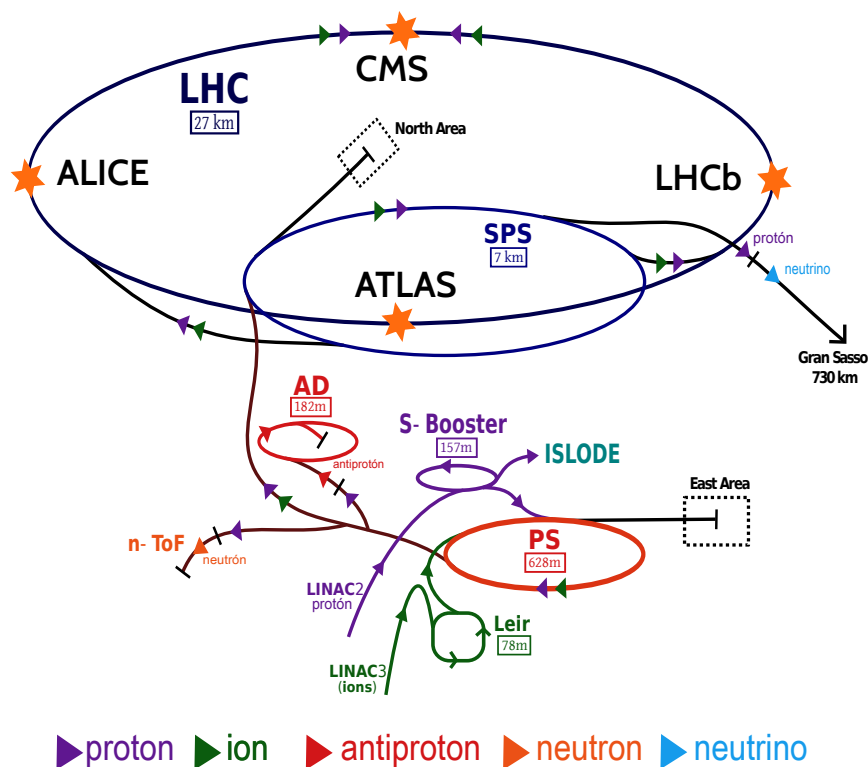
Figure 2.1: Schematic layout of the LHC acceleration chain of protons and lead-ions, figure taken from [65].

ALICE

ALICE(A Large Ion Collider Experiment) is a general-purpose heavy-ion detector at the CERN LHC, that focuses on the strong interaction sector of the Standard Model. It is designed to address

---

[3]The number of events per second generated in the LHC are given by $N_{\text{event}} = L\sigma_{\text{event}}$, where σ_{event} is the cross section of the event under study and L the machine luminosity.

the physics of strongly interacting matter and the QGP at extreme values of energy density and temperature in nucleus-nucleus collisions [66], and to cope with the largest multiplicities expected from Pb-Pb collisions at the highest LHC energies, dN_{ch}/dy up to 6000. During the run 1 period ALICE recorded top multiplicities of $\langle dN_{ch}/d\eta\rangle$=1584±76 for Pb-Pb collisions at $\sqrt{s_{NN}}$=2.76 TeV [67], and for run2 a value of $\langle dN_{ch}/d\eta\rangle$=2035±52 was reached for Pb-Pb collisions at $\sqrt{s_{NN}}$=5.02 TeV [68].

ALICE has several features that make it an important contributor to proton-proton physics program at the LHC. It provides particle identification over a broad momentum range, powerful tracking with excellent resolution from 100 MeV/c to 30 GeV/c, and good determination of secondary vertices. Combined with low material thickness and low magnetic field, it provides unique information about low p_T phenomena in pp collisions at the LHC.

ALICE coordinate system

The ALICE coordinate system is defined according to the LHC rules, and they apply to all the LHC experiments. The coordinate system helps to describe the position and the global parameters of reconstructed tracks in the detectors, the system is a right-handed orthogonal Cartesian system with the origin (0,0,0) at the interaction point (IP). The x-axis is perpendicular to the beam direction, aligned with the local horizontal and points to the LHC ring center. Positive x is from the point of origin toward the accelerator center and negative x is from the origin outward. The y-axis is perpendicular to the x-axis and the beam direction. Positive y is from the origin point upward. The z-axis is parallel to the beam direction where the ALICE muon arm is at negative z [69]. The detector located at positive z are labeled A, those at negative z are C and elements around $z = 0$ are labeled B.

In order to define the detector acceptance the pseudo-rapidity is calculated as follows:

$$\eta = -ln\left(\tan\frac{\theta}{2}\right) \tag{2.1}$$

where $\eta = \pm\infty$ coincides with the beam axis (z) while $\eta = 0$ is in the $x - y$ plane.

ALICE subdetectors

Hadrons, electrons and photons are detected and identified in the central rapidity region $|\eta| < 0.9$, by a complex system of detectors placed in a moderate magnetic field (0.5 T). Tracking relies on a set of high-granularity detectors: an Inner Tracking System (ITS) consisting of six silicon layer detectors, a large-volume Time-Projection Chamber (TPC), and a high-granularity Transition-Radiation Detector (TRD). Particle identification in the central region is performed by measuring energy-loss in the tracking detectors, transition radiation in the TRD, and by measuring the time of flight of particles with a high-resolution by the TOF detector. Two smaller single-arm detectors complete particle identification at mid-rapidity, the High-Momentum Particle Identification Detector (HMPID) that uses the Cherenkov radiation as a detection principle, and PHOton Spectrometer (PHOS) to detect photons with an electromagnetic calorimeter based on scintillating crystals. The

1. ITS
2. FMD, T0, V0
3. TPC
4. TRD
5. TOF
6. HMPID
7. EMCal
8. DCal
9. PHOS, CPV
10. L3 Magnet
11. Absorber
12. Muon Tracker
13. Muon Wall
14, Muon Trigger
15. Dipole Magnet
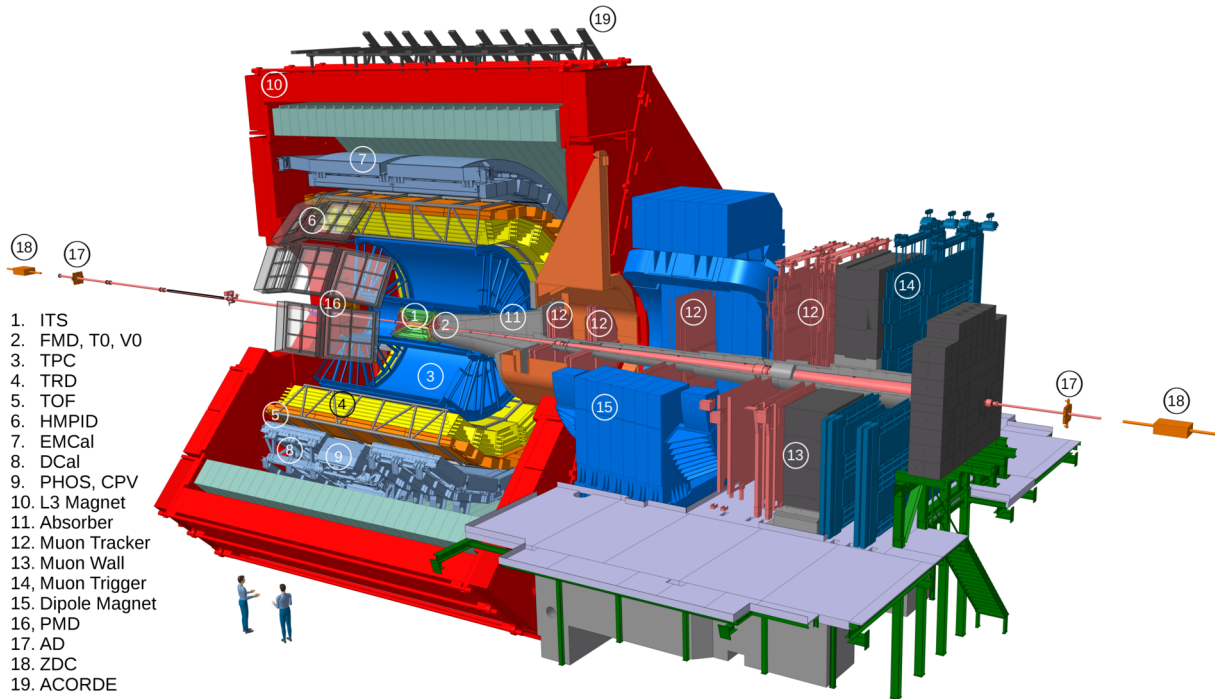16, PMD
17. AD
18. ZDC
19. ACORDE

Figure 2.2: Schematic layout of the ALICE detector.

ElectroMagnetic Calorimeter (EMCAL) increases the electromagnetic coverage of ALICE by an order of magnitude, which provides a fast and efficient trigger for jets, photons and electrons. The detection and identification of muons is performed with a dedicated forward spectrometer, which includes a large warm dipole magnet that covers the pseudo-rapidity region of $-4.0 < \eta < -2.4$ [70]. Additional detectors located at large rapidities complete the detection system to characterize the event and to provide the interaction trigger. They cover a wide acceptance ($-3.4 < \eta < 5.1$) for the measurement of charged particles and triggering, the Forward Multiplicity Detector (FMD), the V0 and T0 detectors. The measurement of photon multiplicities is performed in a narrower range $2.3 < \eta < 3.5$ by the Photon Multiplicity Detector (PMD). Finally, Zero-Degree Calorimeters (ZDC) measure spectator nucleons in heavy-ion collisions close to the beam rapidity at both sides of the experiment [71].

ITS (Inner Tracking System)

The Inner Tracking System (ITS) is the innermost detector of ALICE. It consists of six cylindrical layers of position-sensitive detectors, covering an acceptance from $|\eta| < 0.9$ to $|\eta| < 2$ for vertices located within 10 cm along the beam direction (z).

The high resolution and precision required for the innermost planes is achieved with silicon micro-pattern detectors with two-dimensional readout. The first two layers correspond to the Silicon Pixel Detector (SPD) and the subsequent two correspond to the Silicon Drift Detector (SDD). At larger radii from the interaction point, the requirements of a high resolution are less strict, therefore two layers of Silicon Strip Detectors (SSD) are used. The ITS detector design is schematically shown in Figure 2.3.

The number, position and segmentation of the layers as well as the technology used in the ITS detector were optimized for an efficient track finding and high impact-parameter resolution for the very high multiplicity conditions expected in central ion-ion collisions. The ITS aims to reconstruct the primary vertex and the secondary vertices (important for the reconstruction of charm and hyperons decays). The ITS in addition can provide particle identification, tracking of low-momentum particles and helps to improve the momentum and angle measurements of the Time Projection Chamber (TPC) detector [72].

SPD

The Silicon Pixel Detector constitutes the two innermost layers of the ITS, located at radii of 3.9 cm and 7.6 cm from the beam axis. The layers cover an acceptance of $|\eta| < 2$ for the layer 0 and $|\eta| < 1.4$ for the layer 1, with the nominal interaction point located at $z = 0$.

The SPD detection technology is based on hybrid silicon pixel, consisting of a two-dimensional matrix (sensor ladder) of silicon detector diodes. The sensor matrix includes 256×160 cells with a size of $50 \times 425 \ \mu m$ ($r\phi \times z$), which defines the two track separation and the position resolution. The low amount of material, around 1% of the radiation length X_0 per layer, allows to track particles down to 80 MeV/c.

The SPD is an essential element for the determination of the position of the primary vertex as well as for the measurement of the impact parameter of secondary tracks originating from the weak decays of strange, charm and beauty particles. To achieve this measurement, the SPD has a spatial precision of 12 μm in $r\phi$ and 70 μm in z coordinates. It is designed to operate in a region where the track density is as high as 50 tracks/cm^2, and at relatively high radiation levels [73].

SDD

The Silicon Drift Detector conforms the middle two layers of the ITS are located at radii of 15 cm (layer 2) and 24 cm (layer 3) from the beam axis with an acceptance coverage of $|\eta| < 0.9$ for both layers. The operating principle of a silicon drift detector is based on the drift of the electrons produced in the silicon sensitive volume by a crossing ionizing particle. Electrons then drift towards the collecting anodes due to an electric field. In this way the distance between the interaction point and the anodes is determined by the measurement of the drift time. The other coordinate is obtained from the centroid of the charge distribution along the anode direction.

The SDD detector consist of 260 modules distributed in two layers, with an active area of 7×7.53 cm^2. The position resolution is 38 μm along the drift direction ($r\phi$) and 28 μm along the beam direction. The SDD detector contributes to the excellent resolution of the impact parameter, that is better than 75 μm for tracks at 1 GeV/c. This can be achieved due to the limited material budget, 7.7% X_0 for radial tracks. The layers have very good multi-track capability and provide two out of four dE/dx samples needed for the ITS particle identification.

SSD

The Silicon Strip Detector is located in the last two outer layers of the ITS, at radii of 38 cm and 43 cm and covers an acceptance of $|\eta| < 0.9$. At this radii, a density below 1 track/cm^2 is expected. The silicon strip detector system covers an area of about 2.3 m^2 in the layer 5 and 2.9 m^2 the layer 6. It is composed out of 782 (layer 5) and 988 (layer 6) double-sided silicon strip detectors with each sensors having a rectangular shape with an active area of 7.3×4 cm^2 [72].

The SSD layers are crucial for the matching of tracks from the TPC to the ITS. They provide a two dimensional measurement of the track position with a spatial resolution of 20 μm in the rϕ direction and 830 μm in the beam direction. In addition they provide dE/dx information to assist the particle identification for low-momenta particles.
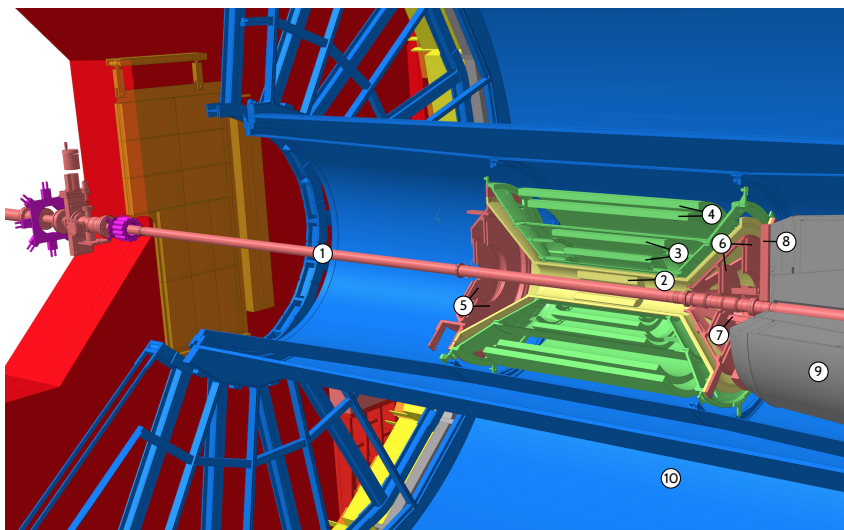

Figure 2.3: Layout of the ALICE inner detectors that surround the beam pipe(1). The ITS consist of two layers of SPD(2), two of SDD(3) and two of SSD(4). The FMD(5,6), TZERO-C(7) and VZERO-C(8) located in the forward region. On the C-side the muon absorber(9) is located. And the TPC(10) detector surrounds all the inner detectors.

TPC (Time Projection Chamber)

The Time-Projection Chamber (TPC) [74, 75] is the main tracking detector of the ALICE central barrel and, together with the ITS and the other central barrel detectors, provides charged-particle momentum measurements with good two track separation, particle identification, and vertex determination.

The TPC covers the pseudo-rapidity region $|\eta| < 0.9$ for tracks with full radial track length (matches ITS, TRD and TOF detectors). The TPC covers the full azimuth with exception of the inactive areas between sectors. It covers a large p_T range, from 0.1 GeV/c up to 100 GeV/c with good momentum resolution.

The TPC is a cylindrical detector with an inner radius of 80 cm, an outer radius of about 250 cm and an overall length of 500 cm in the beam direction. To ensure minimal multiple scattering and low secondary particle production, the material budget of the TPC has to be as low as possible (3%

X_0 at around $\eta = 0$). This required special attention to materials used in the construction of the field cage and a light counting gas, therefore the detector is filled with 88 m^3 of Ne/CO$_2$ (90%/10%). For run 2 program, an another gas mixture was used (Ar/CO$_2$) in order to provide a more stable operation in high particle fluxes during heavy-ion running at larger collision energies compared to those from the run 1 program. Due to the gas mixture and the necessity of high rate capability, the field cage of the TPC has to run at high voltage gradients. A conducting electrode at the center of the cylinder, charged to 100 kV, provides a precise axial electric field of 400 V/cm together with a voltage dividing network at the surface of the outer and inner cylinder [74]. Figure 2.4 shows the TPC field cage layout.

Charged particles traversing the detector ionize the gas. Due to the electric field influence, the electrons drift to the end-caps of the detector, where their arrival point in the cylinder plane is precisely measured. Combining this information with an accurate measurement of the arrival time[4], the complete trajectory in space of all charged particles traversing the TPC can be determined with precision.
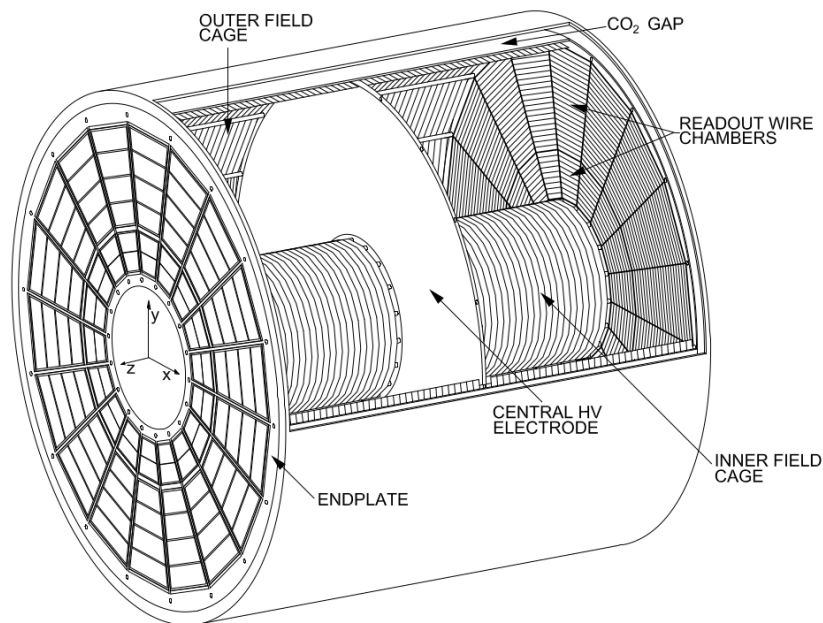

Figure 2.4: Schematic layout of the TPC field cage. The high-voltage electrode is located at the center of the drift volume. The endplates consist of 18 sectors and 36 readout chambers on each end. Figure taken from [76].

The necessary signal amplification is provided through an avalanche effect in the vicinity of the anode wires strung in the readout (see Figure 2.5). Moving from the anode wire towards the surrounding electrodes, the positive ions created in the avalanche induce a positive current signal on the pad plane. This current signal, which is characterized by a fast rising time (less than 1 ns) and a long tail with a rather complex shape, carries a charge that is about 4.8 fC for the minimum ionizing particle.

The readout chambers cover the two end-caps of the TPC cylinder, with an overall area of 32.5 m^2. Their design is based on Multi-Wire Proportional Chamber (MWPC) technique with a cathode pad

---

[4]Relative to some external reference such as the collision time of the beams from the LHC.

readout. The chambers are mounted in 18 trapezoidal sectors for each end-plate. The TPC is composed by ∼ 560000 readout pads, with the purpose to keep the occupancy as low as possible and to ensure the necessary dE/dx and position resolution [74, 75].

The readout chambers are normally closed by a gating grid for electrons coming from the drift volume. The gating grid are opened only by the L1 trigger (6.5 μs after the collision) for the duration of one drift-time interval, of around 90 μs. This helps to prevent space charge due to positive ions from drifting back from the multiplication region for non-triggered interaction and background. All schematic example of a track detection in a readout chamber is shown in Figure 2.5.
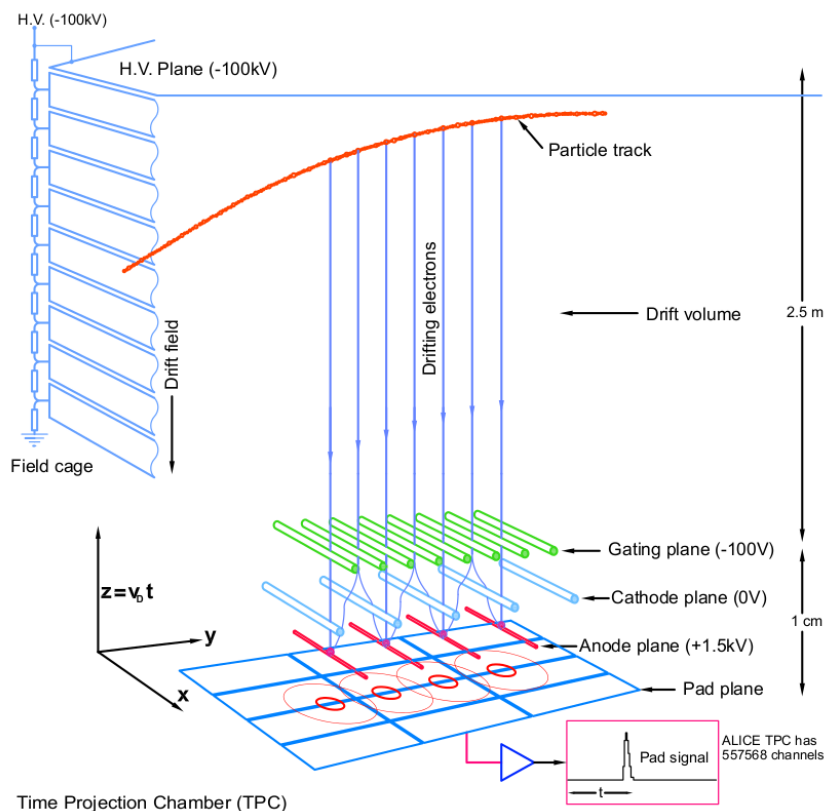

Figure 2.5: Schematic view of a track detection in the TPC detector. Figure taken from [76].

V0 (V-ZERO)

The V0 detector is a small-angle detector that consists of two arrays of scintillator arrays, located at both sides of the ALICE collision vertex, V0A and V0C. The V0A detector is located at 330 cm away from the vertex in the positive z-direction (opposite to the muon spectrometer), as shown in Figure 2.2. The V0C is fixed at the front face of the hadronic absorber, 90 cm from the vertex. Their pseudo-rapidity ranges are $2.8 > \eta > 5.1$(V0A) and $-3.7 < \eta < -1.7$(V0C) [66].

The V0 detector is a disk of 47 mm in thickness, 76 cm in diameter with a central hole of 84 mm in diameter. Each array consists of 32 counters distributed into 4 rings. Each of these rings covers 0.5 - 0.6 units of pseudo-rapidity and divided into 8 sectors (45°) in azimuth, as shown in Figure 2.6. For the V0C array, the rings 3 and 4 are divided into two identical detectors with the purpose

to optimize signal uniformity and a smaller time fluctuation [77]. The segmentation also allows the measurement of anisotropic flow observables and the determination of an event plane.

The V0 detector has several functions. During data taking, it provides a Minimum Bias trigger (MB), Multiplicity Trigger (MT), semi-Central Trigger (CT1) and Central Trigger (CT2) for the central barrel detectors in pp and A-A collisions (V0-AND mode). The V0 detector is able to provide also Minimum Bias p-Gas triggers (PG), originated from interactions of beam particles with the residual gas of the vacuum chamber. In pp collisions, the efficiency of the V0 for detecting at least one charged particle at both sides is about 84%. Finally, the V0 detector participates in the measurement of luminosity with a precision as better than 10% [77].
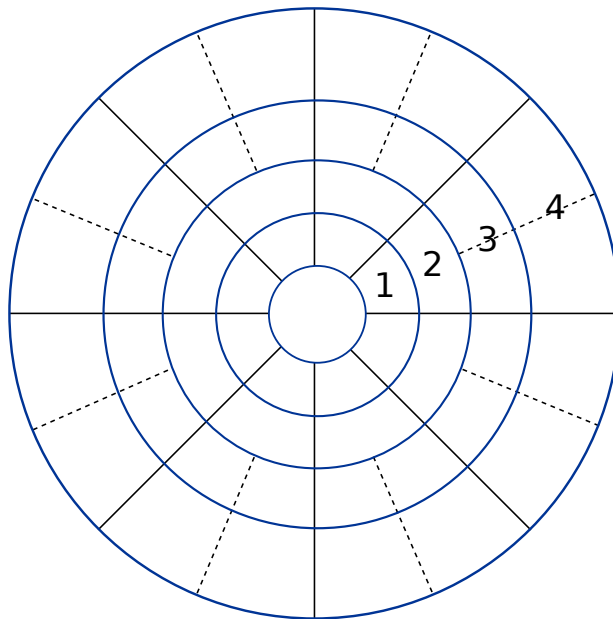

Figure 2.6: Segmentation of V0A and V0C detector arrays.

Track and vertex reconstruction

Tracking in the central barrel starts with the determination of the interaction vertex, by using the two innermost layers (SPD) of the ITS. The vertex is found by looking at the space point to which a maximum number of tracklets[5] converge. In pp collisions, where few pileup interactions are expected, the algorithm is repeated several times and discards at each iteration those clusters that contributed to already-found vertices. By construction, the first vertex found has the largest number of contributing tracklets and is assumed to be the primary one. When a single convergence point is not found, particularly in low-multiplicity events, the algorithm performs a one-dimensional search of the maximum in the z-distribution of the points of closest approach (PCA) of tracklets to the nominal beam axis [72].

The track reconstruction begins with the cluster[6] finding process in all of the ALICE central de-

---

[5]Tracklets: lines defined by pair of clusters, one cluster in each SPD layer.

[6]Cluster: This is a set of adjacent (in space and/or in time) digits that were presumably generated by the same particle crossing the sensitive element of a detector.

tectors. The clusters are reconstructed at the two pixel layers of the ITS, then the position of the primary vertex is estimated before the track finding starts.

The general tracking strategy starts at the TPC outer radius, where the track density is minimal. First, the track candidates (seeds) are found and processed to smaller TPC radii. Since there is a small number of clusters assigned to a seed, the precision is not sufficient to safely extrapolate the tracks outwards to the other detectors. Therefore, new clusters are associated with a track candidate via the Kalman filter [78] and the track parameters are more and more refined. When all of the seeds are extrapolated to the inner limit of the TPC, the tracking in the ITS takes over. The ITS tracker tries to prolong the TPC tracks as close as possible to the primary vertex and are assigned precisely reconstructed ITS clusters, which also improves the estimation of the track parameters [74, 79, 80].

After all tracks from the TPC have their assigned clusters in the ITS, a special ITS-standalone tracking procedure is applied to the rest of the ITS clusters. This procedure tries to recover the tracks that were not found in the TPC because of the p_T cut-off, inactive areas between the TPC sectors, or decays. Now, the tracking is restarted from the vertex back to the outer layer of the ITS and a similar procedure is repeated towards the outer wall of the TPC. For the track that was labeled by the ITS tracking as potentially primary, several particle-mass-dependent and time-of-flight hypotheses are calculated. Once the outer radius of the TPC is reached, the precision of the estimated track parameters is sufficient to extrapolate the tracks to the TRD, TOF, HMPID and PHOS detectors. Tracking in the TRD is done in a similar way to that in the TPC. Tracks are followed until the outer wall of the TRD and the assigned clusters improve the momentum resolution further. Next, the tracks are extrapolated to the TOF, HMPID and PHOS, where they acquire the PID information. Finally, all the tracks are refitted with the Kalman filter backwards to the primary vertex (or the innermost possible radius, in case of a secondary track) [80].
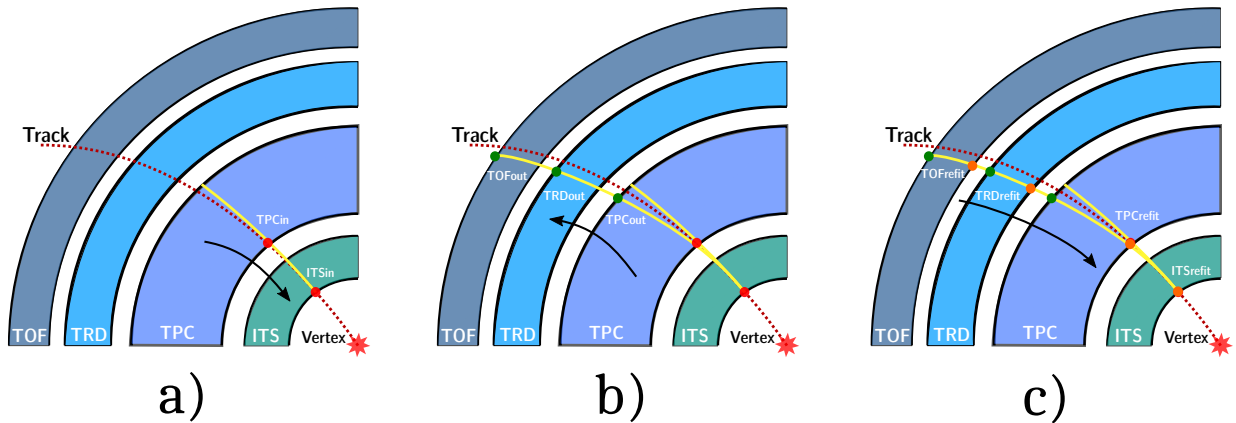

Figure 2.7: Track reconstruction process in the central barrel detectors. a) Track candidate are found in the TPC and extrapolated to the inner layers of the ITS. b) Track candidates obtained with ITS-TPC are extrapolated to the outer wall of the TPC, TRD and TOF detectors. c) Tracks are refitted with the Kalman filter inwards to the primary vertex.

Chapter 3

Transverse momentum spectra

Introduction

This chapter describes analysis details, strategy and corrections used to obtain the transverse momentum (p_T) distributions for primary charged particles, produced in proton proton (pp) collisions at several collision energies, as well as the improved corrections such as the particle composition and contamination by secondary particles. Data from run 1 and run 2 from ALICE is used and sophisticated correction methods are applied to it, which lead to an improved precision of more than factor two when compared to previous analyses. Data from pp collisions at $\sqrt{s} = 5.02$ TeV is used as an example to explain the correction methods and the systematic uncertainties calculation. Final results will be presented for all energies and collision systems.

The analysis is performed on tracks that are reconstructed using the combined tracking information of the TPC and ITS. The relevant track parameters are the transverse momentum p_T, and the pseudorapidity η. In addition, the event is characterized by several parameters, like multiplicity (centrality in the case of Pb–Pb or Xe-Xe) and z-position of the reconstructed primary vertex. The analysis aims at reconstructing the original transverse momentum distributions from the measured ones. Detector effects enter at various stages and are corrected for. The corrections are largely based on Monte Carlo simulations but also include data-driven methods. Correction procedures and the respective systematic uncertainties will be described in this chapter.

Primary-charged-particle definition

Primary charged particles that have been reconstructed as observable tracks in the detectors have been selected for the analysis. According to the ALICE definition, primary particles are those that fulfill the following requirement:

Primary charged particles are defined as prompt charged particles produced in the collision, including their decay products, but excluding products of weak decays of muons and light flavor hadrons [81].

System	$\sqrt{s}$	Year	Data sample	MC generator
pp	2.76 TeV	2011	LHC11a, pass4	PYTHIA 8
pp	5.02 TeV	2015	LHC15n, pass3	PYTHIA 8
pp	7 TeV	2010	LHC10d, pass2	PYTHIA 6
pp	13 TeV	2015	LHC15f, pass2	PYTHIA 8

Table 3.1: Data taking periods and corresponding Monte Carlo event generator used in this work.

This definition requires that a particle lives long enough that it may, in principle reach active detector material. A long-lived particle means that has a proper lifetime larger than 1 cm/c, which is either produced directly in the interaction between colliding partners or from decays of particles with τ smaller than 1 cm/c, restricted to decay chains leading to the interaction. Therefore, the particles species that fulfill the ALICE definition requirement are: e^-, μ^-, π^+, K^+, p, Σ^-, Σ^+, Ω^-, Ξ^- and their antiparticles. The decay products of short lived particles like D mesons or neutral pions are also considered primary particles.

Data and MC samples

ALICE took data for all the collision systems and energies provided by the LHC in run 1 and run 2 programs [82]. The data taking started in fall 2009 with pp collisions at the LHC injection energy of $\sqrt{s} = 0.9$ TeV. In June-July 2010, the proton beam energy was brought up to $\sqrt{s} = 7$ TeV, half of its nominal value[1], and the luminosity was gradually increased. In this period, the interaction rate was low (between a few kHz and a few tens of kHz) and ALICE mostly triggered on minimum bias (MB_{OR}) interactions using the V0 or ITS(SPD) detectors. In 2011, the LHC resumed operation with a short period at the end of March, where pp collisions at $\sqrt{s} = 2.76$ TeV were recorded. The run 1 program finished in 2013 when ALICE recorded pp collisions at $\sqrt{s} = 2.76$ TeV for the second time, with increased luminosity. For this analysis, only 2011 data was used.

In mid 2015, ALICE restarted the data taking for run 2 program with the LHC providing pp collisions at a top center-of-mass energy of 13 TeV [83]. In November of the same year, the collision energy changed to $\sqrt{s} = 5.02$ TeV.

For each data period taken, a Monte Carlo simulation has been generated. The common event generators used in this work were PYTHIA8 (Monash) [55, 56] or PYTHIA6 Perugia2011 [54]. In addition, GEANT3 [84] plus the particle propagation in the detector material was used for the simulation of the detector response, with exactly the same parameters of the experiment that were present during data taking.

---

[1]The LHC was designed to provide proton proton collisions at $\sqrt{s} = 14$ TeV.

Trigger and event selection

The selection of the recorded events is resolved in two consecutive stages. The first stage is the online selection (during data taking procedure) where only events that fulfill the ALICE trigger condition are candidates to be recorded. The second stage is the offline selection, which uses the recorded candidate events from the online stage and go through further selection criteria, like reevaluation of the trigger condition, acceptance and/or centrality selection region, depending of the collision system [70, 71].

For the online trigger selection, signals from the SPD and VZERO detectors are used together in coincidence with two bunches crossing the detector at the same time. Some fired signals in the triggers can be caused from background from the LHC beams. The fake and pileup events are excluded from the analysis via the SPD clusters vs tracklet correlation. The trigger configuration which imposes the smallest selection bias by accepting most of the events is called Minimum Bias (MB) trigger. A detailed trigger information can be found in [85].

This analysis uses data selected with the MB trigger. The trigger is optimized to achieve high efficiencies in low multiplicity events as well as for non single diffractive (NSD) hadronic interactions, and for good background rejection. Depending on the data period taking, the MB trigger condition used different detector logic. Table 3.2 summarizes the pp data recorded in ALICE and its corresponding trigger condition. Figure 3.1 shows the trigger and vertex efficiencies as a function of the z-position of the primary vertex for different pp collision energies. Looking in detail at the trigger efficiencies, one notes that the $V0_{AND}$ condition is more restrictive than the MB_{OR}, which leads to a reduced efficiency as a function of V_z(cm). This is the case for 5.02 TeV and 13 TeV ($V0_{AND}$) data with an overall trigger efficiency of 80% while the 7 TeV and 2.76 TeV (MB_{OR}) data has an efficiency of 94%.

Figure 3.2 shows the trigger efficiency as a function of the track multiplicity measured in the kinematic range of $p_T > 0.15\,\mathrm{GeV}/c$ and $|\eta| < 0.8$. For the case of pp collisions at $\sqrt{s} = 7$ TeV and 2.76 TeV data, the trigger is fully efficient when there is at least one track in the acceptance. This fully efficient trigger is as expected, since a particle in the central region has a large probability to leave a signal in the SPD detector, one of the conditions in the MB_{OR} trigger. Therefore, the requirement of a signal in V0A and V0C strongly affects the trigger efficiency for the pp at 13 TeV and 5.02 TeV.

System	$\sqrt{s}$	Trigger	Efficiency	Signal condition
pp	2.76 TeV	MB_{OR}	93.8%	V0A or V0C or SPD
pp	5.02 TeV	$V0_{AND}$	81.4%	V0A and V0C
pp	7 TeV	MB_{OR}	92.9%	V0A or V0C or SPD
pp	13 TeV	$V0_{AND}$	80.4%	V0A and V0C

Table 3.2: Online trigger conditions applied in each data taking period of pp collisions used in this thesis.
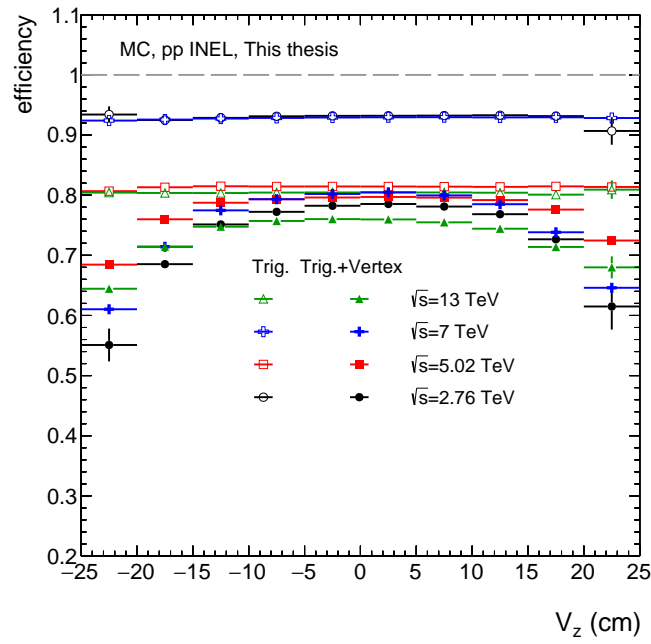
Figure 3.1: Trigger and primary vertex reconstruction efficiencies as a function of the *z*-position of the primary vertex and for different pp collision energies. Values are obtained from PYTHIA+GEANT event generator.
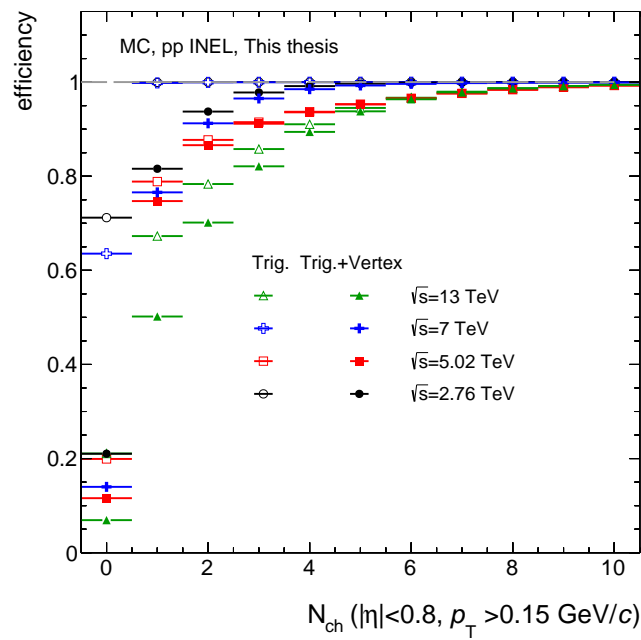

Figure 3.2: Trigger and primary vertex reconstruction efficiencies in pp collisions as a function of the number of charged particles in the acceptance ($|\eta| < 0.8$ and $p_{\mathrm{T}} > 0.15\,\mathrm{GeV}/c$) .

Acceptance and kinematic ranges

Events that satisfy the trigger condition, as described in Section 4, were selected and some additional vertex position selections are applied to them . The resulting reconstructed tracks in the ITS and TPC detectors are ultimately used in the analysis.

An acceptance condition in pseudo-rapidity of $|\eta| < 0.8$ is applied to the reconstructed tracks, motivated by the acceptance coverage of the TPC and ITS detectors. Events with a primary vertex reconstructed within $\pm$ 10 cm around the center of the detectors were selected. The selection criteria on the vertex aims to remove parasitic collisions from satellite bunches. Both select the majority of reconstructed tracks as shown in Figure 3.3.

The $z-$position distribution of the primary vertex for pp collisions at $\sqrt{s}$ = 5.02 TeV is shown in the right side of Figure 3.3, the colored area accounts for about 90% fraction of the events that are selected within $|V_z| < 10$ cm.
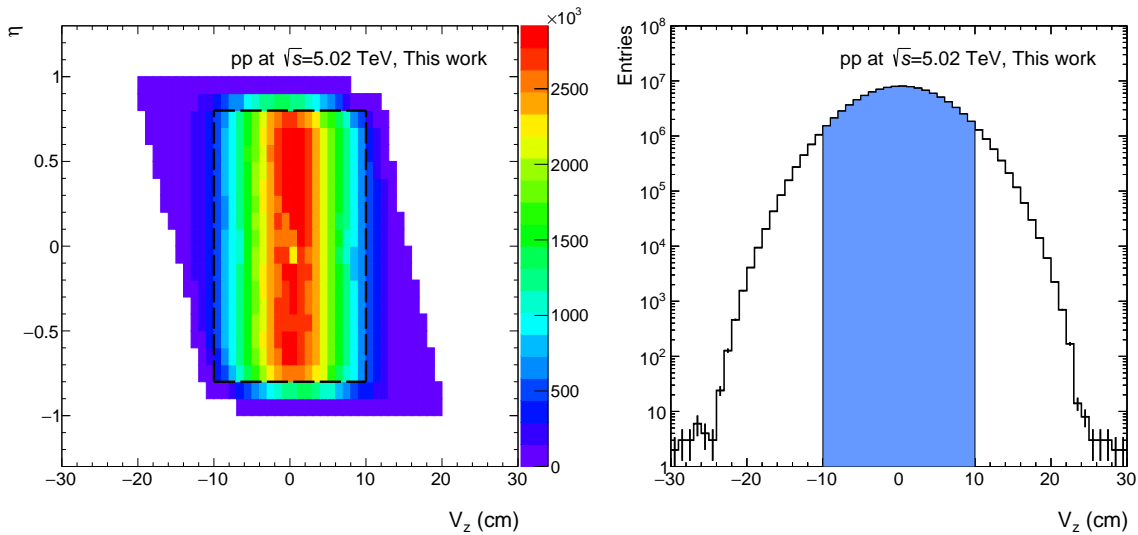

Figure 3.3: **Left**: Two dimensional distribution of the pseudorapidity vs z-position of the primary vertex. The black box represents the acceptance region used in this analysis. **Right**: Primary vertex distribution along the z-position. The colored area indicates the acceptance region where events were selected.

Track selection

In ALICE, there is a standard track selection criteria that are optimized to select primary particles and to guarantee optimal track quality. Identical criteria are applied for all data sets and MC simulations, since no drastic changes in performance of the detectors occurred. The track selection criteria in this analysis aims to fulfill mainly four requirements: reduce the amount of fake tracks or multiple reconstructed tracks, low contamination by secondary particles, the best track quality and p_T resolution possible. To achieve these four goals, corrections to the raw yield distributions are implemented and will be discussed in Section 7.

For example, a high tracking efficiency can be achieved by using TPC only reconstructed tracks when compared to the efficiency that uses global tracks (reconstructed using TPC-ITS), but exhibit a larger contamination by secondaries and worse p_T resolution. The optimal combination of track selection [86–89], used in this analysis, is summarized in Table 3.3.

TPC Selection criteria	Condition
TPC refit	required
χ^2 per TPC cluster	$\chi^2_{TPC}/n_{cl} \leq 4$
Geometric length cut	(3, 130, 1.5, 0.85, 0.7)
ratio of crossed rows over findable clusters in TPC	$n_{\mathrm{rows}}/n_{\mathrm{findable}} \geq 0.8$
fraction of shared TPC clusters	$n_{\mathrm{shared}}/n_{cl} \leq 0.4$
ITS Selection criteria	**Condition**
ITS refit	required
χ^2 per ITS cluster	$\chi^2_{ITS}/n_{ITS} \leq 36$
Number of hits in the SPD	$n_{SPD} \geq 1$
Number of hits in the ITS	$n_{ITS} \geq 2$
Selection of primaries	**Condition**
DCA to primary vertex in z	$\mathrm{DCA}_z \leq 2$ cm
DCA to primary vertex in xy	$\mathrm{DCA}_{xy} \leq 7\sigma_0$
Golden cut	**Condition**
χ^2 between TPC-ITS and TPC constrained track	$\chi^2_{TPC-ITS} \leq 36$

Table 3.3: List of track quality criteria and the default values used in the analysis. For pp collisions at $\sqrt{s}$ = 2.76 TeV, the maximal number of hits in the ITS was 4, since the data was reconstructed without SDD due to a problem in the cooling system [90].

TPC selection criteria

To select good reconstructed tracks in the TPC we require: the TPC track refit[2], the tracks to have a maximum limit value of 4 for χ^2 per TPC cluster, also the ratio of crossed TPC pad rows to the number of findable TPC clusters (maximum number of clusters which can be assigned to a track in the TPC fiducial volume, excluding the information from the pads at the sector boundaries) is required to be larger than 0.8, and the fraction of TPC clusters shared with another track lower than 0.4 [86–89]. In addition, tracks are required to have a minimal length L (in cm) in the TPC readout plane [91] with the following characteristics:

- A geometrical length (L) larger than $A - B \cdot p_T{}^C$, with $A = 130$ cm, $B = 1.0$ cm·c/GeV, $C = -1.5$ and p_T in units of GeV/c. The length calculation excludes the information from the pads at the sector boundaries located up to ~ 3 cm from the sector edges.

---

[2]When the track reconstruction algorithm is applied twice, from the inner to the outer wall of the TPC and vice versa.

- A length expressed by the number of crossed TPC rows larger than $0.85 \cdot L$; a TPC readout pad row is considered crossed if there is a cluster in any of its neighboring two rows.

- The length expressed by the number of TPC clusters (one cluster per pad row) larger than $0.7 \cdot L$.

Figure 3.4 shows the distributions of each relevant TPC selection criteria used for track selection for pp data and the respective MC simulation at $\sqrt{s} = 5.02$ TeV. The distributions are integrated over the kinematic range of $0.15 < p_{\mathrm{T}} < 50$ GeV/c and, therefore they are dominated by the low p_{T} tracks.
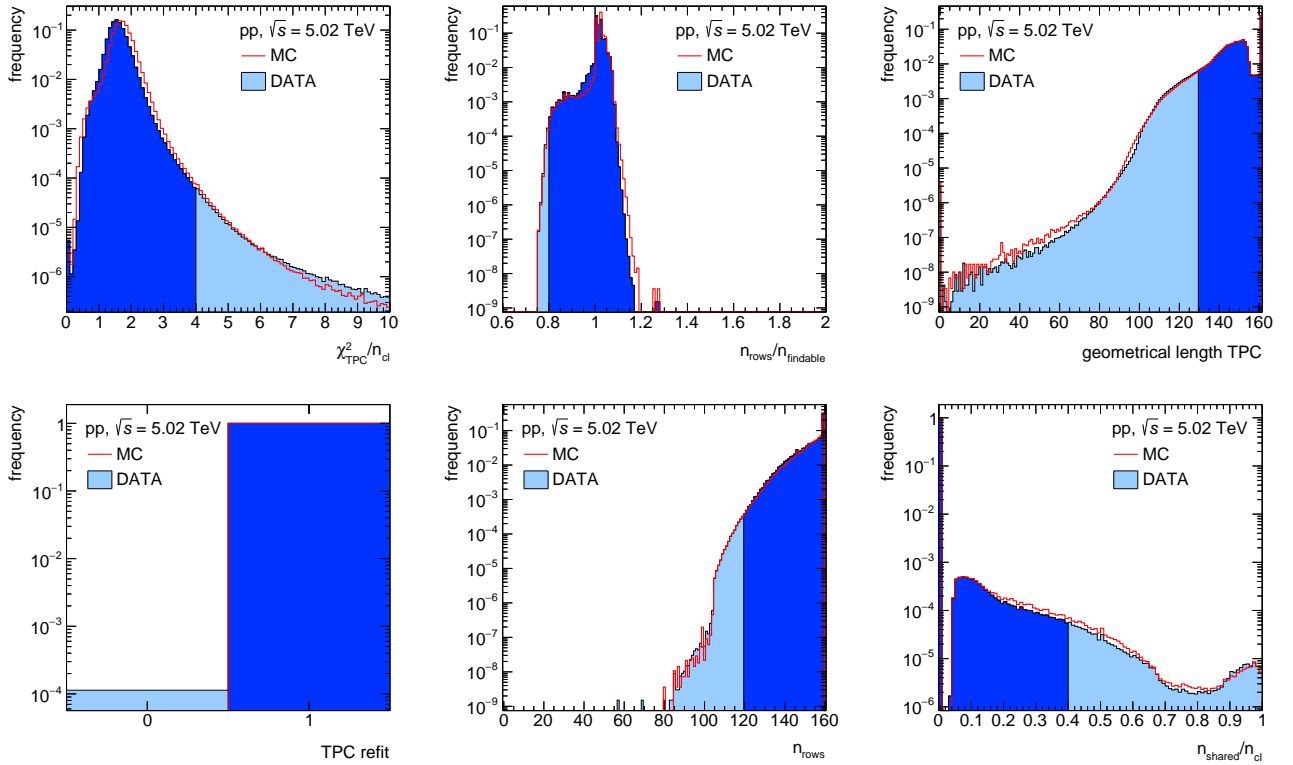

Figure 3.4: Distribution of TPC selection criteria applied to the tracks at $\sqrt{s} = 5.02$ TeV. All distributions are normalized to an integral equal to unity. Each distribution includes all tracks that fulfill the remaining track selection criteria and the blue area represents the ranges selected by each criteria.

ITS selection criteria

The track selection criteria for the ITS requires at least 2 hits in the detector (ITS refit), from which at least one hit has to be in the two innermost (SPD) layers. The fit quality for the ITS track points must satisfy the condition $\chi^2_{ITS}/n_{\mathrm{hits}} < 36$. Tracks that have a large ratio of fit quality over the number of hits are likely to have wrong clusters assigned and as a consequence it can influence the p_{T} resolution at large p_{T} [86–89]. Therefore these particular tracks are removed from the analysis.
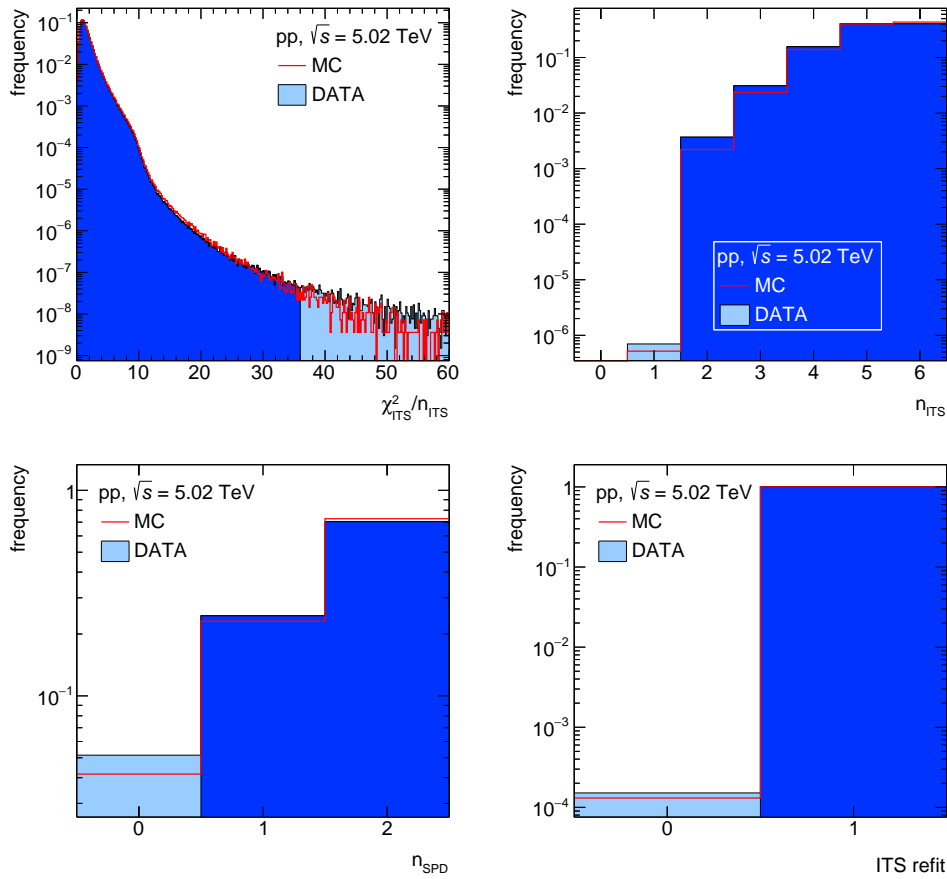
Figure 3.5: Distribution of ITS selection criteria applied to the tracks at $\sqrt{s} = 5.02$ TeV. All distributions are normalized to an integral equal to unity. Each distribution includes all tracks that fulfill the remaining track selection criteria and the blue area represents the ranges selected by each criteria.

Selection of primary particles

The Distance of Closest Approach (DCA) is a p_{T} dependent selection criteria which provides the point where the track is closest to the primary vertex in the radial direction (DCA$_{xy}$), required to be smaller than seven standard deviations (σ_0) of the impact parameter resolution. The selection criteria on DCA is necessary to improve the purity of primary charged particles:

$$\mathrm{DCA}_{xy} \leqslant 7 \cdot \left(26 + \frac{50}{p_{\mathrm{T}}}\right) \mu m, \tag{3.1}$$

$$\mathrm{DCA}_{xy} \leqslant 7 \cdot \sigma_0$$

In the longitudinal direction, the selection criteria is DCA$_z$ < 2 cm. It removes spiraling tracks due to the magnetic field in the detector. Figure 3.6 shows an example of DCA$_{xy}$ (Transversal view) and DCA$_z$ (Longitudinal view) geometry when a track traverses the ITS detector. The DCA$_{xy}$ distribution for data and MC is shown in Figure 3.7, where the tracks selected in the analysis are those in the shaded area (DCA$_{xy} \leqslant 7 \cdot \sigma_0$).
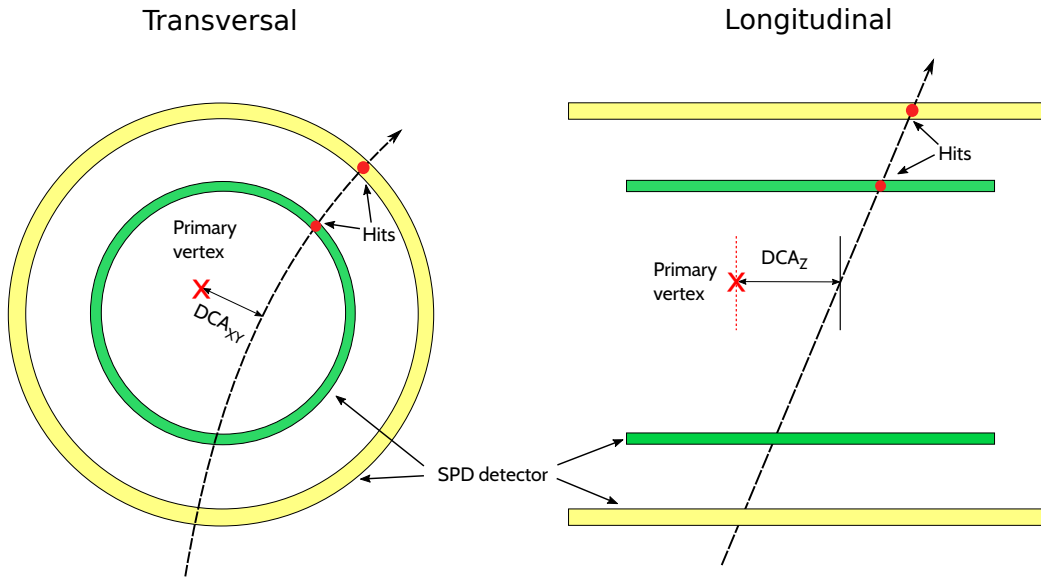
Figure 3.6: Schematic view of the impact parameters in the transversal (DCA_{xy}) and longitudinal (DCA_z) directions.
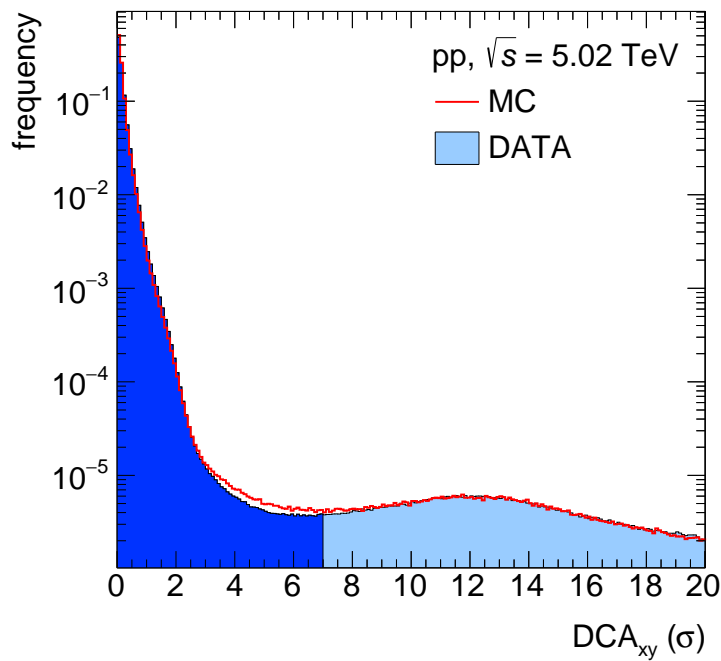

Figure 3.7: Frequency of the DCA_{xy} in data and MC. Tracks in the dark shaded area ($\sigma < 7$) are considered in the analysis.

TPC-ITS χ^2

The $\chi^2_{TPC-ITS}$ selection criteria (also known as "golden cut") compares the tracking information from the combined ITS and TPC track reconstruction algorithm and the tracks derived only from the TPC, which is constrained by the interaction vertex point. The $\chi^2_{TPC-ITS}$ is calculated using the following formula:

$$\chi^2_{TPC-ITS} = (\vec{v}_{TPC} - \vec{v}_{TPC-ITS})^T \cdot \Sigma^{-1} \cdot (\vec{v}_{TPC} - \vec{v}_{TPC-ITS}) \tag{3.2}$$

where $\vec{v}_{TPC}$ and $\vec{v}_{TPC-ITS}$ are the measured track parameter vectors v= $(x, y, z, \theta, \phi, 1/p_T)$ and Σ^{-1} is the inverse of the covariance matrix, which is calculated by treating both tracks as uncorrelated as the sum of the individual covariances matrices ($\Sigma = \Sigma_{TPC} - \Sigma_{TPC-ITS}$) [92]. This selection criteria becomes relevant for high-p_T tracks and removes fake tracks originating from spurious matches of low-p_T particles in the TPC to hits in the ITS, resulting in an imprecise or incorrect momentum assignment.

All track candidates with $\chi^2_{TPC-ITS} > 36$ are rejected from the analysis, and only those below that limit are accepted. The maximum cut value is optimized to select good quality tracks that come from the ITS. Figure 3.8 shows the selection criteria distribution where the shaded area represents the 99% of the total track sample.
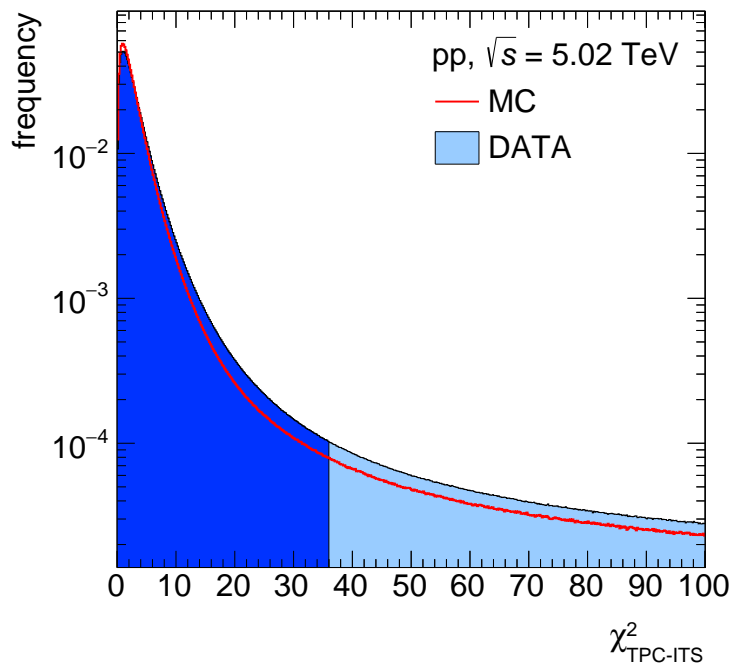

Figure 3.8: Golden cut distribution for DATA and MC for pp at $\sqrt{s} = 5.02\,\text{TeV}$. Tracks that fulfill the condition $\chi^2_{TPC-ITS} < 36$ are considered in the analysis (dark shaded area).

Corrections

From the reconstructed data, the raw transverse momentum distribution can be obtained but it needs still to be corrected to account for the detector effects. The corrections that affect the shape of the distribution are the tracking efficiency, contamination by secondaries and p_T resolution. The corrections that have influence on the overall normalization are the trigger and vertex efficiency, and the measured cross sections. A detailed description of each correction will be given in this section, together with a brief explanation of the implementation on the raw p_T distribution.

Tracking efficiency

The correction for the reconstruction efficiency of primary charged particles is based on Monte Carlo information from simulated data using the PYTHIA6 and PYTHIA8 event generators, together with the detector simulation (GEANT3) for which, the same reconstruction algorithms that were used in data are implemented in MC.

The overall efficiency (tracking efficiency × acceptance) uses generated and reconstructed particles in the kinematic range of $0 \leq \phi < 2\pi$, $|\eta| < 0.8$ and $p_\mathrm{T} > 0.15$ GeV/c. It is calculated as follows:

$$\varepsilon(p_\mathrm{T}, \eta) = \frac{\mathrm{N}^{\mathrm{MC}}_{\mathrm{Rec,prim}}(p_\mathrm{T}, \eta)}{\mathrm{N}^{\mathrm{MC}}_{\mathrm{Gen,prim}}(p_\mathrm{T}, \eta)} \tag{3.3}$$

where $\mathrm{N}^{\mathrm{MC}}_{\mathrm{Rec,prim}}$ is the number of reconstructed primary tracks and $\mathrm{N}^{\mathrm{MC}}_{\mathrm{Gen,prim}}$ is the number of generated primary tracks. The tracking efficiencies for the four collision energies studied here are shown in Figure 3.9, with an overall value between 60% and 70% for high-p_T tracks. The characteristic shape at around $p_\mathrm{T} \approx 1\,\mathrm{GeV}/c$ is caused from the track length requirement, since tracks in this transverse momentum range are more likely to cross the TPC sector boundaries (excluded from the analysis) and are thus reconstructed with lower tracking efficiency. The characteristic rise at low p_T is due to the strong track curvature caused by the magnetic field and the energy loss when traversing the detector material.
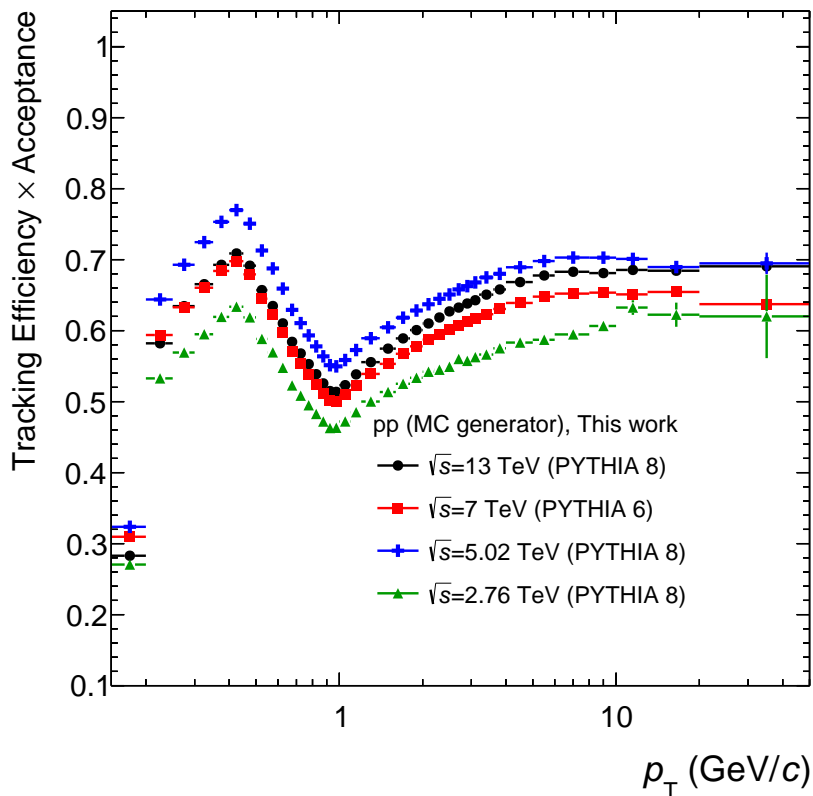
Figure 3.9: Tracking efficiency as a function of p_T for pp collisions at $\sqrt{s}$ = 2.76 TeV, 5.02 TeV, 7 TeV and 13 TeV simulated with PYTHIA and GEANT.

The differences in the tracking efficiencies between the collision energies comes mainly from the updates in the track reconstruction codes in ALICE over the time. The oldest reconstructed data set analyzed is for pp collisions at $\sqrt{s}$ = 2.76 TeV, while for $\sqrt{s}$ = 5.02 TeV data the latest reconstruction tools were used.

Particle composition correction

It is known that MC event generators do not describe well the production of the individual identified charged particles in the bulk (at low momenta), especially the strange hyperons are underestimated substantially [93]. For recent PYTHIA 8 tunes, the $\Sigma^+(1385)$ and $\Sigma^-(1385)$ hyperons and their antiparticles are underestimated by a factor between 2 and 3. Therefore, an additional correction to our MC generators is needed. This correction is called particle composition correction and uses the measured production of charged pions, kaons, protons and lambda baryons (as a proxy for charged hyperons), to calculate the abundances in data and later determine the tracking efficiency by reweighting the primary particle composition.

In Fig. 3.10, the relative particle abundances measured by ALICE in pp collision at $\sqrt{s}$ = 7 TeV and those from MC simulations in pp at $\sqrt{s}$ = 5.02 TeV are shown. Charged protons, kaons and pions were measured from p_T = 0.3, 0.2 and 0.15 GeV/c to 20 GeV/c [94], respectively. Since the

transverse momentum spectrum for Σ^+ ($c\tau = 2.4$ cm) or Σ^- ($c\tau = 4.4$ cm) hyperons has not been measured in ALICE, it is constructed by using the measured spectrum of Λ ($c\tau = 7.9$ cm) baryons [45] scaled by the ratio of $\Sigma^\pm$ to Λ from MC generators, the following equation was used to obtain the reconstructed yield for hyperons:

$$N_{\Sigma^\pm}^{Const.} = \frac{N_{\Sigma^\pm}^{MC}}{N_\Lambda^{MC}} \cdot N_\Lambda^{Data} \tag{3.4}$$

where N_i represents the yield of $\Sigma^\pm$ or Λ accordingly, the ratio $N_{\Sigma^\pm}^{MC}/N_\Lambda^{MC}$ is calculated from PYTHIA simulations at $\sqrt{s} = 7\,\text{TeV}$ and N_Λ^{Data} is the Λ measured spectrum [45]. The relative abundance for other particle species like electrons, muons, Ξ^- and Ω^- are grouped in the rest sample, and is obtained only from MC simulations without further modification since the influence of this sample on the final result is smaller than 1%.
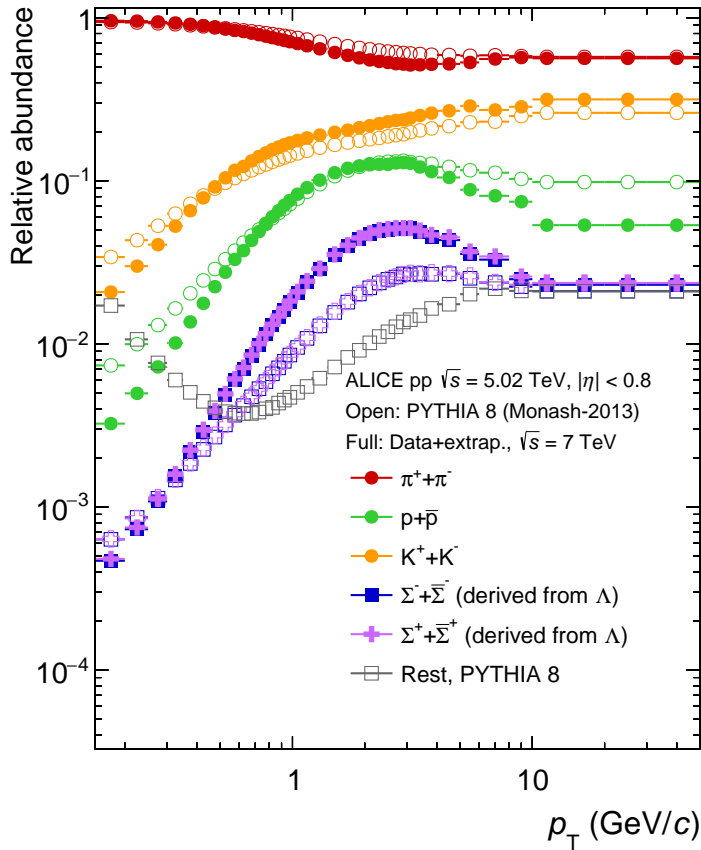

Figure 3.10: Relative particle abundances as a function of p_T in Monte Carlo (open symbols) and in data (full symbols), for pp at $\sqrt{s} = 5.02$ TeV and $\sqrt{s} = 7$ TeV, respectively.

All the relative particle abundances are presented for the p_T range of 0.15-50 GeV/c, but not all the yields of identified particles have been measured in the same p_T range. Therefore, the measured transverse momentum spectra of kaons, protons and Λ was extrapolated down to $p_\text{T} = 0.15$ GeV/c using a parametrization proposed by Bylinkin and Rostovtsev [95]. The parametrization is a qualitative model which tries to describe inclusive pseudorapidity distributions and transverse momentum

spectra by considering a "thermal" and a "hard" components for hadroproduction.

At high transverse momentum ($p_T > 20\,\text{GeV}/c$), above the limit of measured yields, the relative abundances are assumed to be independent on p_T, as motivated by pQCD [96]. Relative particle abundances measured in pp collisions at $\sqrt{s} = 7\,\text{TeV}$ are used to reweight the traking efficiency determined for all the pp collision energies used in this thesis ($\sqrt{s} = 2.76\,\text{TeV}$, $5.02\,\text{TeV}$, $7\,\text{TeV}$ and $13\,\text{TeV}$), based on the experimental knowledge that the energy dependence is weak [45].

The tracking efficiency for each particle species is shown in Figure 3.12. The efficiency is particularly species-dependent for $p_T < 0.5\,\text{GeV}/c$ due to differences in ionization energy loss in the detector material, decay probability or hadronic interaction cross-section. For Σ hyperons, the efficiency below $10\,\text{GeV}/c$ is negligible, essentially because they decay before they reach the detectors. When they have larger p_T, they can be detected with increasing efficiency. The tracking efficiency for the rest (electrons, muons and Ξ and Ω) is also shown.

In order to reduce the statistical fluctuations in the tracking efficiency at high p_T and to study the particle dependence part the components had to be disentangled and studied separately (dependent and independent of particle species). The survival probability $P(p_T, d)$ of a particle with a mass m and mean proper lifetime τ survives a minimal distance d before it decays, and it is calculated as:
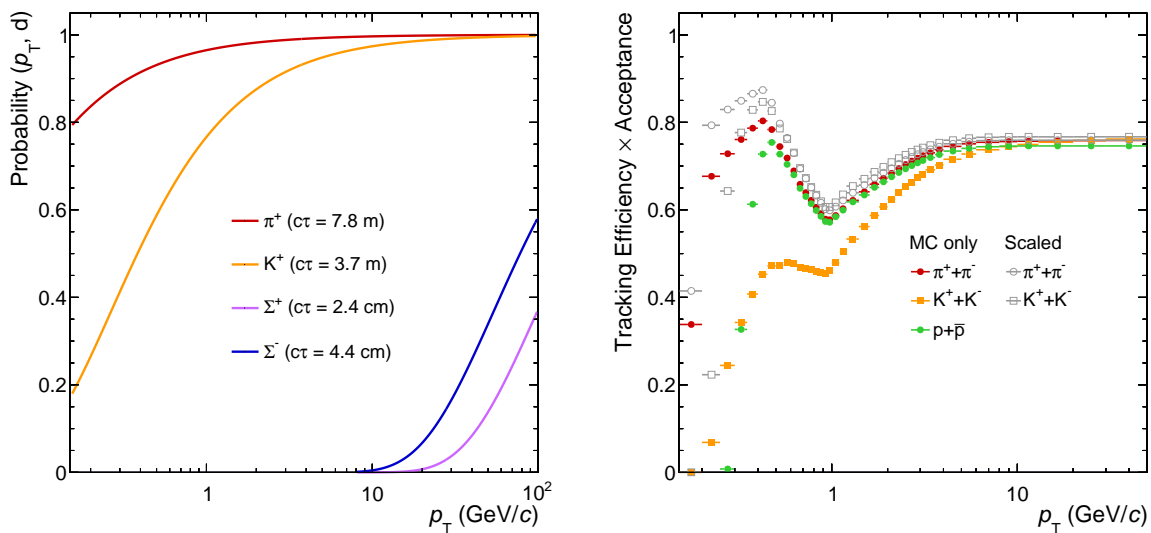
$$P(p_T, d) = e^{-\frac{d \cdot m}{p_T \cdot \tau}} \tag{3.5}$$

Figure 3.11: **Left**: Survival probability function for charged pions, kaons and Σ hyperons. **Right**: Tracking efficiency scaled by the probability function.

On the left side of Figure 3.11, the survival probability for different particle species is shown. On the right side, the scaled efficiencies by their corresponding probability are shown for the whole p_T range. After extracting the particle dependent part, the tracking efficiency can be described by an exponential function at $p_T > 1$ GeV/c:

$$f(p_T) = A \left(1 - B e^{-C p_T}\right) \tag{3.6}$$

where A,B and C are free parameters. Then, the parametrization for each species is scaled back according to their survival probability (eq.3.5) to obtain a tracking efficiency with no statistical errors and no fluctuations, as shown in Figure 3.12. This, at the end reduces the statistical errors in the fully corrected p_T-spectrum. Variations on the parametrization fit range at low and high-p_T are assigned as systematic uncertainties and will be explained in Section 3.5.
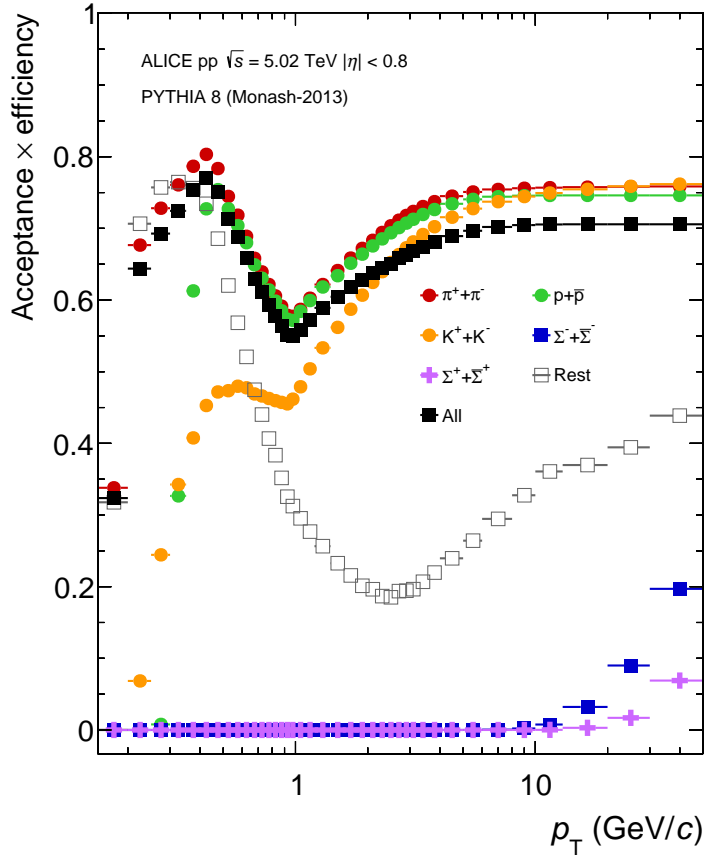

Figure 3.12: Combined tracking efficiency and acceptance as a function of p_T for different particle species and for all charged particles, obtained from MC simulations of pp collisions at $\sqrt{s} = 5.02\,\text{TeV}$. The different acceptance×efficiency for Σ^+ ($c\tau = 2.4$ cm) and Σ^- ($c\tau = 4.4$ cm) is due to their different life times.

Based on the knowledge of particle abundances and tracking efficiencies for each particle species, we can calculate the corrected efficiency for inclusive charged particles ($\varepsilon_{\text{incl}}^{\text{Corr}}(p_T)$), and is obtained using the following equation:

$$\varepsilon_{incl}^{Corr}(p_T) = \varepsilon_{Rest}^{MC}(p_T) \cdot f_{Rest}^{MC}(p_T) + \sum_{i=\pi,K,p,\Sigma} \varepsilon_i^{MC}(p_T) \cdot F_i(p_T) \cdot (1 - f_{Rest}^{MC}(p_T)) \qquad (3.7)$$

where $\varepsilon_i^{MC}(p_T)$ represents the efficiency for each particle species (π, K, p, Σ and *Rest*), $f_{Rest}^{MC}(p_T)$ is the particle abundance fraction of the *rest* sample and $F_i(p_T) = N_i/(N_\pi + N_K + N_p + N_\Sigma)$ is the fraction for each species, with the condition that $\sum_i F_i(p_T) = 1$.

Figure 3.13 shows the combined tracking efficiency and acceptance obtained from MC simulations and the one after applying the particle composition correction, for pp collision at $\sqrt{s} = 2.76$ TeV,

5.02 TeV, 7 TeV and 13 TeV. The effect of the reweighting on the efficiency correction is shown in the bottom panel. The largest correction value is at $p_T \approx 2.5\,\text{GeV}/c$, caused mainly because the Σ hyperon fractions at this momenta have the largest discrepancy with MC generators. The maximum correction factor for pp collisions at $\sqrt{s} = 13$ TeV, 7 TeV, 5.02 TeV and 2.76 TeV was found to be 8%, 3%, 6% and 5%, respectively. An extensive and detailed analysis on the particle composition correction is presented in [97].

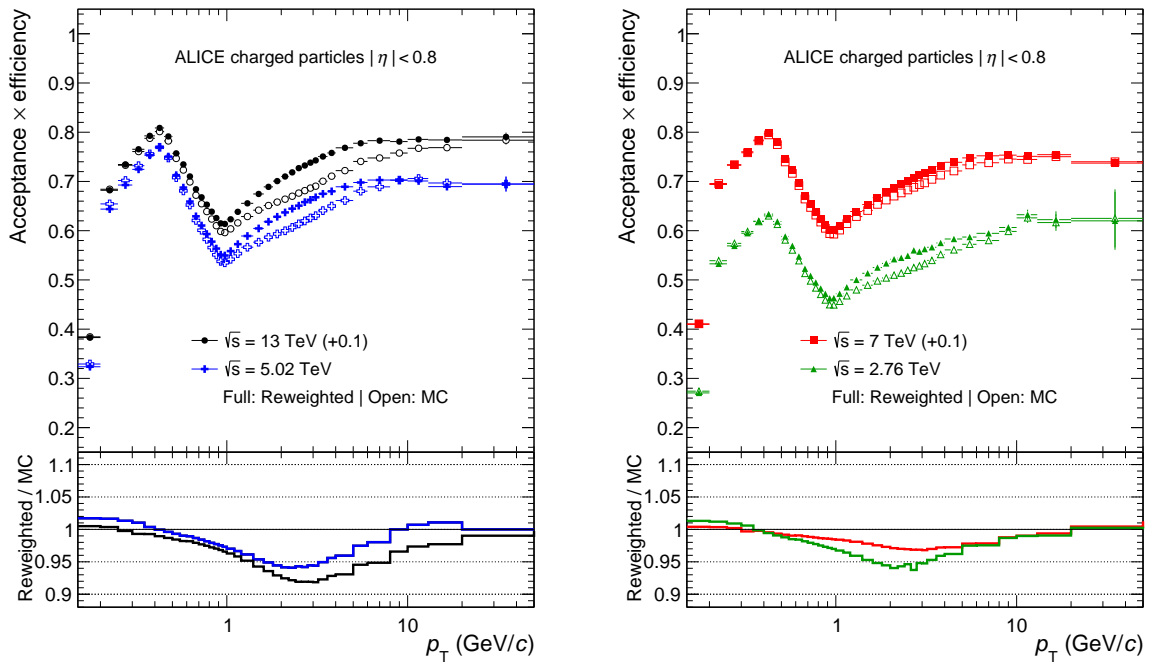
Figure 3.13: **Left**: Combined tracking efficiency and acceptance as a function of p_T, reweighted by particle composition and the efficiency obtained directly from MC simulations for pp collisions at $\sqrt{s} = 13$ TeV and 5.02 TeV. The correction factor (ratio of the two efficiencies) is shown in the bottom panel. **Right**: Similarly for pp collisions at $\sqrt{s} = 7$ TeV and 2.76 TeV.

Contamination by Secondaries

Secondary particles are defined as those coming from weak decays of kaons, Λ hyperons and muons, and particles originating from interactions in the detector material [81]. The particles selected after applying the track selection criteria not only contain primary particles, but still few secondary particles remain and need to be subtracted from the data sample. Figure 3.14 shows the contamination obtained from MC for all energies. A similar distribution over the whole p_T range $(0.15 - 50\,\text{GeV}/c)$ was found. At low p_T, the contamination has the largest value $\sim 6.5\%$ and it reduces as p_T increases, reaching a minimum of $1 - 2\%$. This decreasing trend is a consequence of the steeply falling spectra and that the daughter particles only take a fraction of the energy of the mother particle [98].
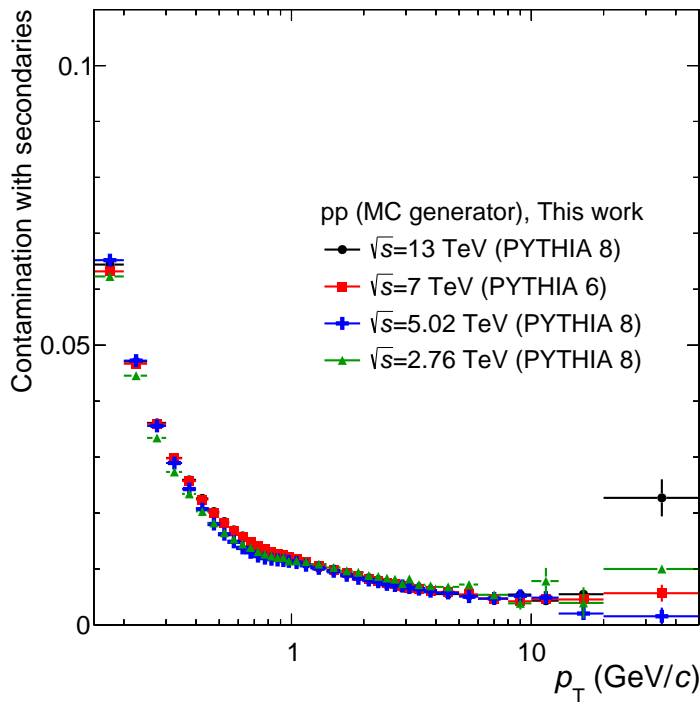

Figure 3.14: Contamination from secondary particles estimated from Monte Carlo simulations for pp collisions at $\sqrt{s} = 2.76\,\text{TeV}$, $5.02\,\text{TeV}$, $7\,\text{TeV}$ and $13\,\text{TeV}$.

A considerable fraction of secondary particles from weak decays come from the decay of neutral strange particles like K^0 or Λ. Since the MC event generators underestimate the yield of strange particles, the fraction of primaries and secondaries is estimated using the transverse impact parameter distributions (DCA_{xy}) of particles in data and Monte Carlo simulations. The assumption is that the DCA_{xy} distributions for primaries and secondaries have a different shape especially in the tails, essentially because secondary particles from decays and from interactions with the detector material are originated away from the primary vertex position, having as a consequence a broader DCA_{xy} distribution.

The tracks are selected without constrains in the DCA_{xy}, DCA_z and without applying the global $\chi^2_{TPC-ITS}$, in order to have the complete DCA_{xy} distribution. This implies to remove the ITS information, which affects the pileup rejection method. Therefore, an extra selection criteria to

reject tracks from pileup events was introduced. This new pileup rejection criteria is based on the difference between the time measured in TOF and the expected arrival time.

Figure 3.15 shows the DCA_{xy} distributions for data, primaries and secondaries for low transverse momentum ($0.1 - 0.5\,\mathrm{GeV}/c$). The distribution for primaries shows a prominent peak, similar to data, centered at $DCA_{xy} = 0$. In the secondary particles distribution, that represents the collection of secondaries from decays and from detector material interaction, a larger width compared to that from primaries or data is found. In the lower panel, the ratio fit to data is shown with a maximum deviation observed of $\pm 10\%$, value that is later used for the systematic uncertainty calculation.
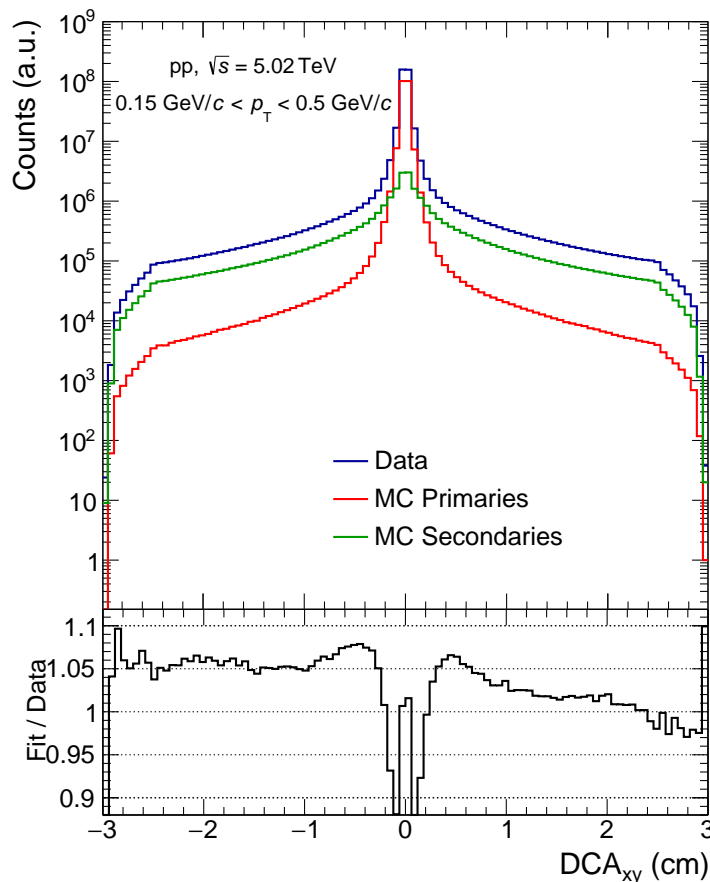

Figure 3.15: DCA_{xy} distributions for data, primary and secondary particles from MC simulations for pp at $\sqrt{s} = 5.02\,\mathrm{TeV}$. The distributions are shown for tracks with a transverse momentum in the range of $0.15\,\mathrm{GeV}/c < p_\mathrm{T} < 0.5\,\mathrm{GeV}/c$. In the lower panel, the ratio fit to data is shown.

To obtain the amount of primary and secondary particles in data, the measured distribution was fitted with a linear combination of DCA_{xy} (templates) for primaries and secondaries. A minimization procedure was used to optimize the relative weights in order to obtain the closest relation to the data distribution. The statistical uncertainties allow this procedure to be applied for three p_T ranges; $0.1 - 0.5\ \mathrm{GeV}/c$, $0.5 - 1.0\ \mathrm{GeV}/c$ and $1.0 - 1.5\ \mathrm{GeV}/c$. For larger p_T, it is assumed to follow the same trend.

In Figure 3.16, the amount of primaries and secondaries after the template fits are shown as fractions. The true amount of secondaries in data is larger than the one predicted by MC. At low-p_T,

secondaries from data account for 13% while the contamination from MC is around 10%. At high-p_T, the contamination is negligible. To obtain a p_T dependent correction factor for secondaries, the ratio of fractions from data and MC is calculated. This ratio is shown in the lowest panel of Figure 3.17 together with the contamination from secondary particles for each pp collision energy studied. The correction factors are found to be similar for pp collisions at $\sqrt{s}$ = 13 TeV, 7 TeV and 5.02 TeV that go from 1.2 at low-p_T to 1.6 for $p_T > 1\,\mathrm{GeV}/c$. The largest correction is for pp collisions at $\sqrt{s}$ = 2.76 TeV, it is between 1.5 and 1.9, above $1\,\mathrm{GeV}/c$.
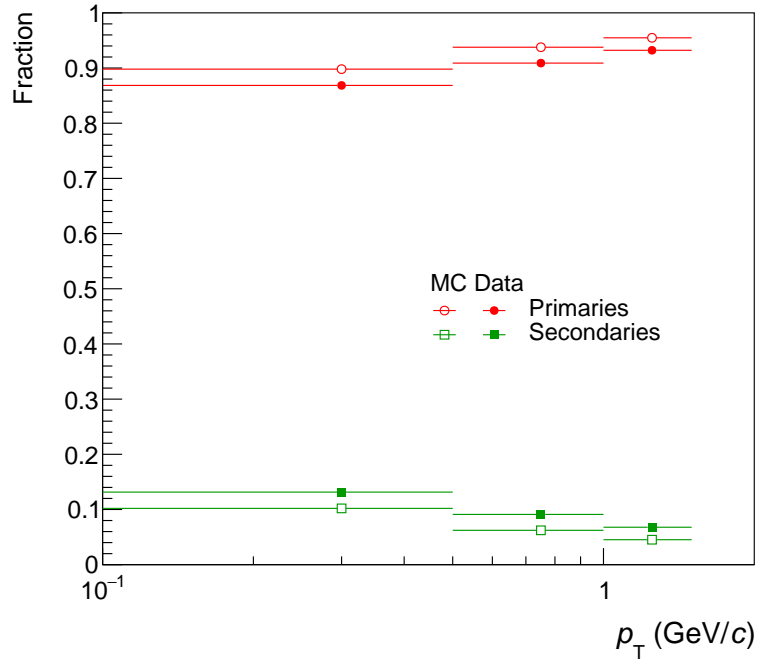

Figure 3.16: The fraction of primary (red) and secondary (green) particles for three p_T ranges. The full markers correspond to fractions obtained from fitting the DCA$_{xy}$ distributions and the empty markers are the values obtained directly from the MC generator.
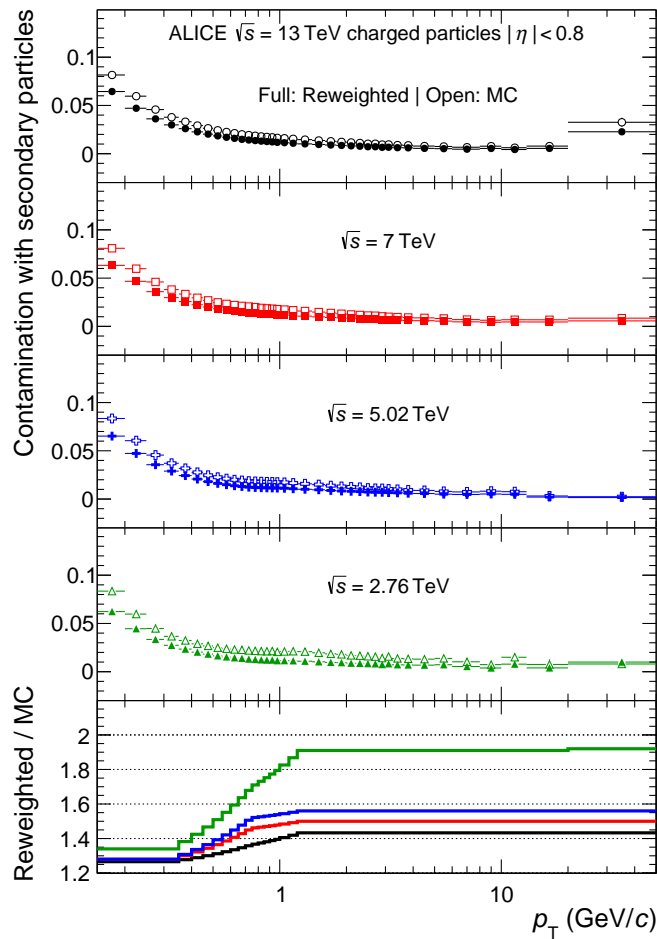
Figure 3.17: Contamination from secondary particles estimated from MC simulations and from the impact parameter fits in data (DCA$_{xy}$) for pp collisions at $\sqrt{s}$ = 13 TeV, 7 TeV, 5.02 TeV and 2.76 TeV. The total effect of the reweighting of secondary paricles is shown in the bottom panel.

p_T **Resolution correction**

The measurement of the p_T distributions at very large momenta needs a correction on the p_T resolution, since the transverse momentum of charged particles is reconstructed from the track curvature measured in the ITS and the TPC. As the track goes higher in p_T, the curvature is more straight.

During the reconstruction procedure as explained in Section 4, the Kalman filter converts hits in the TPC and ITS into tracks, providing track parameters and error estimates (covariance matrix). The inverse of the transverse momentum $1/p_T$ is one of this parameters and is directly related to the track curvature.

An extra contribution to the p_T resolution correction comes from the difference in tracking performance between positive and negative charged particles, due to a possible residual miss-alignment. Figure 3.18 shows the q/p_T distribution for positive and negative tracks where is expected to have a minimum at zero. The q/p_T data was fitted with a power law function and the minimum is found to be shifted from zero. This shift (Δ_{1/p_T}) was found to be dependent of the azimuthal angle ϕ with

a mean and RMS value of 0.0003 c/GeV.

The relative p_T resolution ($\sigma(p_T)/p_T$) obtained in data is shown in Figure 3.19. For tracks with small transverse momentum ($p_T < 1\,\text{GeV}/c$), the resolution is dominated by multiple scattering and no significant differences between the data sets are expected. The resolution has the optimum value of $\sigma(p_T)/p_T \approx 1\%$ at $p_T = 1\,\text{GeV}/c$. At larger momenta, the resolution deteriorates and reaches between 3-4% for $p_T = 50\,\text{GeV}/c$.
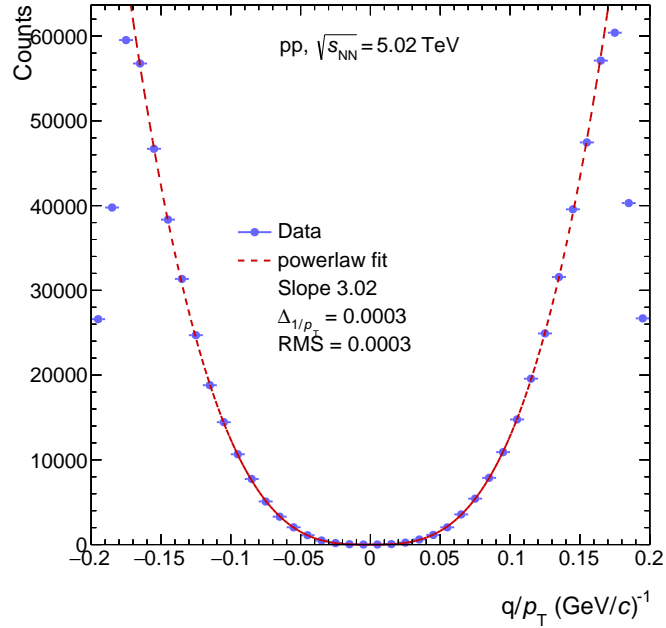

Figure 3.18: Distribution q/p_T tracks where the minimum is obtained by fitting a power law function. An azimuthal angle dependence is found for the shift.

To obtain the resolution correction for the measured spectra, a bin-by-bin correction is implemented as an approximation to a full unfolding. The procedure is described below and relies on the observation that the smearing with the finite p_T resolution has a small effect on the spectrum.

The measured spectra is parametrized by a power law function in the range $10\,\text{GeV}/c < p_T < 50\,\text{GeV}/c$. This resolution is folded with the p_T resolution obtained from the covariance matrix of the track fitting algorithm. The p_T-dependent correction factors are extracted from the ratio of the folded to the unfolded spectra and applied (bin-by-bin) to the measured p_T spectrum. The correction factors obtained with this procedure are shown in Figure 3.20. For pp at $\sqrt{s} = 13\,\text{TeV}$, 7 TeV and 5.02 TeV, the correction goes from less than 1% for tracks below $20\,\text{GeV}/c$, to a maximum of 2% at $50\,\text{GeV}/c$. The largest correction at high p_T is for pp at $\sqrt{s} = 2.76\,\text{TeV}$, that reaches a value of 8%. The origin of this large correction comes from the track-reconstruction procedure, where a miss-calibration was present for the 2010 data, affecting the high-p_T particles, and which was later corrected for run 2 program.

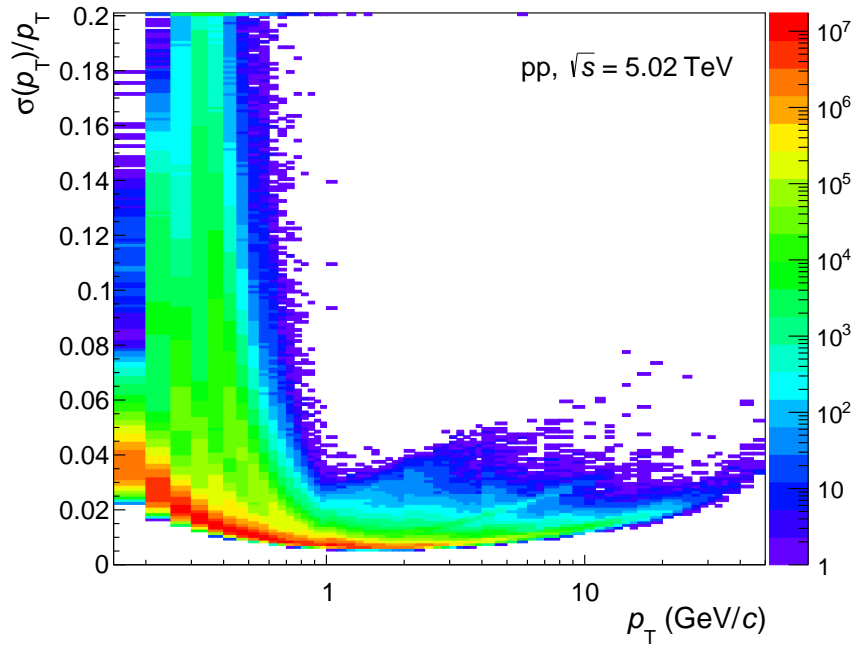Figure 3.19: Transverse momentum resolution $\sigma(p_T)/p_T$ as a function of p_T for pp collisions at $\sqrt{s} = 5.02\,\text{TeV}$.
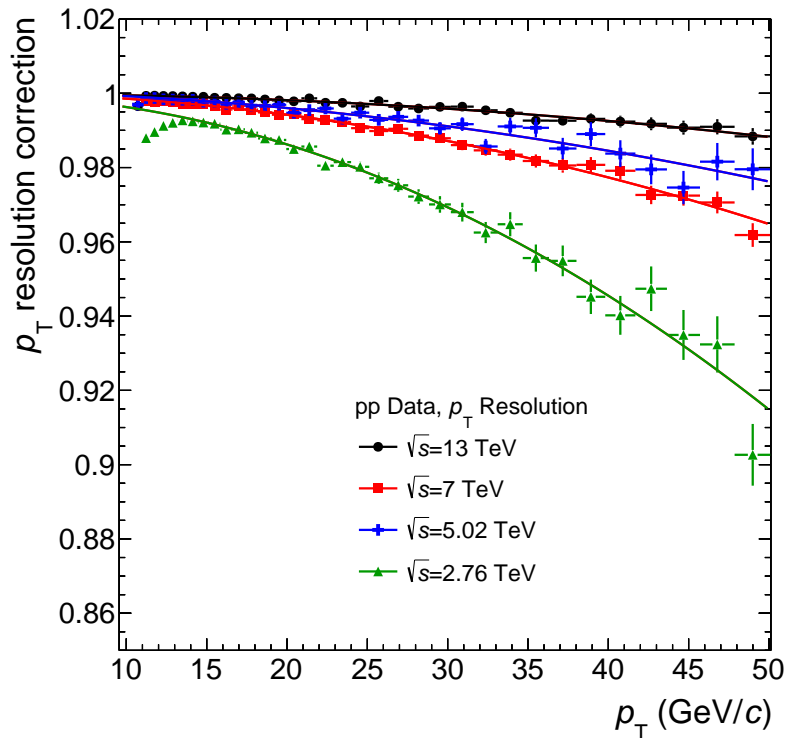

Figure 3.20: Resolution correction factors as a function of p_T applied to the spectra in each pp collision energy.

Trigger efficiency and cross sections

The trigger efficiency (ε_trig) can be obtained from the measurement of the inelastic ($\sigma^\text{pp}_\text{INEL}$) and visible cross sections ($\sigma^\text{pp}_\text{vis}$), or from MC simulations. The visible cross section, seen by a given detector or set of detectors with an specific trigger condition, is a fraction of the total inelastic cross section $\sigma^\text{pp}_{vis} = \varepsilon_{trig} \times \sigma^\text{pp}_\text{INEL}$. The efficiencies strongly depend on the trigger condition, V0$_\text{AND}$ or MB$_\text{OR}$ (see Section 4), and is generally larger for MB$_\text{OR}$. Table 3.4 shows the trigger efficiency values for pp collisions obtained from MC and from ALICE measurements [99–101].

For the differential cross section calculation, the measured cross section with the minimum-bias trigger condition ($\sigma^\text{pp}_\text{MB}$) was used. The values for $\sigma^\text{pp}_\text{MB}$ were determined using the ALICE luminosity measurements with van der Meer (vdM) scans at each pp collision energy [99, 101].

- $\sqrt{s} = 2.76\,\text{TeV}$: $\sigma^\text{pp}_\text{MB} = 55.4 \pm 1.0$ mb

- $\sqrt{s} = 5.02\,\text{TeV}$: $\sigma^\text{pp}_\text{MB} = 51.2 \pm 1.2$ mb

- $\sqrt{s} = 7\,\text{TeV}$: $\sigma^\text{pp}_\text{MB} = 62.2 \pm 2.2$ mb

- $\sqrt{s} = 13\,\text{TeV}$: $\sigma^\text{pp}_\text{MB} = 57.8 \pm 1.2$ mb

pp collision energy	Trigger efficiency		Vertex efficiency	
$\sqrt{s}$	PYTHIA	ALICE	PYTHIA	ALICE
2.76 TeV	93.8%	$88.1^{-3.5}_{+5.9}$%	88.3%	89.7%
5.02 TeV	81.4%	75.74 ± 1.9%	97.7%	94.1%
7 TeV	92.9%	$85.2^{-3.0}_{+6.2}$%	93.8%	89.1%
13 TeV	80.4%	74.48 ± 1.9%	93.8%	96.1%

Table 3.4: Trigger and vertex efficiency obtained from PYTHIA simulations and from ALICE data for pp collisions.

Corrections implementation

The implementation of all corrections described before starts with the measurement of the raw transverse momentum distribution $N_\text{raw}(p_\text{T}, \eta)$, which reflects the number of reconstructed tracks with a given transverse momentum p_T and pseudorapidity η, that satisfy the track selection criteria (see Sec.6) in events that have a reconstructed primary vertex in $|V_z| < 10$ cm. The corrected p_T distribution $N_\text{corr}(p_\text{T}, \eta)$ is calculated as follows [86–89]:

$$
\begin{aligned}
N_\text{corr}(p_\text{T}, \eta) = N_\text{raw}(p_\text{T}, \eta) \times [& C_{\varepsilon \times \text{Acc}}(p_\text{T}) \cdot S_\text{P.Comp.}(p_\text{T}) \\
& \times (1 - C_\text{Sec}(p_\text{T}) \cdot S_\text{Sec.DCA}(p_\text{T})) \\
& \times C_{p_\text{T}-\text{resolution}}]
\end{aligned}
\tag{3.8}
$$

where $C_{\varepsilon \times \mathrm{Acc}}(p_\mathrm{T})$ is the correction due to the detector efficiencies for tracks in $|\eta| < 0.8$ and corrected for the factor $S_{\mathrm{P.Comp.}}(p_\mathrm{T})$ related to the particle composition, $C_{\mathrm{Sec}}(p_\mathrm{T})$ is the percentage of secondary particles that survived our primary track selection in MC and afterwards scaled by the amount of missing secondaries (data driven) $S_{\mathrm{Sec.DCA}}(p_\mathrm{T})$. The last term $C_{p_\mathrm{T}-\mathrm{resolution}}$ is the correction for the finite resolution of transverse momentum in the detector.

The resulting corrected distribution is used to calculate the differential cross section for inelastic (INEL) pp collisions in the acceptance. It is obtained as follows [86–89]:

$$
\begin{aligned}
\frac{\mathrm{d}^2\sigma}{\mathrm{d}\eta\mathrm{d}p_\mathrm{T}} &= \sigma_{\mathrm{MB}}^{\mathrm{pp}} \cdot \frac{1}{N_{\mathrm{ev}}^{\mathrm{MB}}} \frac{\mathrm{d}^2 N}{\mathrm{d}\eta\mathrm{d}p_\mathrm{T}} \\
&\equiv \sigma_{\mathrm{MB}}^{\mathrm{pp}} \cdot \frac{1}{N_{\mathrm{ev}}^{\mathrm{rec}}} \cdot \frac{N_{\mathrm{corr}}(p_\mathrm{T},\eta)}{\Delta\eta\Delta p_\mathrm{T}} \cdot \varepsilon_{Vz}
\end{aligned}
\tag{3.9}
$$

where $\sigma_{\mathrm{MB}}^{\mathrm{pp}}$ is the minimum bias cross section (see Section 7.5), $N_{\mathrm{ev}}^{\mathrm{rec}}$ is the number of reconstructed events (fraction of the INEL events [3]), $N_{\mathrm{corr}}(p_\mathrm{T},\eta)$ is the corrected distribution of charged particles for a given η and p_T, $\Delta\eta$ and Δp_T are normalizations to the bin width and the pseudorapidity interval analyzed, respectively. ε_{Vz} represents the correction for the vertex reconstruction efficiency calculated from the ratio of events with a vertex within ± 10 cm and the events with reconstructed vertex without any further requirement. Table 3.4 summarizes the vertex efficiencies for the pp collision energies studied in this thesis.

The fully corrected p_T spectra of primary charged particles is obtained by dividing the differential cross section with the corresponding inelastic cross section (σ_{INEL}):

$$
\frac{\mathrm{d}^2 N^{\mathrm{INEL}}}{\mathrm{d}\eta\mathrm{d}p_\mathrm{T}} = \frac{1}{\sigma_{\mathrm{INEL}}} \frac{\mathrm{d}^2\sigma}{\mathrm{d}\eta\mathrm{d}p_\mathrm{T}}.
\tag{3.10}
$$

ALICE has measured σ_{INEL} for pp collisions at $\sqrt{s} = 2.76\,\mathrm{TeV}$ and $7\,\mathrm{TeV}$ [100], but not for $\sqrt{s} = 5.02\,\mathrm{TeV}$ or $13\,\mathrm{TeV}$. In the last cases, the cross sections are obtained from a fit approximation to the measured values from several experiments, including ALICE, ATLAS, CMS, TOTEM, and others [102]. The values of the inelastic cross sections used are listed below.

- $\sqrt{s} = 2.76\,\mathrm{TeV}$: $\sigma_{\mathrm{INEL}} = 61.8 \pm 0.9$ mb

- $\sqrt{s} = 5.02\,\mathrm{TeV}$: $\sigma_{\mathrm{INEL}} = 67.6 \pm 0.6$ mb

- $\sqrt{s} = 7\,\mathrm{TeV}$: $\sigma_{\mathrm{INEL}} = 70.9 \pm 0.4$ mb

- $\sqrt{s} = 13\,\mathrm{TeV}$: $\sigma_{\mathrm{INEL}} = 77.6 \pm 1.0$ mb

Systematic uncertainties

All sources that contribute to the systematic uncertainties for each collision energy are summarized in Table 3.5, and the p_T dependence uncertainty is shown in Figure 3.21. All contributions are

---

[3] $N_{\mathrm{rec}} = N_{\mathrm{INEL}} \times \varepsilon_{\mathrm{trig}} \times \varepsilon_{Vz}$

considered to be independent among each other and thus they are summed up quadratically to obtain the total systematic uncertainty [86–88], despite of some contributions that can be potentially sensitive to the same origin. The differences between collision energies in the amount of the total systematic uncertainties comes mainly from the improvements made in the reconstruction codes for the data.

Event Cuts

The effect of the event selection, based on the z-coordinate of the primary vertex, is studied by comparing the fully corrected p_T spectra obtained with the nominal selection ($|V_z| < 10$ cm) and those obtained with alternative selections $|V_z| < 5$ cm and $|V_z| < 15$ cm. Identical vertex variations are applied to data and MC simulations. The resulting spectra with vertex variations were compared to the nominal one and the largest difference was taken as the uncertainty bin-by-bin in p_T. The systematic uncertainty for pp collisions at $\sqrt{s} = 2.76$ TeV was found to be flat at 0.9% for the whole p_T range. For $\sqrt{s} = 5.02$ TeV and 13 TeV was below 0.7%, and for 7 TeV data the uncertainty reached 1.2%, only at high p_T ($p_T > 10$ GeV/c).

Source of Uncertainty	Uncertainty [%] for each $\sqrt{s}$			
	2.76 TeV	5.02 TeV	7 TeV	13 TeV
Event selection (Z_v)	0.9	0.5	0.1-1.2	0.3-0.7
Track selection criteria	0.4-3.8	0.6-3.4	1.2-4.0	0.6-5.6
Secondary particles	0.0-3.0	0.0-2.8	0.0-1.6	0.0-0.9
Particle composition	0.1-1.6	0.2-2.7	0.3-1.2	0.3-1.7
Matching efficiency	1.0-4.0	0.0-1.1	0.8-2.6	0.0-3.6
Trigger and vertex biases	0.0-0.4	0.0-1.2	0.5-0	0.0-1.2
p_T - resolution	0.0-0.4	0.0-0.4	0.0-0.4	0.0-0.3
Material budget	0.1-0.9	0.1-0.9	0.1-1.5	0.1-1.5
Normalization	1.9	2.3	3.5	2.0
Total:	**3.8-5.4**	**1.3-4.3**	**2.1-4.7**	**1.6-6.0**

Table 3.5: Contributions to the relative systematic uncertainty for p_T spectra in pp collisions at $\sqrt{s} = 2.76$ TeV, 5.02 TeV, 7 TeV and 13 TeV. The ranges correspond to the minimum-maximum uncertainty in the p_T range of $0.15 - 50$ GeV/c. The total systematic uncertainty is calculated as the sum in quadrature of each contributor.

Secondary particles

The systematic uncertainty due to the secondary particle contamination includes contributions from the template fits to the measured impact parameter distributions. The fit templates were varied using two (primaries, secondaries) or three components (primaries, secondaries from material,
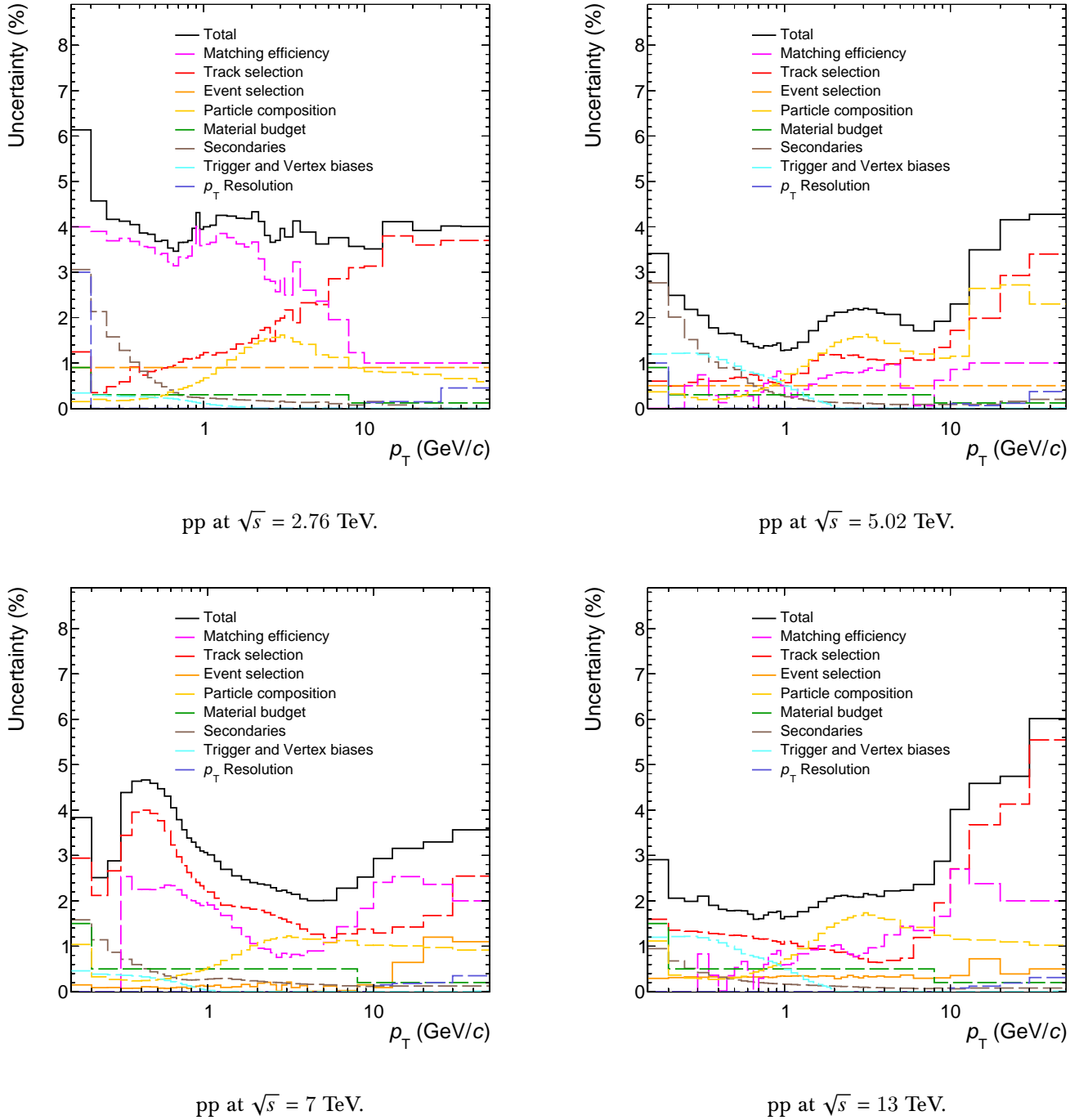
pp at $\sqrt{s}$ = 2.76 TeV.

pp at $\sqrt{s}$ = 5.02 TeV.

pp at $\sqrt{s}$ = 7 TeV.

pp at $\sqrt{s}$ = 13 TeV.

Figure 3.21: Contributions to the systematic uncertainties as a function of p_T for all the pp collision energies studied in this thesis. The total uncertainty (black line) is obtained as the sum in quadrature of all contributions.

secondaries from weak decays of K_s^0 and Λ), as well as variations in the fit ranges. The maximum difference between data and the template fits with 2 components is summed in quadrature with the difference between the results from the 2-and 3-component template fits, and the result is assigned as systematic uncertainty. Figure 3.22 shows the systematic uncertainty for each pp collision energy. The largest uncertainty was found for pp collisions at $\sqrt{s} = 2.76\,\mathrm{TeV}$ with 3% at low p_T and decreases towards high p_T to less than 1% for the remaining energies.
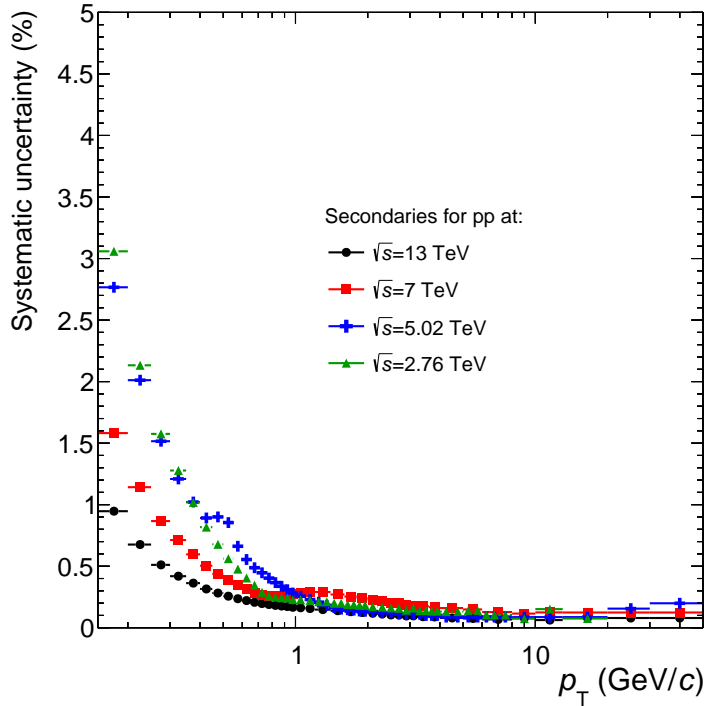

Figure 3.22: Systematic uncertainty for the contamination by secondary particles for pp collisions at $\sqrt{s} = 2.76\,\mathrm{TeV}$, $5.02\,\mathrm{TeV}$, $7\,\mathrm{TeV}$ and $13\,\mathrm{TeV}$.

Track selection criteria

The systematic uncertainty related to the track selection criteria was studied by shifting the nominal values of the track quality selection criteria. The same variations are implemented simultaneously in data as in MC. Each criteria was changed individually at a time, and the resulting change on the corrected spectra was assigned as systematic uncertainty to the respective selection criteria. In Table 3.6 the minimum and maximum track selection criteria variation along with the corresponding systematic uncertainty are listed.

The systematic uncertainty percentage for each track variation as a function of p_T is shown in Figure 3.23 and for each energy collision studied. The total systematic uncertainty due to track selection criteria is calculated as the squared sum of all contributions. It reaches a maximum of 4-5% at high transverse momentum ($p_\mathrm{T} > 10\,\mathrm{GeV}/c$) for pp data at $\sqrt{s} = 2.76\,\mathrm{TeV}$, $5.02\,\mathrm{TeV}$ and $13\,\mathrm{TeV}$. For $\sqrt{s} = 7\,\mathrm{TeV}$, a maximum uncertainty of 4% was found at low momenta ($p_\mathrm{T} < 1\,\mathrm{GeV}/c$).

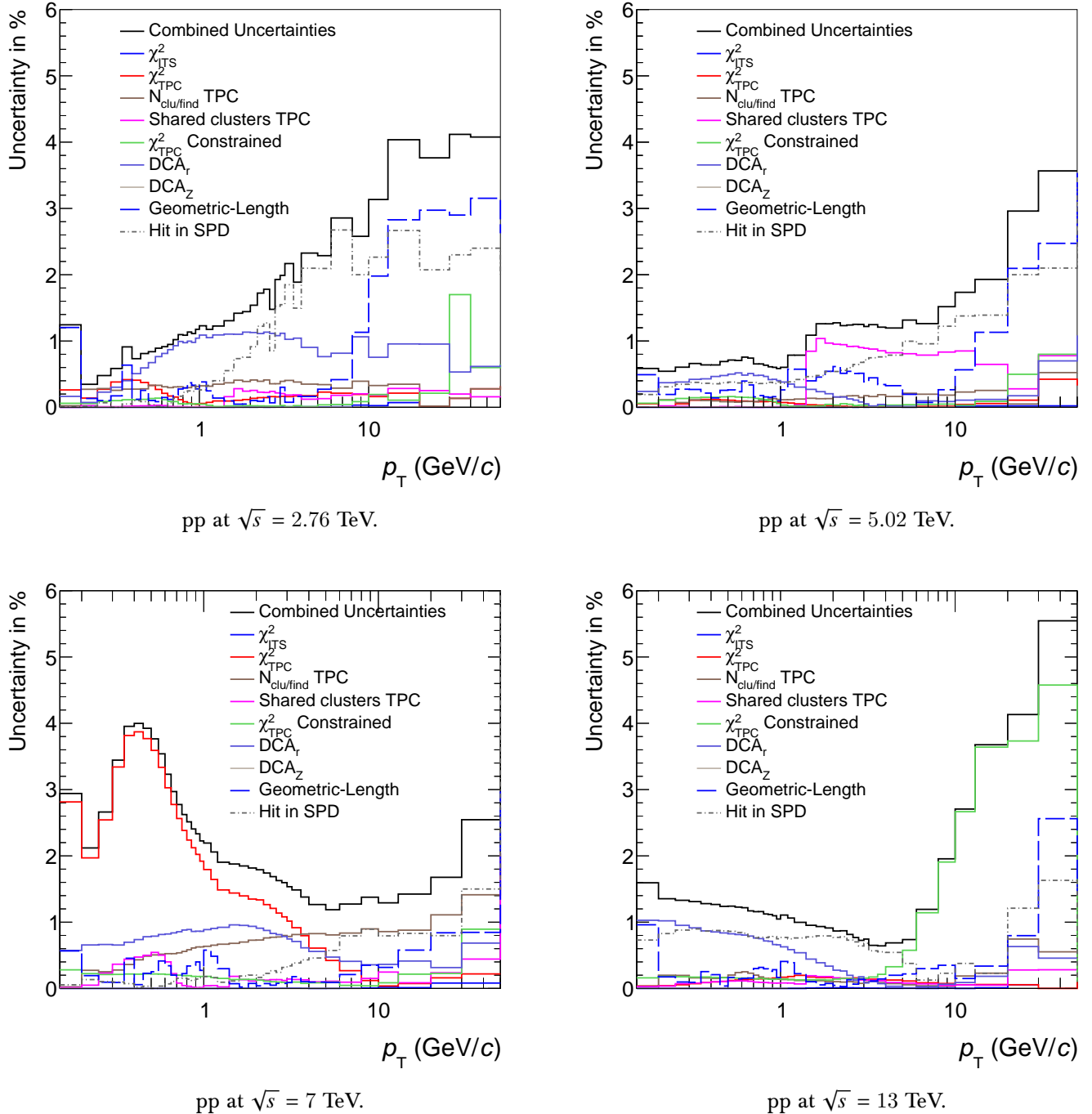Figure 3.23: Systematic uncertainties from the track selection variations for pp collisions in $\sqrt{s} = 2.76\,\text{TeV}$, $5.02\,\text{TeV}$, $7\,\text{TeV}$ and $13\,\text{TeV}$.

Cut	Nominal	Variations	
max. DCAz	2 cm	1 cm	5 cm
max. DCAr	7σ	4σ	10σ
max. ratio of crossed rows over findable clusters	0.8	0.7	0.9
max. fraction of shared TPC clusters	0.4	0.2	1
max. χ^2 per TPC cluster	4	3	5
max. χ^2 per ITS cluster	36	25	49
one hit in the SPD	required	not required	
geometric-length (dead TPC area)	3cm	4cm	2cm
geometric-length (track length)	130	140	120
max. 5-dim. χ^2 TPC constrained track vs. global track	36	25	49

Table 3.6: Nominal values of the track selection criteria and the respective variations used for the systematic uncertainty calculations.

Particle Composition

The systematic uncertainty related to the particle composition correction consists mainly of three effects. The first effect is due to the p_T threshold required when a track is sufficiently long[4]. The identified charged particles have been measured in different low-p_T ranges. Therefore, an extrapolation fit has to be performed to complete the region where data is not measured. To estimate the uncertainty, the extrapolation function as well as the fit p_T region is varied.

The second effect is only relevant for high transverse momentum particles ($p_T > 8 \, \text{GeV}/c$), where the particle species fraction is assumed to be flat. The momenta at which this assumption is considered, is varied and the maximal deviation from the default is assigned as uncertainty. The different configurations for low, high p_T and the ratios to the nominal particle composition correction are shown on the right side of Figure 3.24.

The third effect is when the systematic uncertainty of the measured identified charged particle spectra is propagated to the correction factor. Each data point is transported upwards or downwards by the amount of its corresponding systematic uncertainty, then the correction factor is recalculated using this spectra moved up/down and leaving the other particle spectra unchanged. The total uncertainty for the third effect is calculated as the sum in quadrature of the maximum difference between the correction with the moved spectra and the nominal one. In the upper panel of Figure 3.25, the particle composition correction factors for the nominal case is shown as well as those obtained when the identified spectra are moved down[5]. In the bottom panel, the ratio to the nominal correction is shown, where the total deviation is calculated as the sum in quadrature of the individual ratios.

The total uncertainty and each contributor to the particle composition uncertainty is shown in

---

[4]It is required to have at least 120 crossed TPC rows
[5]The systematic uncertainties of the identified charged particles are symmetric.
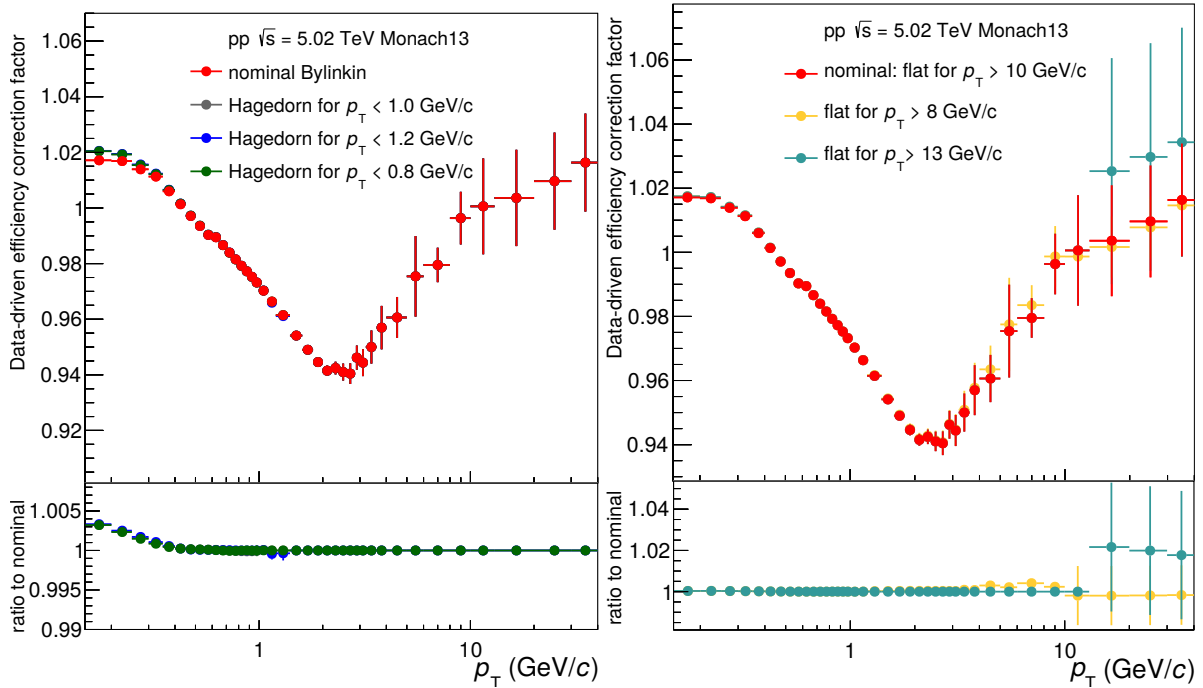
Figure 3.24: **Left**: Systematic uncertainty of the particle composition correction due to the extrapolation to low p_T .**Right**: Similarly, but correction due to the assumption at high p_T .
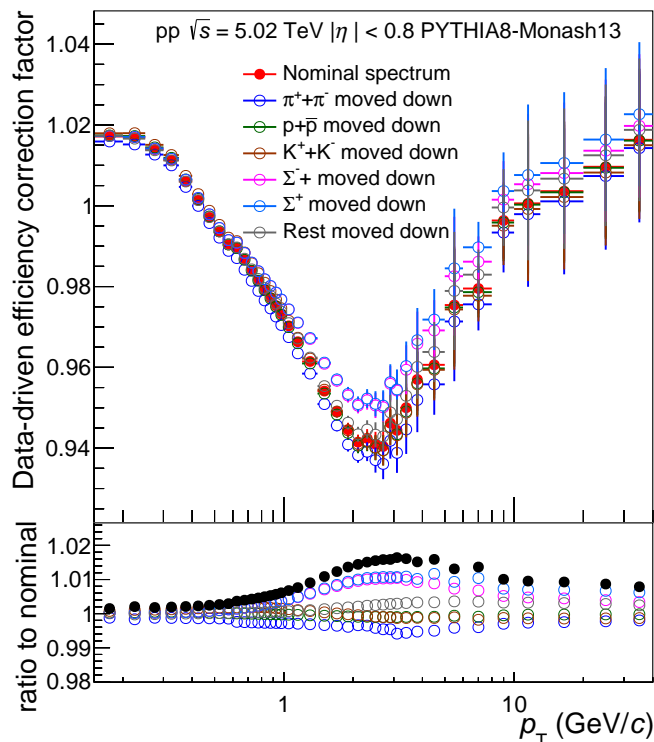

Figure 3.25: Particle composition correction factor when the spectra is moved down. The bottom panel shows the ratio to the unmoved correction factor.

Figure 3.26 for pp collisions at $\sqrt{s}$ = 5.02 TeV, the same procedure was used for all collision energies giving similar values of systematic uncertainties (see Figure 3.21) [97].
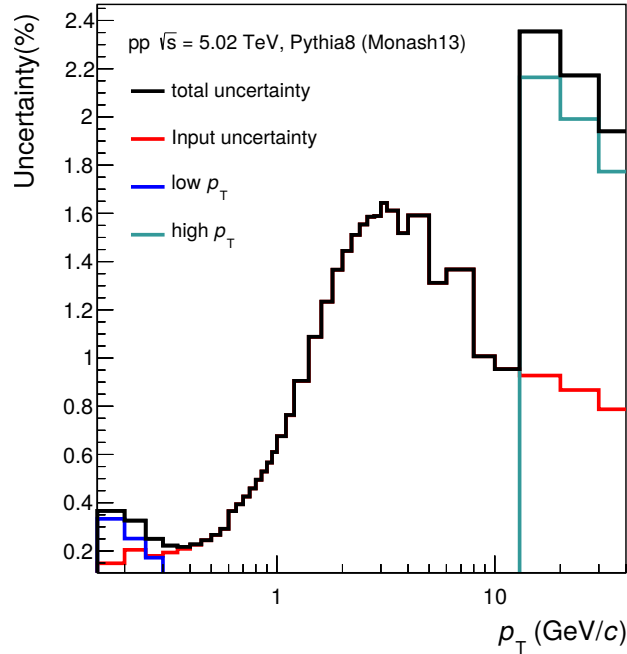
Figure 3.26: Contributors to particle composition systematic uncertainty for pp collisions at $\sqrt{s} = 5.02\,\mathrm{TeV}$.

Matching efficiency

The correction for tracking efficiency is obtained from Monte Carlo simulations (see Section 7.1) and since they do not have a perfect description of the ALICE detector, an additional systematic uncertainty has to be obtained.

The systematic uncertainty is calculated based on the differences between data and MC that a track measured in the TPC has probability to be matched in the ITS . The matching efficiency is calculated by the ratio of tracks that fulfilled the TPC selection criteria and tracks with TPC and ITS selection selection criteria. Table 3.7 lists in detail all the selection criteria used in each case, including a less restrictive selection of primary tracks in terms of their DCA_{xy} and DCA_z.

The matching efficiency for primary and secondary particles is expected to be considerably different, since the secondary particles can originate after the last layers of the SPD and, as a consequence can not have a match in the ITS. The right plot of Figure 3.27 shows the matching efficiency for primary, secondary and reconstructed particles from PYTHIA 8 (Monash) MC simulation at $\sqrt{s} = 5.02\,\mathrm{TeV}$. The secondary particles have a matching efficiency of around 70% at $p_\mathrm{T} \approx 0.5\,\mathrm{GeV}/c$ with a strong steeply falling p_T -dependence. For primary particles, the matching efficiency is close to 95% over the entire p_T range studied. In addition, the primaries were corrected for the missing secondary particles by the DCA_{xy} fits to data, as studied in Section 7.3, giving a slightly reduced matching efficiency.

The matching efficiency obtained with reconstructed tracks from MC is generally larger than data. However, after correcting by the missing secondaries, the efficiency becomes closer to data. The resulting discrepancy reflects the inaccuracy of the MC simulations. The maximum difference is assigned as a systematic uncertainty and is shown in Figure 3.28, where it was found to be lower than 1% over the entire p_T range for pp data at $\sqrt{s} = 5.02\,\mathrm{TeV}$, within the statistical fluctuations

Cut	TPC	TPC-ITS
TPC refit	required	required
Track length		
Ratio of crossed rows over findable clusters in the TPC	0.8	0.8
χ^2 per TPC cluster	≤ 4	≤ 4
Fraction of shared TPC clusters	≤ 0.4	≤ 0.4
DCA to primary vertex in z	≤ 3.2 cm	≤ 3.2 cm
DCA to primary vertex in xy	≤ 2.4 cm	≤ 2.4 cm
ITS refit	not required	required
number of hits in SPD	≥ 0	≥ 1

Table 3.7: Track selection criteria used for the calculation of the matching efficiency for the cases of TPC only and TPC-ITS tracks.
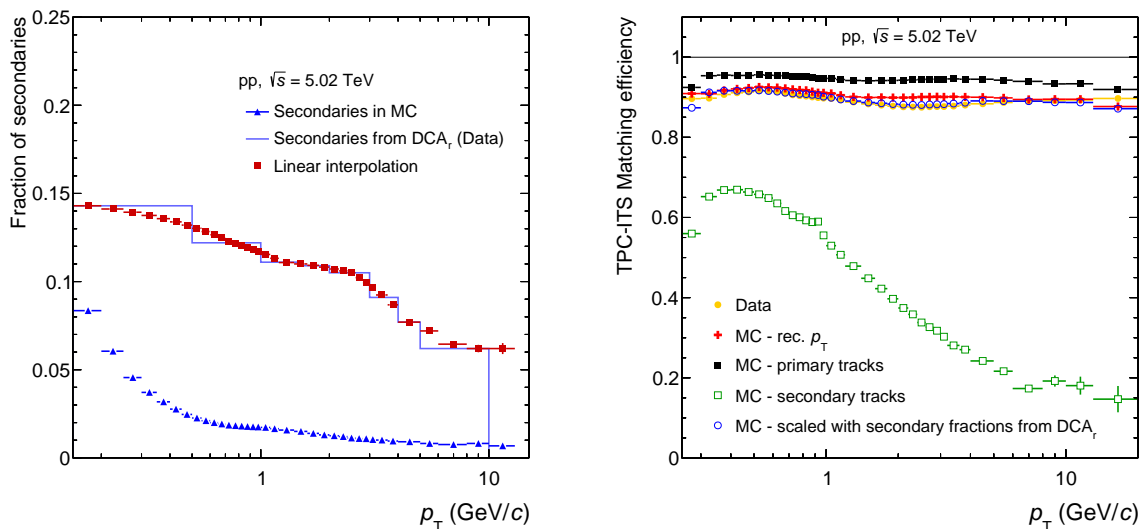
(limited to the data and MC sample).

Figure 3.27: **Left**: Secondaries fraction obtained from MC simulations and from fits to the DCA_{xy} distributions in data. A linear interpolation is performed for data in order to have the same p_T range as the matching efficiency. **Right**: Matching efficiency for data, MC primary, MC secondary and MC reconstructed particles. The MC matching efficiency scaled by the fraction of secondary particles (DCA_{xy} fits) is shown as empty blue markers.

Detector material budget

The amount of material present between the primary vertex and the detectors, as well as the detectors themselves can influence the final measurement of charged particles transverse momentum. The material budget can affect the energy loss of charged particles and hadronic interactions, as well as an increased production of secondary electrons (coming from photon conversions), other
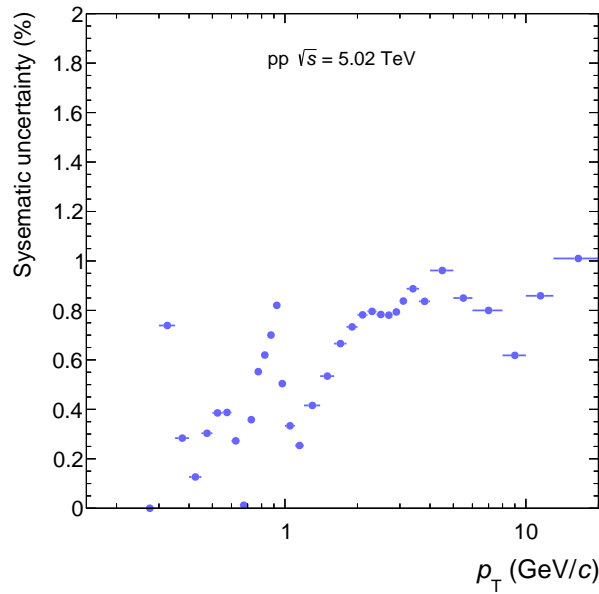
Figure 3.28: Amount of systematic uncertainty from the TPC-ITS matching efficiency.

secondary particles and multiple scattering of charged particles at low p_T.

ALICE has measured the radiation thickness with a precision of 6.5% using reconstructed photon conversions [103] in pp collisions at $\sqrt{s} = 7$ TeV. The systematic uncertainty was estimated by varying the material budget by $\pm 4.5\%$ in the GEANT simulations. The estimated uncertainty is p_T-dependent, going from 0.9% at very low p_T to lower than 0.1% at intermediate and high p_T.

The same systematic uncertainty was used for all collision energies based on the assumption that the ALICE material budget remained unchanged.

Trigger and Vertex

The trigger and vertex bias systematic uncertainty is associated with the multiplicity dependence of the trigger and vertex efficiencies as shown in Figure 3.2. In particular, the low multiplicity pp events which are characterized by a softer p_T distribution can have an impact at low p_T.

Figure 3.29 (left) shows the trigger and vertex biases for PYTHIA 8 Monash and PYTHIA 6 Perugia2011 for pp collisions at $\sqrt{s} = 5.02$ TeV. The biases are calculated from the comparison of the p_T distributions with and without the trigger or vertex selection. While the vertex selection bias is small, the bias from the trigger selection was found to have a larger deviation. This is expected since the data was recorded with the $V0_{AND}$ trigger condition, which is insensitive to single diffractive (SD) events but results are obtained for INEL events that include diffraction. The systematic uncertainty assigned due to this effect is half of the maximum deviation between the trigger or vertex bias, while the other half is used as a correction to the transverse momentum distribution. The right plot of Figure 3.29 shows the systematic uncertainty for each collision energy. The uncertainty distribution exhibits a decreasing trend with a maximum value of 1.2% at low p_T for pp collisions at $\sqrt{s} = 5.02$ TeV, reaching zero for tracks with $p_T > 2$ GeV/c at all energies.
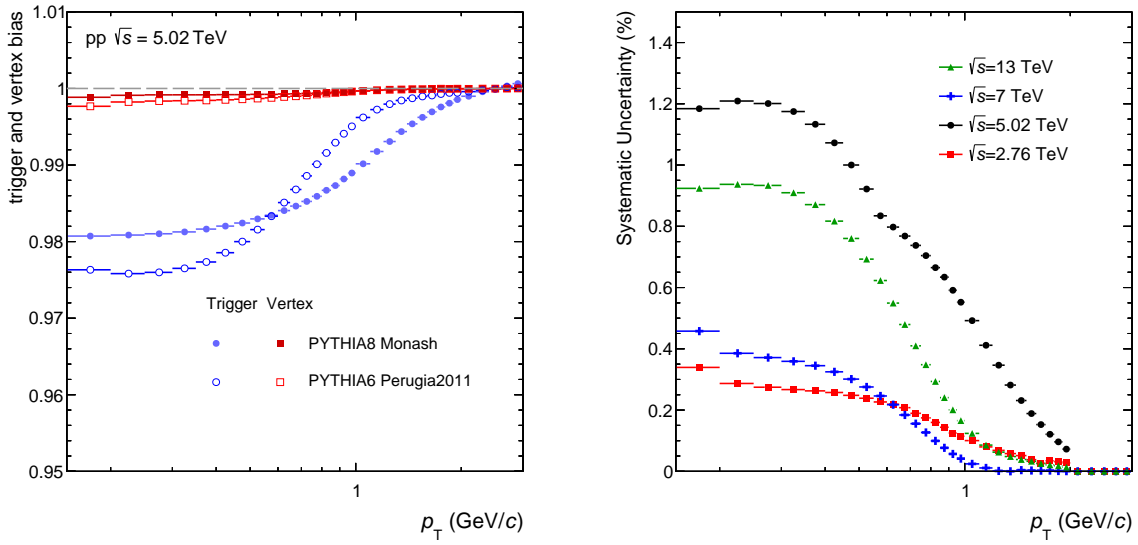
Figure 3.29: **Left**: Trigger and vertex bias for two PYTHIA8 Monash and PYTHIA6 Perugia2011 for pp collisions at $\sqrt{s}$ = 5.02 TeV. **Right**: Systematic uncertainty for trigger and vertex bias for all pp collision energies studied.

p_T **Resolution**

The systematic uncertainty on the momentum resolution was estimated from the $1/p_T$ shift of positively and negatively charged particles ($\Delta(1/p_T)$), as explained in Section 7.4. The RMS (ϕ smearing) is included in the systematic uncertainty calculation. The difference between the corrected p_T spectra with and without the smearing applied is used to estimate the maximum uncertainty for this contribution.

In the p_T resolution correction procedure (see Section 7.4), a power law parametrization to the corrected transverse momentum spectrum is used. An additional contributor to the systematic uncertainty is obtained from the variation of the power law fit range. The resolution correction is calculated with a power law fit in the p_T ranges: $8\,\mathrm{GeV}/c$ to $50\,\mathrm{GeV}/c$ and $12\,\mathrm{GeV}/c$ to $50\,\mathrm{GeV}/c$, and compared to the one using the nominal range ($10\,\mathrm{GeV}/c$ to $50\,\mathrm{GeV}/c$). The maximum difference is assigned as systematic uncertainty. On the left side of Figure 3.30, the ϕ smearing and the fit range uncertainty is shown. On the right side, the total p_T resolution uncertainty for each collision energy is shown. The total uncertainty, calculated as the squared sum of each contributor, was found to have an increasing trend with p_T and a maximum value of 0.45% for p_T = $50\,\mathrm{GeV}/c$.
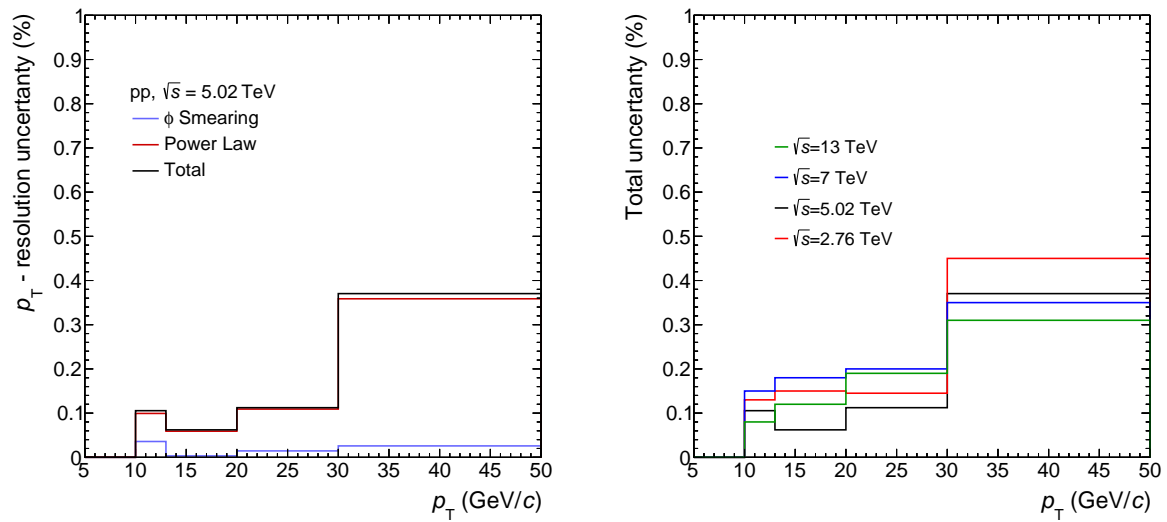
Figure 3.30: **Left**: p_T-resolution systematic uncertainty contributors for pp collisions at $\sqrt{s} = 5.02\,\text{TeV}$. **Right**: Total p_T-resolution systematic uncertainty for pp collisions at $\sqrt{s} = 2.76\,\text{TeV}$, $5.02\,\text{TeV}$, $7\,\text{TeV}$ and $13\,\text{TeV}$.

Chapter 4

Results and Discussion

In this chapter, results on the differential cross section for charged particles in pp collisions are presented. The transverse momentum spectra are compared to event generators like PYTHIA and EPOS LHC, as well as with other previously published results. The details on the construction of the pp reference at $\sqrt{s}$ = 5.44 TeV is explained in Section 2.

In Section 3, the average transverse momentum for charged particles is calculated as a function of center-of-mass energy and compared to previous measurements at similar or lower energies. The transverse momentum spectra are studied in multiplicity ranges and compared to the Minimum Bias measurement. The $\langle N_{\mathrm{ch}} \rangle$ vs $\sqrt{s}$, calculated from the integration of the pp yield, is presented as well.

In the last part of this chapter, the differential cross section measured in pp collisions is compared to the Pb-Pb and Xe-Xe yield. The nuclear modification factor is calculated based on the particle production in pp and heavy-ion collisions, and is presented in this thesis as a function of centrality and average multiplicity $\langle \mathrm{d}N_{\mathrm{ch}}/\mathrm{d}\eta \rangle$.

Differential cross section in pp collisions

The differential cross sections have been measured for inelastic (INEL) pp collisions in ALICE at $\sqrt{s}$ = 2.76 TeV, 5.02 TeV, 7 TeV and 13 TeV in the pseudorapidity range of $|\eta|$ < 0.8 and in a transverse momentum range of $0.15\,\mathrm{GeV}/c$ < p_{T} < $50\,\mathrm{GeV}/c$. Some of the results presented in this thesis are published in [104, 105], and used as a reference to compare with the production yield in Xe-Xe and Pb-Pb collisions to obtain the nuclear modification factor R_{AA}.

The upper panel of Figure 4.1 shows the measured differential cross section for pp collisions at $\sqrt{s}$ = 2.76 TeV data, and the bottom panel shows the ratio to the published results [106, 107]. A good agreement was found within the systematic uncertainties, especially at low and high-p_{T} . The largest discrepancy was found at intermediate-p_{T} of around 8%, where a characteristic peak structure is present. This peak is originated from the updated particle composition correction, which was not as complete for the publication as the one presented in Section 7.2. The p_{T} -differential cross section

from the reanalysis of the $\sqrt{s} = 2.76$ TeV data has improved in precision compared to the previously published results, with reduced systematic uncertainties up to 30%.
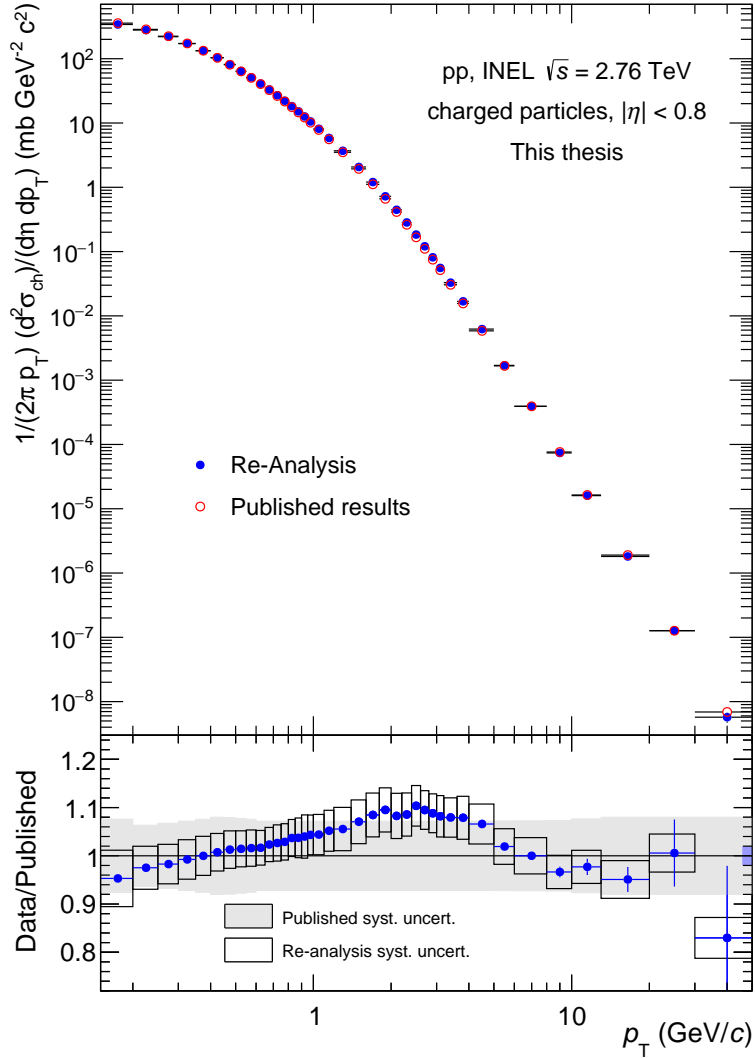

Figure 4.1: **Upper panel**: Differential cross section measured in pp collisions at $\sqrt{s} = 2.76$ TeV for the reanalysis of the data (filled circles) and the published results [106] (empty circles). **Bottom panel**: Ratio of the reanalysis to the published results. The gray band and the boxes represent the systematic uncertainties of the publication and the reanalysis, respectively. The vertical lines represent the statistical errors.

Figure 4.2 shows the comparison of the differential cross sections and the published results at $\sqrt{s} = 5.02$ TeV [106, 107]. In the publication, the p_T-differential cross section was constructed using three different methods at three different p_T-ranges: a) At low-p_T ($< 5\,\mathrm{GeV}/c$), a power law interpolation between the measured cross sections for pp collisions of $\sqrt{s} = 2.76$ TeV and 7 TeV was used. b) At $5\,\mathrm{GeV}/c < p_T < 20\,\mathrm{GeV}/c$, the measurement at $\sqrt{s} = 7$ TeV is scaled down using NLO-pQCD calculations. c) And at $p_T > 20\,\mathrm{GeV}/c$, a power law parametrization of the NLO-scaled reference is used.

The largest difference between the measurement and the constructed reference at $\sqrt{s} = 5.02$ TeV is

of the order of 10%, as shown in the lower panel of Figure 4.2. This difference is explained by the new data-driven tracking efficiency (particle composition) and the set of track selection criteria used. At low-p_T ($< 1\,\text{GeV}/c$) and at high-p_T ($> 10\,\text{GeV}/c$), the agreement is better than 4% and well covered by the systematic uncertainties. A remarkable precision has been achieved in the measurement of the p_T-differential cross section (syst. unc. of 1.3% to 4.3%), with a reduction of less than a factor four in the systematic uncertainties when compared to the old reference.

For the reanalysis of the pp data at $\sqrt{s} = 7$ TeV, shown in Figure 4.3, the agreement with the published cross section is within 8% for $p_T > 1.5\,\text{GeV}/c$. At $p_T < 1\,\text{GeV}/c$, the ratio is close to unity. The systematic uncertainties of the reanalysis of the data are between 30-60% smaller than the published uncertainties.
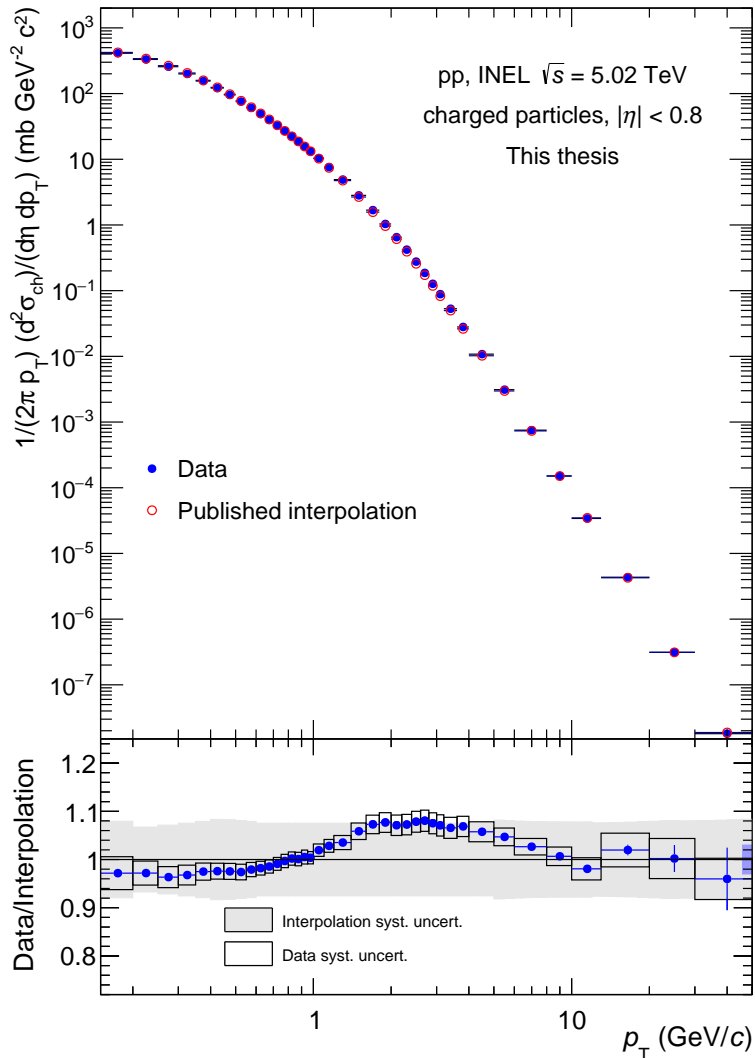

Figure 4.2: **Upper panel**: Differential cross section measured in pp collisions at $\sqrt{s} = 5.02$ TeV for the analysis of the data (filled circles) and the published interpolation results [106] (empty circles). **Bottom panel**: Ratio of the reanalysis to the published results. The gray band and the boxes represent the systematic uncertainties of the publication and the reanalysis, respectively. The vertical lines represent the statistical errors.
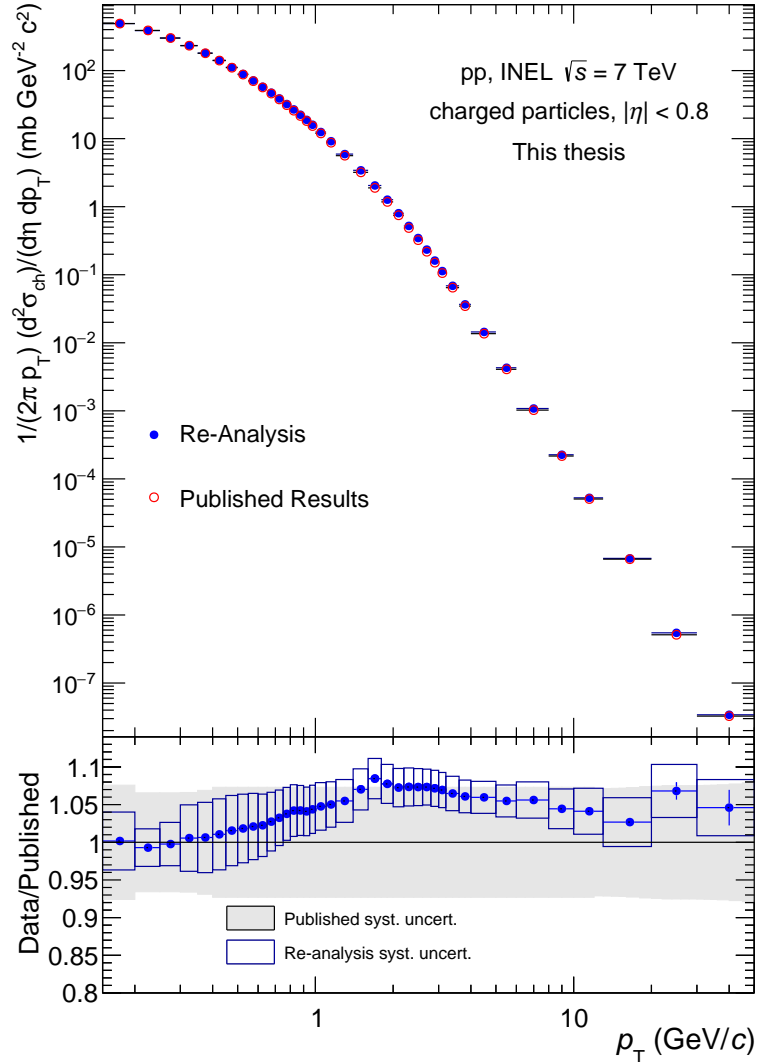
Figure 4.3: **Upper panel**: Differential cross section measured in pp collisions at $\sqrt{s}$ = 7 TeV for the reanalysis of the data and the published results [106,107]. **Bottom panel**: Ratio of the reanalysis to the published results. The gray band and the boxes represent the systematic uncertainties of the publication and the reanalysis, respectively. The vertical lines represent the statistical errors.

The p_T-differential cross section has not been measured for INEL pp collisions at $\sqrt{s}$ = 13 TeV, but only the transverse momentum spectrum for INEL>0 event class[1] is published [108] in the p_T region of $0.15\,\text{GeV}/c - 20\,\text{GeV}/c$. Therefore, the published result was scaled by the ratio of INEL to INEL> 0 event classes in order to compare with the result obtained in this thesis. The scaling factor was found to be 0.82 for $|\eta| < 0.8$ and was calculated from the ratio of the average pseudorapidity densities of charged particles as a function of η in both event classes [108]. Figure 4.4 shows the measured p_T-differential cross section compared to the scaled published result in the transverse momentum region of $0.15\,\text{GeV}/c < p_T < 20\,\text{GeV}/c$. In the bottom panel, the ratio of the measurement to the published result is shown. The agreement of both results is within the systematic uncertainties, where the maximum deviation is around 9% at $p_T \approx 3\,\text{GeV}/c$. Similarly

---

[1]Events with at least one charged particle produced with $p_T > 0.15\,\text{GeV}/c$ in the acceptance of $|\eta| < 1.0$

to the previous collision energies, the systematic uncertainties from the INEL measurement are reduced by approximately a factor 2 in the p_T-range studied.
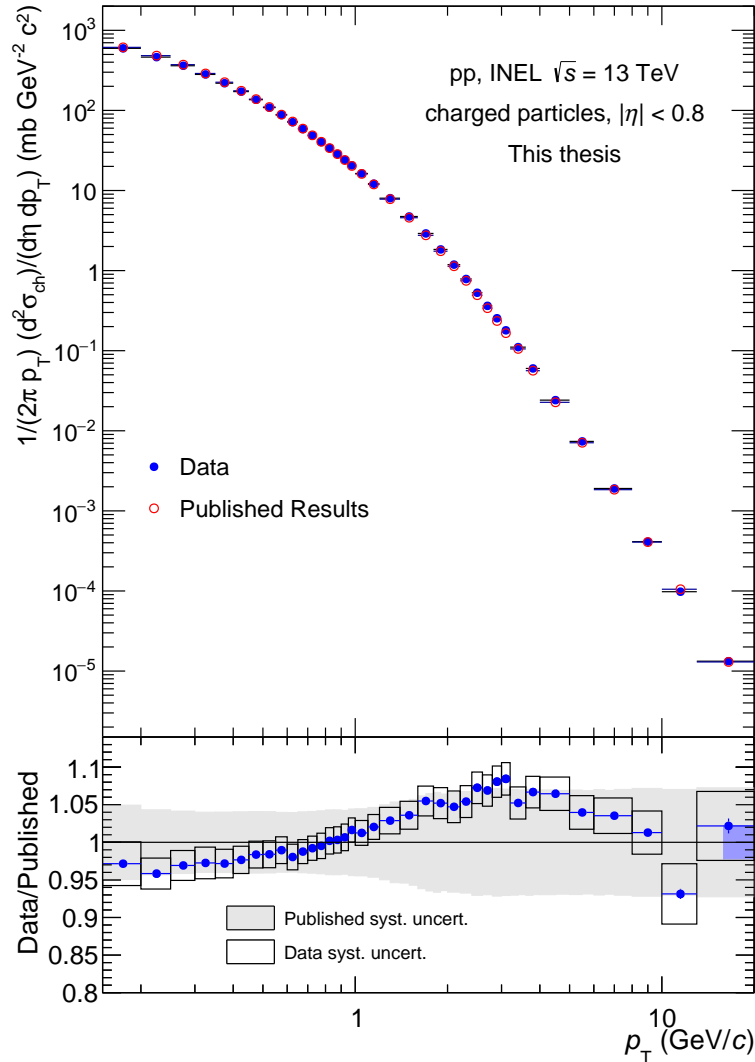

Figure 4.4: **Upper panel**: Differential cross section measured in pp collisions at $\sqrt{s} = 13$ TeV for the analysis of the data and the constructed cross section from the published results for $INEL > 0$ [108]. **Bottom panel**: Ratio of the analysis to the published results. The gray band and the boxes represent the systematic uncertainties of the publication and the reanalysis, respectively. The vertical lines represent the statistical errors.

A similar structure at intermediate p_T is present for the results at $\sqrt{s} = 5.02$ TeV, 7 TeV and 13 TeV as the one discussed for $\sqrt{s} = 2.76$ TeV, but less pronounced for the cases of $\sqrt{s} = 7$ TeV and 13 TeV. The different magnitude of the peak structure between collision energies can be attributed to the MC versions used for the calculation of the tracking efficiency and the particle composition correction, PYTHIA 6 Perugia2011 and PYTHIA 8 Monash tune.

Figure 4.5 and 4.6 compares the measured p_T spectra with results from PYTHIA 8 Monash tune and EPOS LHC. None of the MC generators is able to reproduce the data within the uncertainties

of the measurement in the full p_T -range. The discrepancies are dependent on the collision energy.

The upper panel of Figure 4.5 corresponds to pp collisions at $\sqrt{s}$ = 2.76 TeV, while the lower panel is at $\sqrt{s}$ = 5.02 TeV. PYTHIA 8 (Monash tune) and EPOS LHC fail to reproduce the spectral shape of the data at $\sqrt{s}$ = 2.76 TeV, with a maximum discrepancy between 20-25% and fluctuates over the entire p_T range. In the lower pannel, PYTHIA agrees better with the spectral shape than EPOS LHC, especially at $1\,\mathrm{GeV}/c\ < p_T\ < 10\,\mathrm{GeV}/c$. The data-MC differences are of around 4% and 14% for PYTHIA and EPOS, respectively. At high-p_T, both MC models describe the $\sqrt{s}$ = 5.02 TeV data within 10%.

At $p_T\ > 1\,\mathrm{GeV}/c$, EPOS LHC describes the measured pp spectrum at $\sqrt{s}$ = 7 TeV and 13 TeV within 10%, as shown in Figure 4.6. On the other hand, PYTHIA overestimates the measurement by approximately 20% for $\sqrt{s}$ = 13 TeV data, possibly because the parameters have been tuned to 7 TeV data. The upper panel shows the ratio to $\sqrt{s}$ = 7 TeV data, where PYTHIA agrees well within systematic uncertainties as expected. At $p_T\ < 1\,\mathrm{GeV}/c$, EPOS and PYTHIA overestimate the data by approximately 20% and 25% similarly for all collision energies.

As explained in Section 6, diffractive events produce few particles at mid-rapidity ($|\eta| < 0.8$) and therefore, the overall p_T spectrum is largely dominated by particles from non-diffractive events, around 72%. At $p_T\ < 1\,\mathrm{GeV}/c$, a third of the total amount of tracks from inelastic processes come from diffractive processes. Hence, the imprecision of PYTHIA to describe the spectral shape in data at low-p_T ($p_T\ < 1\,\mathrm{GeV}/c$) can partially be attributed to the complications of the pQCD-inspired event generators to describe diffraction processes [35,100]. The EPOS LHC troubles to describe the measurement is possibly attributed to the non complete 3-D hydro calculation and the treatment of the hadronic cascade, as explained in Section 9.
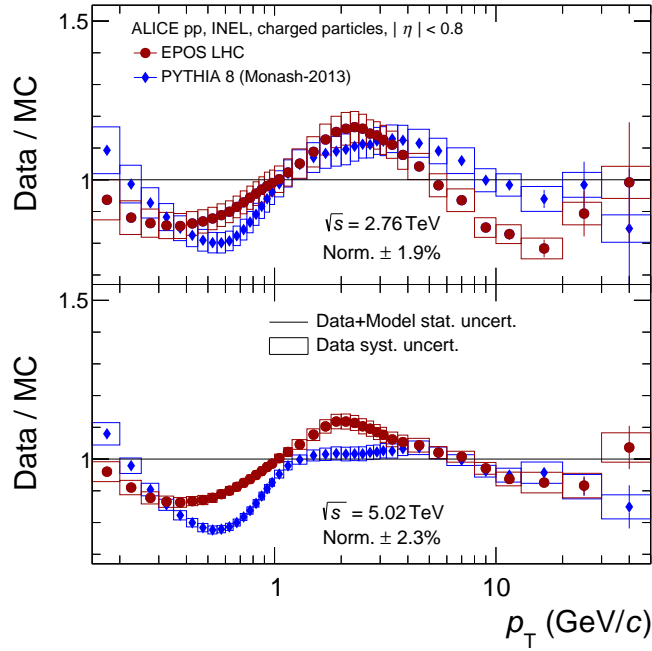
Figure 4.5: Comparison of the charged-particle transverse momentum spectra measured in pp collisions to PYTHIA 8 (Monash-2013 tune) and EPOS-LHC model calculation at $\sqrt{s}$ = 2.76 TeV (top) and $\sqrt{s}$ = 5.02 TeV (bottom). The boxes represent the systematic uncertainties of the data and the vertical lines are the statistical errors of the data and model added in quadrature. Result published in [104].
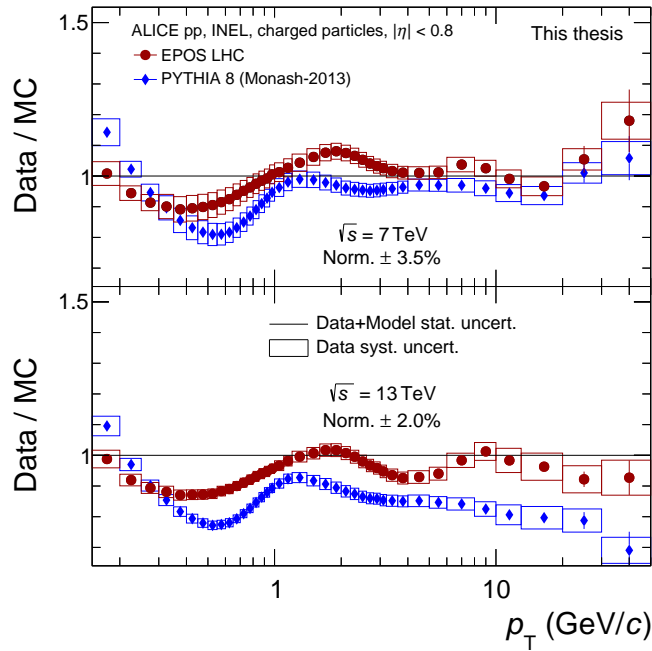

Figure 4.6: Comparison of the charged-particle transverse momentum spectra measured in pp collisions to PYTHIA 8 (Monash-2013 tune) and EPOS-LHC model calculation at $\sqrt{s}$ = 7 TeV (top) and $\sqrt{s}$ = 13 TeV (bottom). The boxes represent the systematic uncertainties of the data and the vertical lines are the statistical errors of the data and model added in quadrature.

The ratios of transverse momentum spectra for charged particles at different collision energies and the corresponding MC simulations are shown in Figure 4.7. The left panel shows the ratio $\sqrt{s} = 5.02$ TeV to 2.76 TeV, and the right panel the ratio of yields at $\sqrt{s} = 13$ TeV to 7 TeV. In both cases, the spectrum is significantly harder at $\sqrt{s} = 13$ TeV and 5.02 TeV when compared to 7 TeV and 2.76 TeV, respectively. In the lower collision energy case, the ratio is between 2.5 and 3 at $p_{\mathrm{T}} > 10\,\mathrm{GeV}/c$, while in the larger collisional energy flattens at a value of 2. It is important to note that the last point in the $5.02\,\mathrm{TeV}/2.76$ TeV ratio has 20% statistical error and no conclusion on a possible flattening can be driven.

EPOS LHC and PYTHIA 8 manage to reproduce the hardening trend observed in data over the entire p_{T}-range studied. In the ratio $\sqrt{s} = 5.02$ TeV to 2.76 TeV, PYTHIA agrees with data within the systematic uncertainties and reflects better the hardening trend than EPOS, where at $4 < p_{\mathrm{T}} < 30\,\mathrm{GeV}/c$ it underestimates data. In the ratio $\sqrt{s} = 13$ TeV to 7 TeV, PYTHIA slightly underestimates data at $p_{\mathrm{T}} < 2\,\mathrm{GeV}/c$, and similarly for EPOS in the range $p_{\mathrm{T}} < 20\,\mathrm{GeV}/c$.

At low-p_{T}, the differences between data and the MC event generators do not reflect the observed 20% discrepancy as in Figures 4.5 and 4.6. The good agreement of MCs with the data ratios can be seen as the inaccuracies cancel out in the ratio of the pp yield at two different energies.
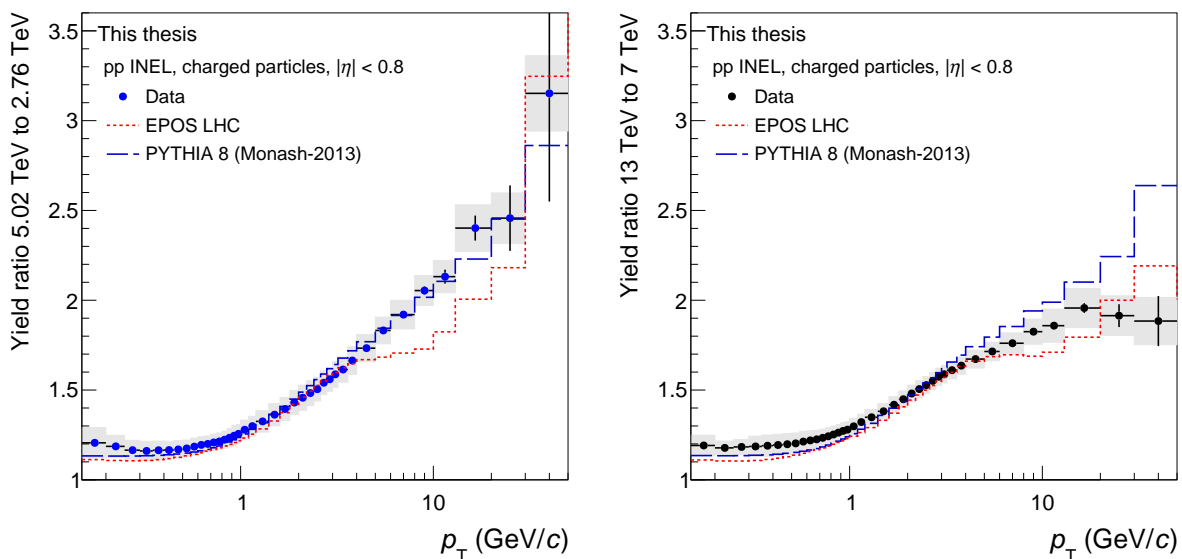

Figure 4.7: **Left**: Ratio of charged-particle transverse momentum spectra for INEL pp collisions at $\sqrt{s} = 5.02$ TeV to $\sqrt{s} = 2.76$ TeV. The gray boxes represent the systematic uncertainties and the vertical lines the statistical. Comparison to PYTHIA 8 (Monash-2013 tune) and EPOS LHC is represented with the blue and red dashed lines, respectively. **Right**: Similar ratio for pp collisions at $\sqrt{s} = 13$ TeV to 7 TeV.

pp reference at $\sqrt{s}$ =5.44 TeV

ALICE recorded Xe-Xe collisions at $\sqrt{s_{\mathrm{NN}}} = 5.44$ TeV, but no data of pp collisions is available at the same energy. Therefore, a constructed pp reference spectrum is required to obtain the nuclear modification factor. This procedure is based on pp data measured at $\sqrt{s} = 5.02\,\mathrm{TeV}$ and $7\,\mathrm{TeV}$. Two different methods are implemented:

- Scaling up the pp spectrum at $\sqrt{s} = 5.02\,\mathrm{TeV}$ by using the PYTHIA 8 Monash event generator.

- Interpolating between the pp data at $\sqrt{s} = 5.02$ TeV and $\sqrt{s} = 7$ TeV, assuming a power law behavior as function of $\sqrt{s}$.

The power law interpolation was used as default method and the one based on MC simulations was used as a cross check. The maximum difference between both methods is assigned as an extra systematic uncertainty to the constructed pp reference.

The first method uses a PYTHIA fast simulation (without detectors information) of 400 million generated events at $\sqrt{s} = 5.02$ TeV and $\sqrt{s} = 5.44$ TeV. The ratio of the transverse momentum spectra at these two energies is used to scale the measured $\sqrt{s} = 5.02$ TeV pp cross section as follows:

$$\left(\frac{\mathrm{d}^2 N_{\mathrm{ch}}}{\mathrm{d}\eta\mathrm{d}p_{\mathrm{T}}}\right)_{\sqrt{s}=5.44\mathrm{TeV}} = \underbrace{\left(\frac{\mathrm{d}^2 N_{\mathrm{ch}}}{\mathrm{d}\eta\mathrm{d}p_{\mathrm{T}}}\right)_{\sqrt{s}=5.02\mathrm{TeV}}}_{\text{measurement}} \cdot \underbrace{\frac{\left(\frac{\mathrm{d}^2 N_{\mathrm{ch}}}{\mathrm{d}\eta\mathrm{d}p_{\mathrm{T}}}\right)_{\mathrm{MC},\sqrt{s}=5.44\mathrm{TeV}}}{\left(\frac{\mathrm{d}^2 N_{\mathrm{ch}}}{\mathrm{d}\eta\mathrm{d}p_{\mathrm{T}}}\right)_{\mathrm{MC},\sqrt{s}=5.02\mathrm{TeV}}}}_{\text{ratio from PYTHIA simulation}} \tag{4.1}$$

Note that this approach does not require the simulation to describe the absolute spectra at different energies, but only the relative changes over a moderate energy increase. The transverse momentum spectra from PYTHIA8 (Monash) for the two energies is shown in Figure 4.8. The spectrum at higher collision energy was found to be harder and the difference goes from 2% to 10% from low to high-p_{T}, respectively. The lower panel shows the p_{T}-dependent scaling factor applied to the measured cross section in pp collisions at $\sqrt{s} = 5.02$ TeV.
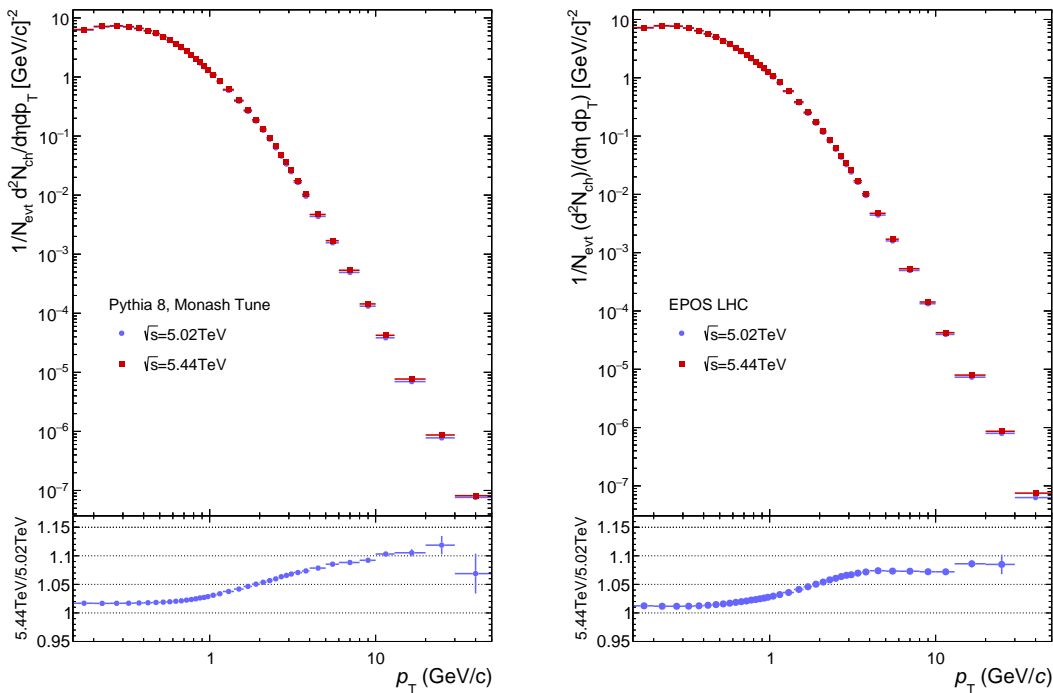

Figure 4.8: Top: Generated pp spectrum with the PYTHIA8 Monash (left) and EPOS LHC (right) at different energies. Bottom: ratio of the two energies, applied as scaling to the measured $\sqrt{s} = 5.02$ TeV spectrum.

The interpolation method has been successfully used to interpolate the pp reference in previous ALICE publications [106]. It is based on the observation that the cross section at a fixed p_T scale is approximated to a power law in the collision energy, i.e. $d\sigma/dp_T(\sqrt{s}) \propto \sqrt{s}^n$. This scaling behavior only applies to the cross section, not the per-event yield. The measured cross sections in pp collisions at $\sqrt{s} = 5.02$ TeV and $\sqrt{s} = 7$ TeV is used to obtain a bin-by-bin interpolation to $\sqrt{s} = 5.44$ TeV. Figure 4.9 shows two examples at different p_T of the power law interpolation of measured cross sections as a function of $\sqrt{s}$. Figure 4.10 shows the ratio of the constructed pp reference to the measured cross section in $\sqrt{s} = 5.02$ TeV, as well as the ratio as obtained from PYTHIA 8 (Monash).

Figure 4.11 shows the interpolated pp reference at $\sqrt{s} = 5.44$ TeV compared to EPOS LHC and PYTHIA 8 (Monash). At low-p_T ($< 1\,\text{GeV}/c$), both event generators overestimate the spectra by around 20%. For $p_T > 1.0\,\text{GeV}/c$, PYTHIA agrees with the reference within the systematic uncertainties, while EPOS has a difference within 10%.
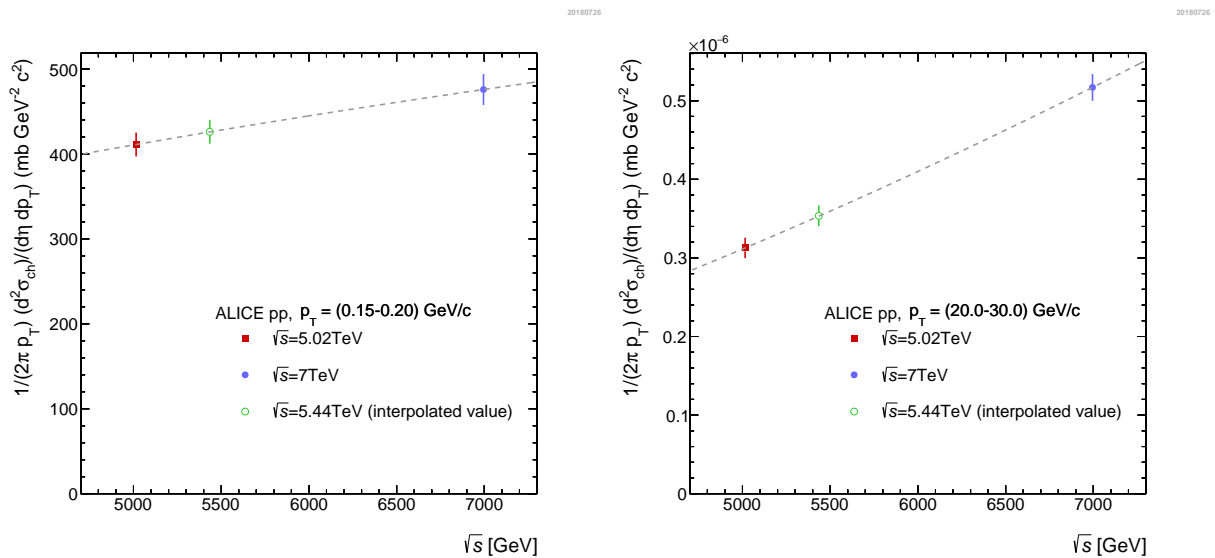

Figure 4.9: Differential cross section as a function of pp collisional energy ($\sqrt{s}$) at low-p_T (left) and at high-p_T (right). The results at $\sqrt{s} = 5.02$ TeV and 7 TeV are used to interpolate the value at $\sqrt{s} = 5.44$ TeV.
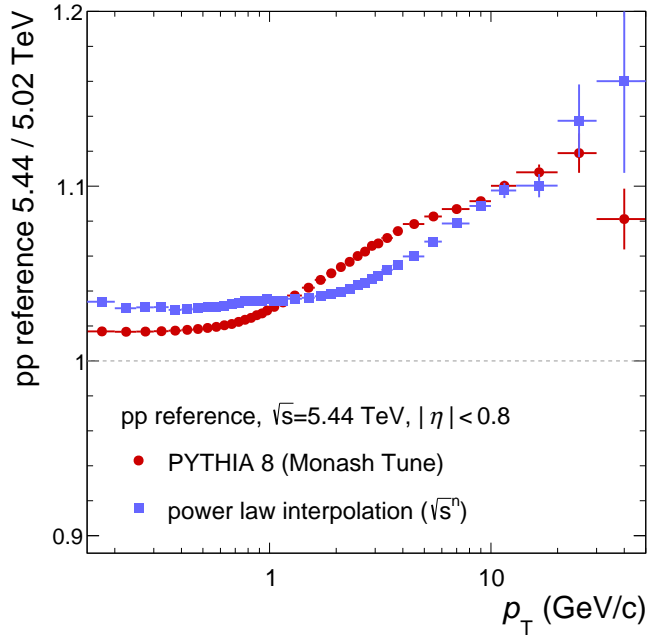
Figure 4.10: Ratio of p_T-differential cross sections in pp collisions at $\sqrt{s}$ = 5.44 TeV to 5.02 TeV, from the power law interpolation method and the event generator PYTHIA 8. Figure published in [105].

Average transverse momentum $\langle p_T \rangle$

In order to determine the average transverse momentum $\langle p_T \rangle$ for INEL pp collisions for each collision energy studied, a modified Hagedorn function [109] is used to fit the transverse momentum spectrum and to extrapolate down to $p_T = 0 \, \mathrm{GeV}/c$. The function is as follows:

$$\frac{dN_{ch}^2}{d\eta \, dp_T} = A \frac{p_T{}^2}{\sqrt{m_\pi^2 + p_T{}^2}} \left(\frac{1 + p_T}{C} \right)^{-B} \tag{4.2}$$

where A,B, and C are free parameters and m_π is the mass of the charged pion. At small p_T, the second part of equation $\left(\frac{1+p_T}{C} \right)^{-B}$ behaves like an exponential in p_T, which provides a good description of the soft part of the spectrum. The fit is performed for each transverse momentum spectrum in the range $0.15 \, \mathrm{GeV}/c < p_T < 1.0 \, \mathrm{GeV}/c$. The relative fraction of the extrapolated yield is between 10.9% and 12.7% of the total yield for $\sqrt{s}$ = 2.76 TeV and 13 TeV data, respectively. The statistical uncertainties of the $\langle p_T \rangle$ are negligible, while the systematic uncertainties are estimated by fitting the shifted measured spectrum up and down by their systematic uncertainty, as well as by changing the fit range to $0.15 \, \mathrm{GeV}/c < p_T < 0.5 \, \mathrm{GeV}/c$, and by varying the low-p_T interpolation range to $0 - 0.2 \, \mathrm{GeV}/c$. All contributions are added quadratically to obtain the total systematic uncertainty.

Figure 4.12 shows the results of $\langle p_T \rangle$ vs $\sqrt{s}$ for INEL pp collisions from ALICE and the results from other experiments [110–115]. The results are found to be slightly higher than previous measurements from pp and p$\bar{\text{p}}$ collisions at the same energy but measured in a larger η region, like CMS [111]
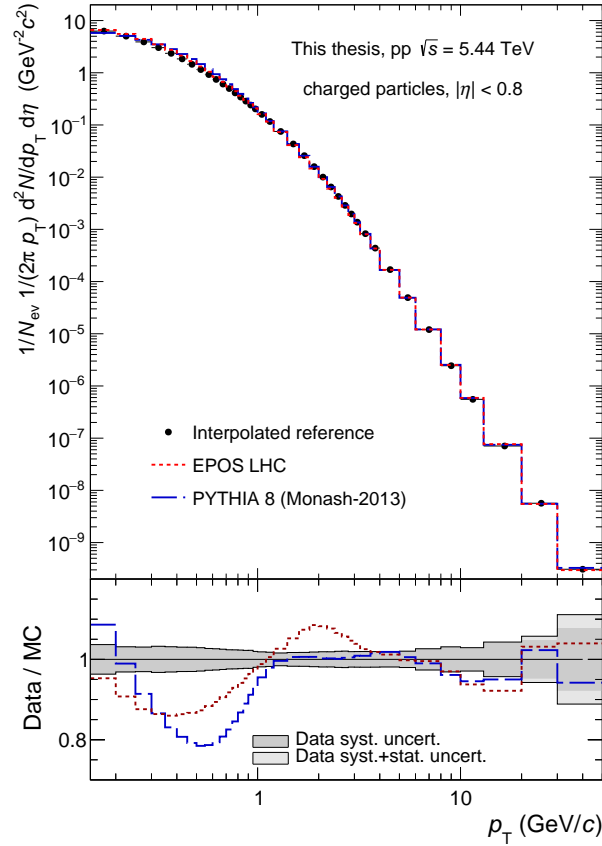
Figure 4.11: Top: Generated pp spectra with the PYTHIA8 Monash and EPOS LHC event generators at different $\sqrt{s}$. Bottom: ratio of the two energies, applied as scaling to the measured $\sqrt{s} = 5.02$ TeV spectrum.

($|\eta| < 2.4$) and UA1 [112] ($|\eta| < 2.5$). The observed hardening can be attributed to the pseudorapidity range in which the spectrum was measured. At small values of η, hard processes are more frequent due to the large momentum transfered (Q^2) in the collision. A quadratic increase trend in $ln(\sqrt{s})$ was found in the results from previous experiments at energies that go from $\sqrt{s} = 23$ GeV to 7 TeV. From the results of this thesis, an increasing trend is observed in the $\langle p_\mathrm{T} \rangle$ the energy range of $\sqrt{s} = 0.9$ TeV to 13 TeV, similar to what was observed in previous measurements. PYTHIA values agree with data within uncertainties but only at $\sqrt{s} = 2.76$ TeV and 5.02 TeV. At larger collision energies, PYTHIA clearly overestimate the $\langle p_\mathrm{T} \rangle$ measurement. EPOS exhibit an opposite behavior, at $\sqrt{s} = 7$ TeV and 13 TeV it agrees best the results; while at lower energies EPOS underestimated them.
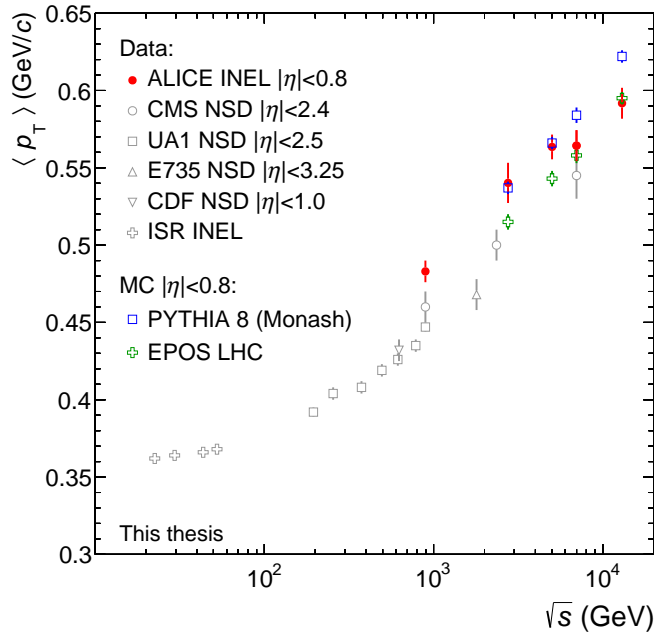
Figure 4.12: Energy dependence of the average transverse momentum of primary charged particles in pp and p$\overline{\text{p}}$ from ALICE and other experiment measurements. ALICE data at $\sqrt{s}$ = 900 GeV is taken from [110]. Data from other experiments are taken from [111–115]. The bars represent the systematic uncertainties.

Multiplicity dependence

The transverse momentum spectra of charged particles for pp collisions was studied as a function of the event multiplicity in the acceptance ($N_{\text{ch}}^{\text{acc}}$). The multiplicity estimator is based on the number of reconstructed tracks in the transverse momentum acceptance of $0.15 < p_{\text{T}} < 50\,\text{GeV}/c$ and in the pseudorapidity range of $|\eta| < 0.8$. The spectra in multiplicity intervals use the minimum bias corrections, as described in Section 7, with the assumption that the multiplicity dependence is negligible.

Three different multiplicity ranges are studied. The low multiplicity covers from one charged particle to the mean multiplicity $\langle N_{\text{ch}}^{\text{acc}}\rangle$, which is energy-dependent. The intermediate multiplicity is studied in the range $\langle N_{\text{ch}}^{\text{acc}}\rangle \leqslant N_{\text{ch}}^{\text{acc}} < 2\langle N_{\text{ch}}^{\text{acc}}\rangle$. And the high multiplicity class contains all events with $N_{\text{ch}}^{\text{acc}} > 2\langle N_{\text{ch}}^{\text{acc}}\rangle$.

Figure 4.13 shows the transverse momentum spectrum for minimum bias pp collisions at $\sqrt{s}$ = 13 TeV, as well as for the three multiplicity ranges studied. The spectrum are normalized to their integral, with the purpose to compare the spectral shape.
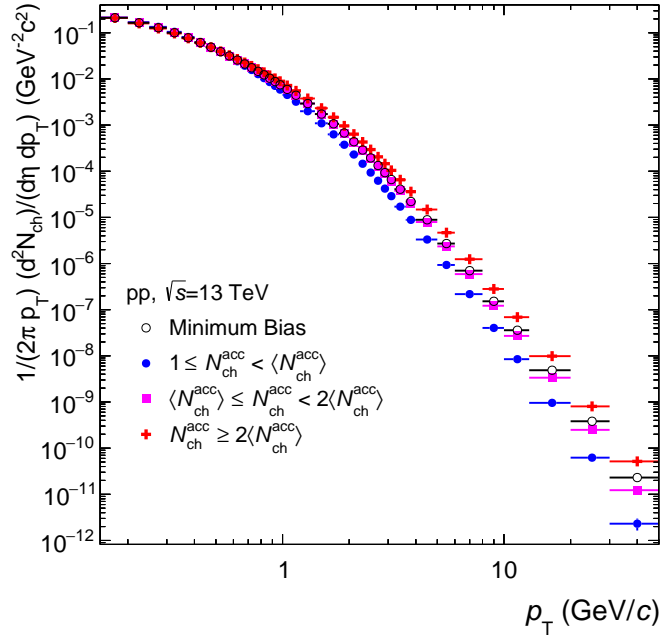
Figure 4.13: Transverse momentum spectra in accepted multiplicity ranges and the MB bias measurement for pp collisions at $\sqrt{s}$=13 TeV. The spectra is normalized individually to their integral. Statistical uncertainties are represented as bars.

Figure 4.14 shows the ratio of transverse momentum spectra measured in multiplicity intervals to the inclusive INEL spectrum for pp collisions at $\sqrt{s}$ = 2.76 TeV and 5.02 TeV. The results are compared to PYTHIA 8 (Monash Tune) and EPOS LHC MC simulations in comparable multiplicity ranges according to the mean true multiplicity $\langle N_{\mathrm{ch}} \rangle$. The MC ratios show similar trends when compared to data. At low and intermediate multiplicity, the simulations fail to describe the data in the transverse momentum range of $1\,\mathrm{GeV}/c < p_{\mathrm{T}} < 10\,\mathrm{GeV}/c$, approximately. In high multiplicity events, the data and MC agree relatively well up to $p_{\mathrm{T}} < 4\,\mathrm{GeV}/c$. Figure 4.15 shows similar ratios of the spectra in multiplicity ranges to the inclusive measurement but for $\sqrt{s}$ = 7 TeV and 13 TeV data.

The multiplicity to INEL ratios and the MC simulations show similar trends for low, intermediate and high multiplicity events in all pp collision energies.
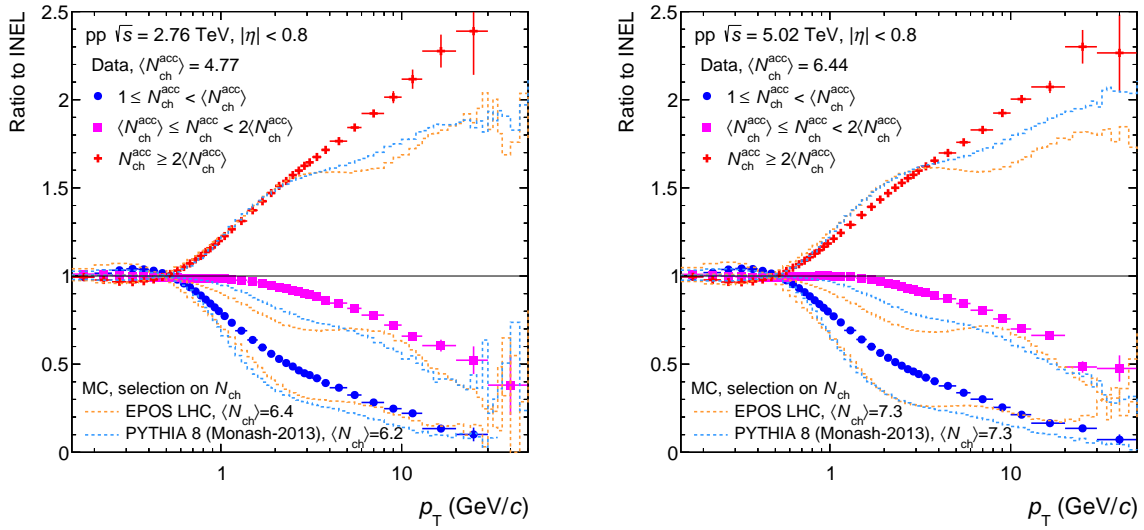
Figure 4.14: Ratios of transverse momentum distribution of charged particles in three multiplicity intervals to the inclusive spectra for INEL pp collisions at $\sqrt{s}$ = 2.76 TeV (left) and 5.02 TeV (right). The spectra were normalized to the integral previous to division. The data is compared to EPOS LHC and PYTHIA 8 simulations.
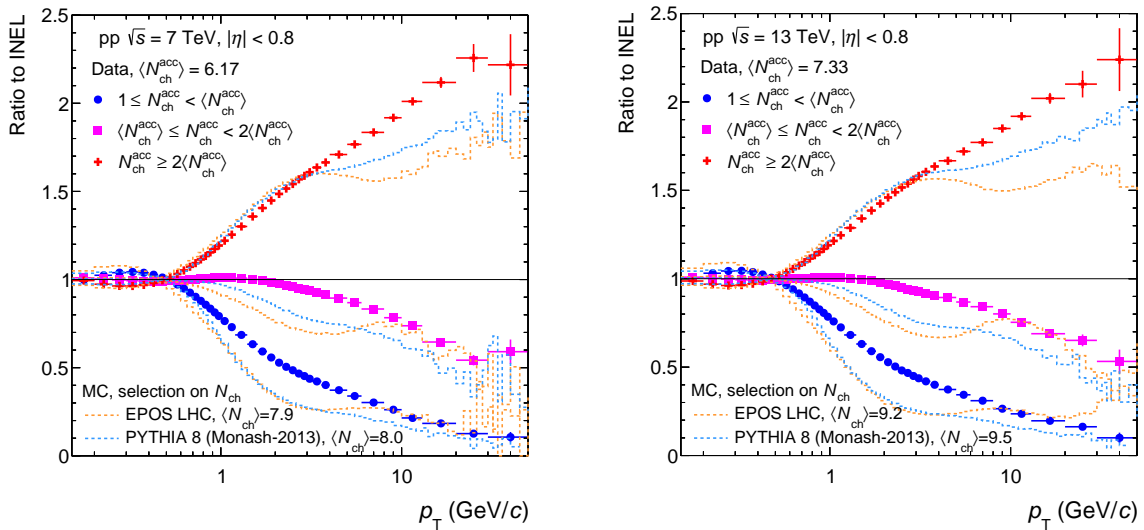

Figure 4.15: Ratios of transverse momentum distribution of charged particles in three multiplicity intervals to the inclusive spectra for INEL pp collisions at $\sqrt{s}$ = 7 TeV (left) and 13 TeV (right). The spectra were normalized to the integral previous to division. The data is compared to EPOS LHC and PYTHIA 8 simulations.

The average number of charged particles $\langle \mathrm{d}N_{\mathrm{ch}}/\mathrm{d}\eta \rangle$ as a function of center-of-mass energy ($\sqrt{s}$) is shown in Figure 4.16. The total $\langle \mathrm{d}N_{\mathrm{ch}}/\mathrm{d}\eta \rangle$ is calculated from the measured transverse momentum distributions and from the low-p_{T} extrapolation part. A Hagedorn function (eq.4.2) is used to complete the low-p_{T} region. The systematic uncertainties are computed in a similar way as described in Section 3, shifting the measured spectra within systematic uncertainties and varying the extrapolation region. The $\langle \mathrm{d}N_{\mathrm{ch}}/\mathrm{d}\eta \rangle$ as a function of $\sqrt{s}$ results show an increase from 3.03 ± 0.32 to 5.41 ± 0.20 and exhibit a quadratic dependence. In previous ALICE measurements, the $\langle \mathrm{d}N_{\mathrm{ch}}/\mathrm{d}\eta \rangle$

was calculated from the charged particle pseudorapidity distribution [108, 116], which is based on the reconstruction of tracklets (hits in the SPD layers and the reconstructed primary vertex position). The results from this thesis are compared to previous ALICE measurements ($|\eta| < 0.5$) and found to be in good agreement within systematic uncertainties.
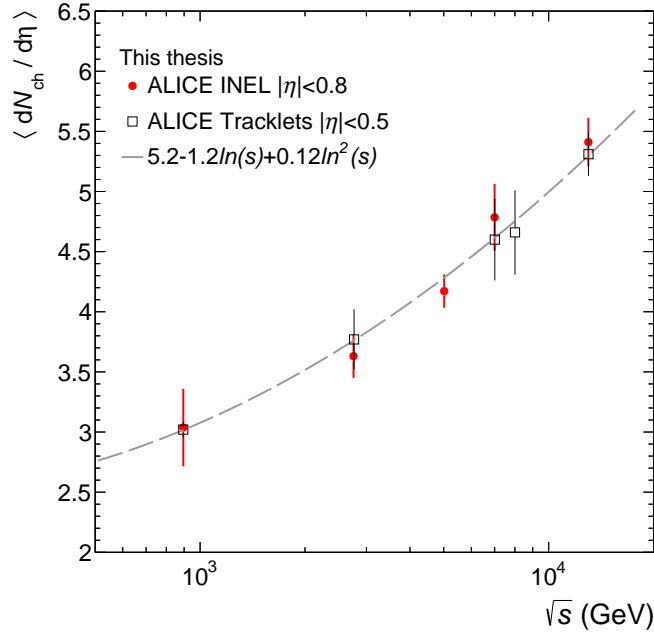

Figure 4.16: Measurement of $\langle \mathrm{d}N_{\mathrm{ch}}/\mathrm{d}\eta \rangle$ as a function of $\sqrt{s}$ from the ALICE INEL pp spectrum. The ALICE result at $\sqrt{s}$ = 900 GeV is taken from [110]. Values from the tracklets method are from [108, 116, 117]. Vertical bars represent the systematic uncertainties for each measurement.

Nuclear modification factor for Pb-Pb and Xe-Xe collisions

In order to study the in-medium modification of the charged particle spectra, the nuclear modification factor is a quantity t/hat provides information about the in-medium suppression of hight-p_{T} particles in heavy-ion collisions with respect to the production in pp collisions. It is calculated as follows:

$$R_{AA} = \frac{\mathrm{d}^2 N_{\mathrm{ch}}^{\mathrm{AA}}/\mathrm{d}\eta\,\mathrm{d}p_{\mathrm{T}}}{\langle T_{\mathrm{AA}} \rangle \times \mathrm{d}^2 \sigma_{\mathrm{ch}}^{\mathrm{pp}}/\mathrm{d}\eta\,\mathrm{d}p_{\mathrm{T}}} \tag{4.3}$$

The nuclear modification factor is calculated for Pb-Pb and Xe-Xe collisions at $\sqrt{s_{\mathrm{NN}}}$ = 5.02 TeV and 5.44 TeV, respectively [118]. Figure 4.17 shows the R_{AA} for both systems, where a strong centrality dependence is observed. A larger suppression is observed for R_{AA} in Pb-Pb when compared to Xe-Xe, for the nine centralities studied. In central collisions ($0 - 5\%$) and at p_{T} = $6 - 7\,\mathrm{GeV}/c$, the yield is suppressed by a factor 8 for Pb-Pb ($R_{\mathrm{AA}} \approx 0.13$) and a factor 6 for Xe-Xe ($R_{\mathrm{AA}} \approx 0.18$). At high-$p_{\mathrm{T}}$ ($30\,\mathrm{GeV}/c < p_{\mathrm{T}} < 50\,\mathrm{GeV}/c$), there is a significant rise of the nuclear modification factor that reaches a value of 0.4 for Pb-Pb. The R_{AA} for Xe-Xe is around 50% larger than Pb-Pb for the same

centrality. As the centrality increases, i.e. towards peripheral collisions, the nuclear modification factor increases, suggesting that suppression of charged particles in the medium becomes smaller in both systems.

In the most peripheral Pb-Pb collisions ($70-80\%$), the suppression is around 30% for intermediate-p_{T} and reaches unity for high-p_{T} particles. For the case of Xe-Xe, there is a constant 10% suppression for $p_{\mathrm{T}} > 7\,\mathrm{GeV}/c$.

The normalization uncertainty for R_{AA} is shown as a colored bar at unity in Figure 4.17. It is calculated as the sum in quadrature of the pp measurement (cross section uncertainty) and centrality determination uncertainty. Due to the imprecision on the charge-density distribution of the deformed ^{129}Xe nucleus, it results in a larger relative uncertainty in $\langle \mathrm{T_{AA}} \rangle$ [119] when compared to ^{208}Pb.
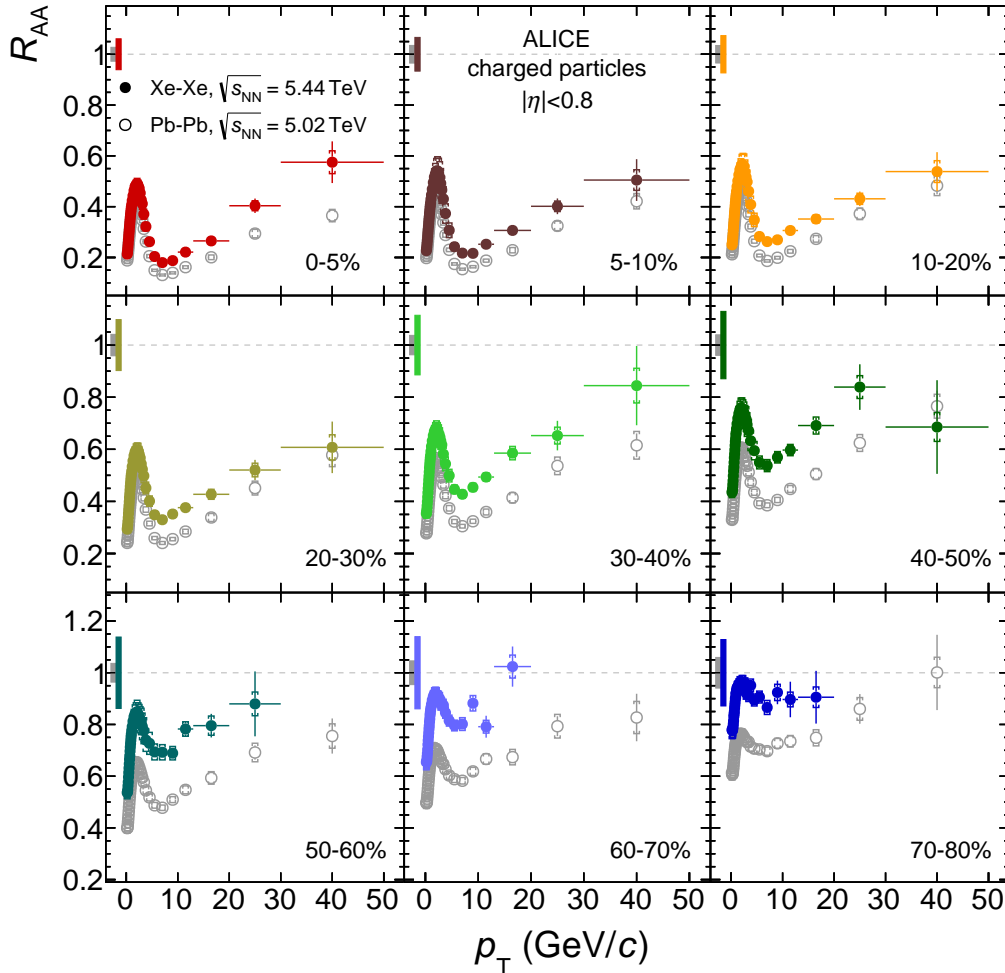

Figure 4.17: Nuclear modification factor in Xe-Xe collisions at $\sqrt{s_{\mathrm{NN}}} = 5.44$ TeV (filled markers) and Pb-Pb collisions at $\sqrt{s_{\mathrm{NN}}} = 5.02$ TeV (open markers) in nine centrality classes. The brackets represent the systematic uncertainties and the vertical lines the statistical errors. The overall normalization uncertainty is shown as colored bar around unity. Figure published in [105].

Figure 4.18 shows the ratio of $R_{\mathrm{XeXe}}/R_{\mathrm{PbPb}}$ in nine centrality classes. In the $0-5\%$ centrality class,

a clear structure appears after $p_T > 3\,\mathrm{GeV}/c$ while for low-p_T the ratio shows a flat distribution. Towards peripheral collisions, the structure reduces gradually until it vanishes completely in the $70 - 80\%$ range. The nuclear modification factors from Pb-Pb and Xe-Xe collisions and their ratios in similar mean multiplicities ranges $\langle \mathrm{d}N_{\mathrm{ch}}/\mathrm{d}\eta \rangle$ are shown in Figure 4.19. For central Xe-Xe collisions $(0 - 5\%)$, the average number of participants and average multiplicity is $\langle N_{\mathrm{part}} \rangle = 236 \pm 2$ and $\langle \mathrm{d}N_{\mathrm{ch}}/\mathrm{d}\eta \rangle = 1167 \pm 24$, while for Pb-Pb collisions in 10-20% centrality range is $\langle N_{\mathrm{part}} \rangle = 263 \pm 4$ and $\langle \mathrm{d}N_{\mathrm{ch}}/\mathrm{d}\eta \rangle = 1180 \pm 31$. Despite the clear difference between the $\langle N_{\mathrm{part}} \rangle$ values, the ratio of the nuclear modification factor from both systems are in a remarkable agreement. In the comparison of 30-40% Xe-Xe and 40-50% Pb-Pb, the large systematic uncertainties do not allow to give a definitive conclusion. The compatibility in the nuclear modification factors at similar values of average multiplicity is in agreement with results from the study of fractional momentum loss of high-p_T partons at RHIC and at the LHC [120]. The ratios at similar multiplicities supports the idea that the R_{AA} ratios in the same centrality classes is not a correct comparison, since the multiplicities or the medium sizes are not comparable between the two systems.
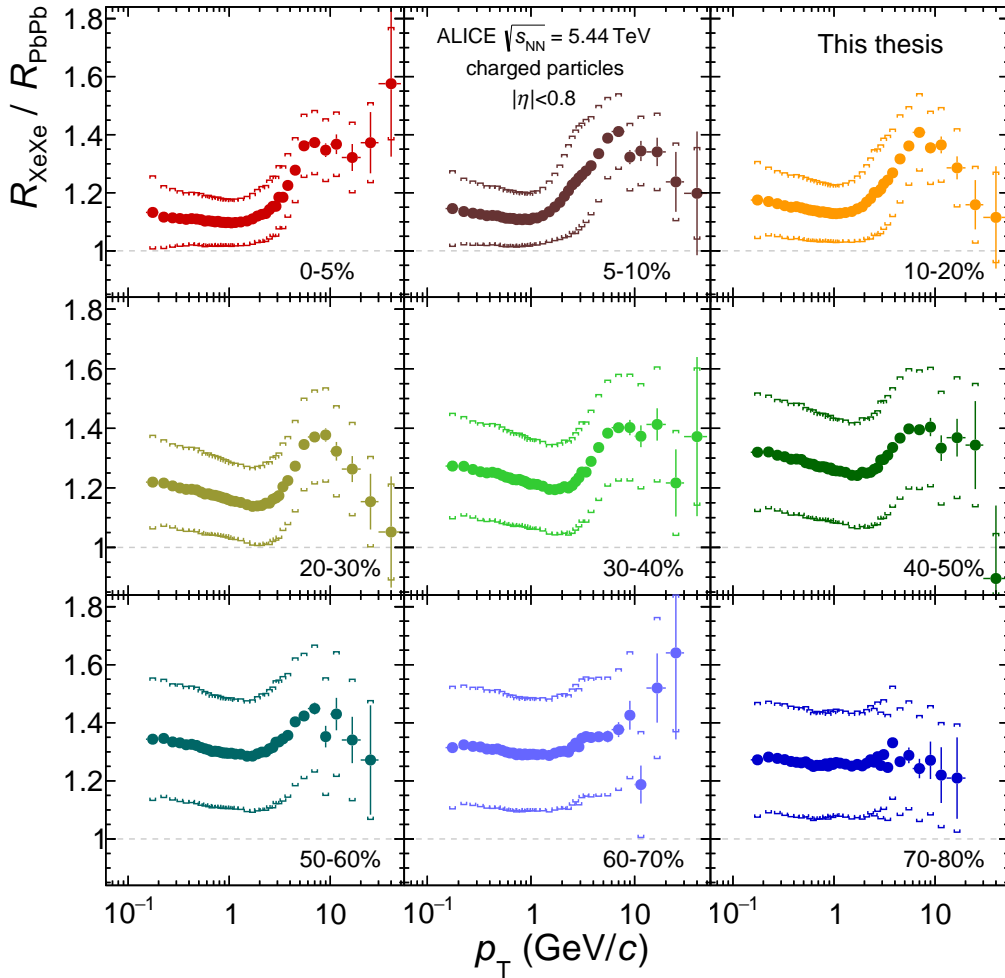

Figure 4.18: Ratio of nuclear modification factors in Xe-Xe and Pb-Pb for nine centrality classes. Vertical lines represent the statistical uncertainties while the brackets are the systematic and normalization uncertainty.

The R_{AA} in three different p_T regions (low, medium and high) for Xe-Xe collision at $\sqrt{s} = 5.44$ TeV
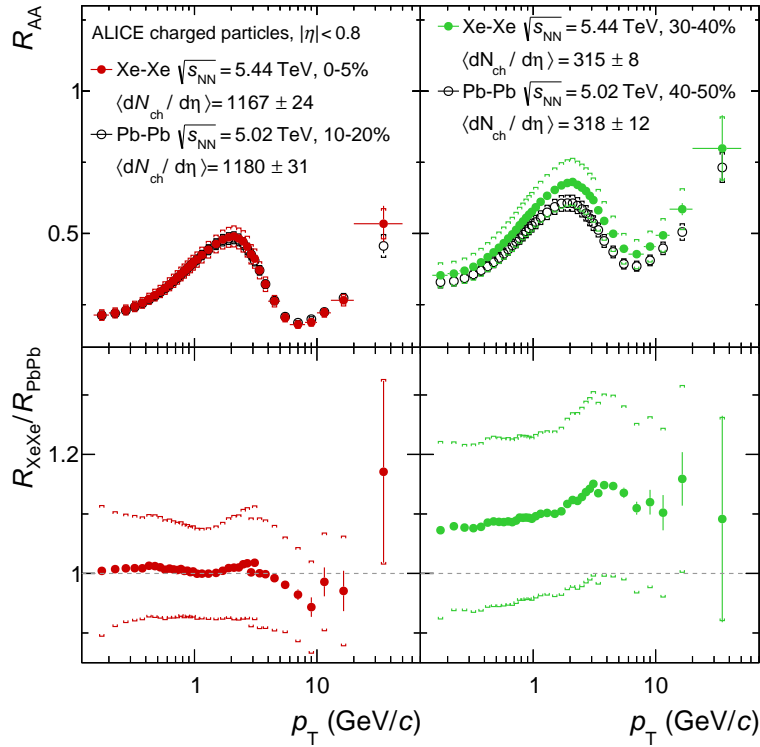
Figure 4.19: Comparison of nuclear modification factors in Xe-Xe (full points) and Pb-Pb (open points) collisions for similar ranges of mean multiplicity, 0-5% (left) and 30-40% (right) Xe-Xe centrality classes. The brackets represent the systematic plus normalization uncertainties and the vertical lines the statistical errors. Plot published in [105].

and Pb-Pb collisions at $\sqrt{s}$ = 5.02 TeV and 2.76 TeV as a function of $\langle \mathrm{d}N_{\mathrm{ch}}/\mathrm{d}\eta \rangle$ is shown in Figure 4.20. The upper panel shows the average R_{AA} value at the flow bump, $1.2 < p_{\mathrm{T}} < 4.2\,\mathrm{GeV}/c$. The middle panel is for $5\,\mathrm{GeV}/c < p_{\mathrm{T}} < 8\,\mathrm{GeV}/c$ (the local minimum) and the lower panel shows the R_{AA} in the high-p_{T} rise, between $10\,\mathrm{GeV}/c < p_{\mathrm{T}} < 20\,\mathrm{GeV}/c$. A remarkable agreement between R_{AA} is observed for Xe-Xe and Pb-Pb collisions for the average multiplicity range $\langle \mathrm{d}N_{\mathrm{ch}}/\mathrm{d}\eta \rangle > 500$. This similarity holds in the region where the hydrodynamical expansion of the medium dominates (low-p_{T}) and in the region where parton energy loss inside the medium influences the spectral shape (high-p_{T}). At $\langle \mathrm{d}N_{\mathrm{ch}}/\mathrm{d}\eta \rangle < 500$, there is an agreement within the large systematic uncertainties from the R_{XeXe}, which are mainly driven by the normalization uncertainty.

In a simple radiative energy loss approach, the average energy loss can be seen as proportional to the square of the path length of the parton in the medium and to the density of scattering centers.

$$\langle \Delta E \rangle \propto \varepsilon \cdot L^2 \tag{4.4}$$

The energy density can be approximated to the average charged particle multiplicity density divided by the transverse area [121], $\varepsilon \propto \langle \mathrm{d}N_{\mathrm{ch}}/\mathrm{d}\eta \rangle / A_{\mathrm{T}}$. The initial transverse area is related to the radius of the nucleus in central collisions as $A_{\mathrm{T}} = \pi \cdot r^2$ [119], and the path length of a high-p_{T} parton that travels trough the medium is proportional to r. Therefore, assuming these considerations the

average energy loss can be reduced to be proportional to the mean multiplicity as:

$$\langle \Delta E \rangle \propto \frac{1}{\pi \cdot r^2} \cdot \langle \mathrm{d}N_{\mathrm{ch}}/\mathrm{d}\eta \rangle \cdot r^2 \propto \langle \mathrm{d}N_{\mathrm{ch}}/\mathrm{d}\eta \rangle \qquad (4.5)$$

The comparison of the measured R_{AA} in two colliding systems can give insights into the path length dependence of the radiative energy loss in the hot and dense medium created in each system. Two theoretical models are compared to the results [122], one assumes a static or constant temperature in the medium and the other considers a Bjorken expansion of the medium. Both models exhibit different trends with respect to data. At $5\,\mathrm{GeV}/c \ < \ p_{\mathrm{T}} \ < 8\,\mathrm{GeV}/c$, the models underestimate the results especially at low $\langle \mathrm{d}N_{\mathrm{ch}}/\mathrm{d}\eta \rangle$. In the high-$p_{\mathrm{T}}$ region ($10\,\mathrm{GeV}/c \ < \ p_{\mathrm{T}} \ < 20\,\mathrm{GeV}/c$), the models agree better with R_{AA} but not in detail, since for $\langle \mathrm{d}N_{\mathrm{ch}}/\mathrm{d}\eta \rangle > 1000$ they are slightly above the data and follow a different trend.
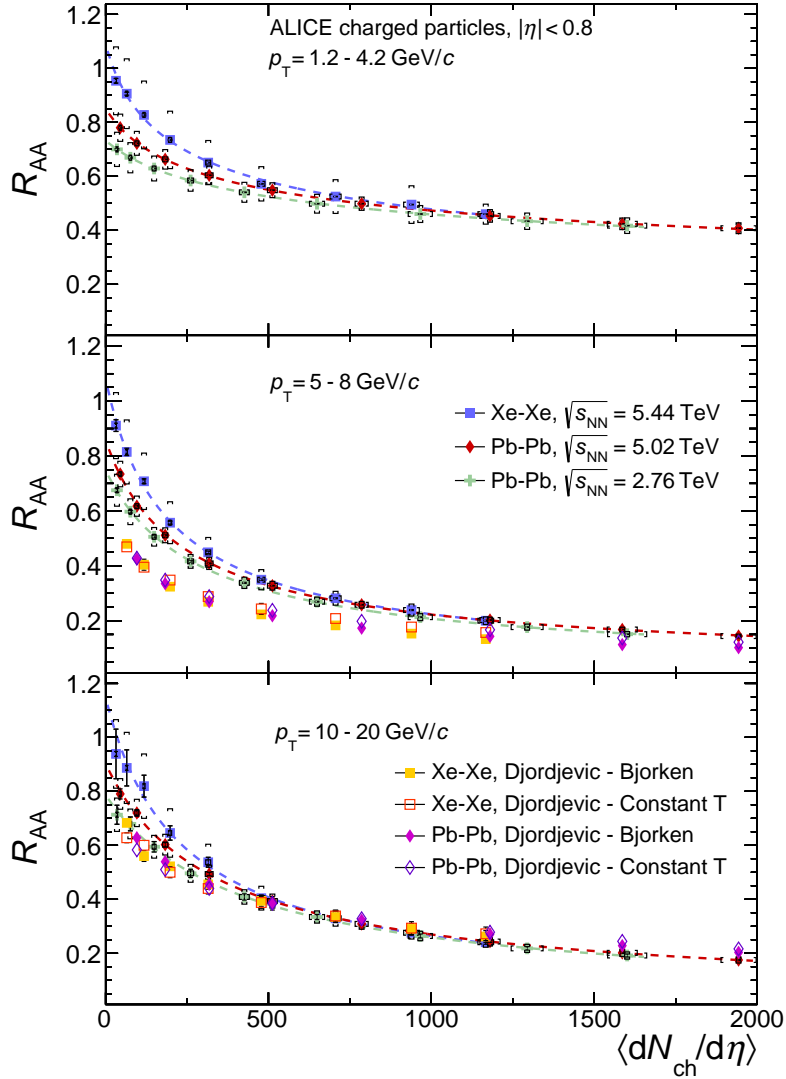
Figure 4.20: Comparison of the nuclear modification factor in Xe-Xe and Pb-Pb collisions integrated over three p_T regions as a function of $\langle \mathrm{d}N_{ch}/\mathrm{d}\eta \rangle$. The upper panel correspond to $1.2\,\mathrm{GeV}/c < p_T < 4.2\,\mathrm{GeV}/c$, the middle panel is for $5\,\mathrm{GeV}/c < p_T < 8\,\mathrm{GeV}/c$ and the bottom to $10\,\mathrm{GeV}/c < p_T < 20\,\mathrm{GeV}/c$. The brackets indicate the quadratic sum of the total systematic uncertainty from the measurement and the overall normalization uncertainty in $\langle T_{AA} \rangle$. The horizontal bars correspond to the RMS of the distribution in each bin. The dashed line is a power law fit to the data only for guidance purposes. The data is compared to Model calculations assuming a constant medium temperature T and a Bjorken medium expansion for Xe-Xe and Pb-Pb [122].

Chapter 5

Summary and Outlook

The differential production cross section for primary charged particles from inelastic (INEL) pp collisions at $\sqrt{s}$ = 2.76 TeV, 5.02 TeV, 7 TeV and 13 TeV have been measured in ALICE at the LHC. The particles were studied in the acceptance range of $0.15\,\mathrm{GeV}/c < p_\mathrm{T} < 50\,\mathrm{GeV}/c$ and in the pseudorapidity range of $|\eta| < 0.8$. The comparison with the already published results yields good agreement at low-p_T ($< 1\,\mathrm{GeV}/c$) and at high-p_T ($> 10\,\mathrm{GeV}/c$), within systematic uncertainties. At $1\,\mathrm{GeV}/c < p_\mathrm{T} < 7\,\mathrm{GeV}/c$, a maximum difference of 9% was found that is directly related to the correction methods.

The systematic uncertainties have been reduced for all collision energies by around 30% in pp collisions at $\sqrt{s}$ = 2.76 TeV, a reduction of a factor four at $\sqrt{s}$ = 5.02 TeV, and approximately a factor of two at $\sqrt{s}$ = 7 TeV and 13 TeV. The improved precision is the result of the new and updated correction methods used in the analysis such as the data-driven particle composition and the correction for contamination by secondary particles as well as from the inclusion of the new track selection criteria based on the track length in the inactive area of the TPC read-out.

The contamination by secondary particles was one of the corrections that was improved with respect to previous analyses. In general, is known since long that MC event generators underestimate the amount of secondaries by around 40% to 60% for pp collisions at $\sqrt{s}$ = 5.02 TeV, 7 TeV and 13 TeV, and by almost a factor two at $\sqrt{s}$ = 2.76 TeV. The data-driven correction is based on the measurement of the distance of closest approach to the primary vertex.

The largest correction was due to the tracking efficiency and acceptance as obtained from the PYTHIA event generator. An additional correction to the MC tracking efficiency has been implemented that accounts for the imprecision to reproduce the measured particle abundances. At $2\,\mathrm{GeV}/c < p_\mathrm{T} < 4\,\mathrm{GeV}/c$, the new and more precise particle composition correction had a major impact, of the order of 6%, on the transverse momentum spectrum with respect to the published results.

The EPOS LHC and PYTHIA 8 (Monash) MC event generators overestimate the transverse momentum spectra at $p_\mathrm{T} < 1\,\mathrm{GeV}/c$, regardless of the collision energy. PYTHIA was found to agree better with data at $p_\mathrm{T} > 1\,\mathrm{GeV}/c$, but only for pp collisions at $\sqrt{s}$ = 5.02 TeV and 7 TeV.

The results of transverse momentum spectra at $\sqrt{s}$ = 5.02 TeV over 2.76 TeV and $\sqrt{s}$ = 13 TeV to 7 TeV showed similar trends and significant hardening for the larger collision energies. This hardening of the spectra, of the order of factor two, is originated from the increase in the collision energy, causing an enhancement in the amount of hard processes that produce more particles at higher p_T. The EPOS LHC and PYTHIA 8 simulations revealed a qualitatively good agreement of this trend in the ratios over all the p_T range studied.

The differential cross section for pp collisions at $\sqrt{s}$ = 5.44 TeV was constructed to be the reference for the Xe-Xe data. A power law function that interpolates between the invariant cross section at $\sqrt{s}$ = 5.02 TeV and 7 TeV data was used. PYTHIA 8 Monash was found to be the generator that describes best the interpolated reference at $p_T > 1\,\mathrm{GeV}/c$, between 10%.

The measurement of the average transverse momentum $\langle p_T \rangle$ is dominated by the soft part of the spectrum, but still sensitive to the spectra hardening as the collisional energy increases. The results of $\langle p_T \rangle$ as a function of the center-of-mass energy exhibited a similar quadratic increase trend with respect to previous experiments, like CMS ($|\eta| < 2.4$), UA1 ($|\eta| < 2.5$), E735 ($|\eta| < 3.25$) and CDF ($|\eta| < 1.0$). A larger $\langle p_T \rangle$ was seen in the results with respect to previous experiments, which came from the different pseudorapidity region used, since the $|\eta| < 0.8$ has a stronger bias for jets or hard collisions than a broader region.

The average multiplicity $\langle \mathrm{d}N_{\mathrm{ch}}/\mathrm{d}\eta \rangle$ was obtained from the integral of the transverse momentum spectrum in INEL pp collisions. An increasing quadratic trend in $ln(\sqrt{s})$ as a function of center-of-mass energy was found. Excellent agreement was found with the multiplicity results from the tracklets method.

The transverse momentum spectra has been measured as a function of the primary charged particle multiplicity, measured in the TPC detector. Three multiplicity ranges were selected according to the average multiplicity in pp collisions at each energy, and compared to the minimum bias measurement. A significant hardening was observed for the high multiplicity interval. However, the opposite behavior was found in the low multiplicity region. The comparison of the results with EPOS and PYTHIA models highlighted some deficiencies in both models to describe the spectral shapes as a function of multiplicity. A weak center-of-mass energy dependence was observed in the multiplicity ratios to the INEL measurement.

The R_{AA} for Pb-Pb collisions at $\sqrt{s_{\mathrm{NN}}}$ = 5.02 TeV and Xe-Xe at $\sqrt{s_{\mathrm{NN}}}$ = 5.44 TeV showed a clear centrality dependence. In central collisions, a strong suppression was observed with the minimum at $p_T \sim 6\,\mathrm{GeV}/c$ in both systems. In peripheral collisions, R_{AA} was approximately constant and reached unity at high-p_T. Less suppression was found in Xe-Xe data compared to Pb-Pb for all centralities. This would indicate that the size of the medium created is different due to the smaller Xe nuclei, but a multiplicity analysis proved that centrality is not the best observable to compare system sizes.

The medium size was studied with the average multiplicity of charged particles in Xe-Xe and Pb-Pb collisions. At similar multiplicities, the R_{AA} ratios between both systems was in agreement with unity within the small systematic uncertainties. At $p_T = 1.2 - 4.2$ GeV/c, the R_{AA} for Pb-Pb collisions at $\sqrt{s_{\mathrm{NN}}}$ = 2.76 TeV was lower than the R_{AA} Pb-Pb collisions at $\sqrt{s_{\mathrm{NN}}}$ = 5.02 TeV and Xe-Xe collisions

at $\sqrt{s}$ = 5.44 TeV. This behavior is attributed to the increase of radial flow with the increase in collision energy. At p_T = $10 - 20$ GeV/c, a remarkable agreement was found in the R_{AA} between Pb-Pb and Xe-Xe for $\langle dN_{ch}/d\eta \rangle$ larger than 500 charged particles, approximately. In a simplified parton energy-loss scenario, the agreement between the systems was consistent with a squared path length dependence (L^2) of parton traversing the medium. The theoretical predictions, based on the assumption of a Bjorken-like expanding medium and a medium with constant temperature exhibited a different trend than data and underestimated it at p_T = $5 - 8$ GeV/c.

Outlook

The results presented in this thesis leave still room for improvements. For example, in pp collisions a larger p_T coverage up to 100 GeV/c would extend the region of the nuclear modification factor to that transverse momentum, and access into the truly perturbative regime in QCD. To achieve this, more than a factor five the amount of the already analyzed data is needed. In the specific case of pp collisions at $\sqrt{s}$ = 5.02 TeV, in 2017 ALICE has collected ten times more data than the analyzed in this thesis (based on 2015 data). Another possible improvement is in the systematic uncertainties that can be reduced by increasing the precision of the transverse momentum spectra for identified particles and, in addition, the measurement of the $\Sigma^-, \overline{\Sigma}^-$ and $\Sigma^+, \overline{\Sigma}^+$ particles. A detailed analysis on charged particle multiplicity would benefit the medium size study rather than slicing in centrality ranges. The path-length dependence energy-loss of a parton in the medium can be studied more precisely with collision from different nuclear sizes. For run 3 and run 4, the TPC at ALICE will be upgraded and will allow to extract particle identification up to the Fermi-plateau (π up to 48 GeV/c), which will allow the study of parton energy loss of gluons and quarks via pions and protons, respectively.

Bibliography

[1] S. Chatrchyan and others (**CMS** Collaboration), "Observation of a new boson at a mass of 125 GeV with the CMS experiment at the LHC," *Phys. Lett.*, vol. B716, pp. 30–61, 2012.

[2] G. Aad and others (**ATLAS** Collaboration), "Observation of a new particle in the search for the Standard Model Higgs boson with the ATLAS detector at the LHC," *Phys. Lett.*, vol. B716, pp. 1–29, 2012.

[3] M. Tanabashi *et al.*, "Review of particle physics (**PDG** collaboration)," *Phys. Rev. D*, vol. 98, p. 030001, Aug 2018.

[4] G. Sterman *et al.*, "Handbook of perturbative QCD," *Rev. Mod. Phys.*, vol. 67, pp. 157–248, Jan 1995.

[5] R. Placakyte, "Parton Distribution Functions," in *Proceedings, 31st International Conference on Physics in collisions (PIC 2011): Vancouver, Canada, August 28-September 1, 2011*, 2011.

[6] K. Nagano and others (**ZEUS** Collaboration), "Parton Distribution Functions: Impact of HERA," in *Hadron collider physics. Proceedings, 19th Symposium, HCP2008, Galena, USA, May 27-31, 2008*, 2008.

[7] A. Polyakov, "Thermal properties of gauge fields and quark liberation," *Physics Letters B*, vol. 72, no. 4, pp. 477 – 480, 1978. [Online]. Available: http://www.sciencedirect.com/science/article/pii/0370269378907372

[8] L. Susskind, "Lattice models of quark confinement at high temperature," *Phys. Rev. D*, vol. 20, pp. 2610–2618, Nov 1979. [Online]. Available: https://link.aps.org/doi/10.1103/PhysRevD.20.2610

[9] J. C. Collins and M. J. Perry, "Superdense matter: Neutrons or asymptotically free quarks?" *Physical Review Letters*, vol. 34, pp. 1353–1356, May 1975.

[10] F. Karsch and E. Laermann, "Thermodynamics and in medium hadron properties from lattice QCD," pp. 1–59, 2003.

[11] T. Bhattacharya *et al.*, "QCD Phase Transition with Chiral Quarks and Physical Quark Masses," *Phys. Rev. Lett.*, vol. 113, no. 8, p. 082001, 2014.

[12] P. Braun-Munzinger and J. Wambach, "The Phase Diagram of Strongly-Interacting Matter," *Rev. Mod. Phys.*, vol. 81, pp. 1031–1050, 2009.

[13] Z. Fodor and S. D. Katz, "Lattice determination of the critical point of QCD at finite T and mu," *JHEP*, vol. 03, p. 014, 2002.

[14] M. G. Alford, A. Schmitt, K. Rajagopal, and T. Schäfer, "Color superconductivity in dense quark matter," *Rev. Mod. Phys.*, vol. 80, pp. 1455–1515, 2008.

[15] H. Oeschler, J. Cleymans, K. Redlich, and S. Wheaton, "Statistical Model and the mesonic-baryonic transition region," *PoS*, vol. CPOD2009, p. 032, 2009.

[16] C. Schmidt and S. Sharma, "The phase structure of QCD," *J. Phys.*, vol. G44, no. 10, p. 104002, 2017.

[17] A. Andronic, P. Braun-Munzinger, and J. Stachel, "Thermal hadron production in relativistic nuclear collisions: The Hadron mass spectrum, the horn, and the QCD phase transition," *Phys. Lett.*, vol. B673, pp. 142–145, 2009, [Erratum: Phys. Lett.B678,516(2009)].

[18] P. Braun-Munzinger, K. Redlich, and J. Stachel, "Particle production in heavy ion collisions," pp. 491–599, 2003.

[19] M. Gyulassy and L. McLerran, "New forms of QCD matter discovered at RHIC," *Nucl. Phys.*, vol. A750, pp. 30–63, 2005.

[20] F. Gelis, "Color Glass Condensate and Glasma," *Int. J. Mod. Phys.*, vol. A28, p. 1330001, 2013.

[21] M. Strickland, "Anisotropic Hydrodynamics: Three lectures," *Acta Phys. Polon.*, vol. B45, no. 12, pp. 2355–2394, 2014.

[22] E. Iancu, "Theory summary for ISMD2000," in *Proceedings, 40th International Symposium on Multiparticle Dynamics (ISMD 2010): Antwerp, Belgium, September 21-25, 2010*, 2011, pp. 411–437.

[23] U. A. Wiedemann, "Jet Quenching in Heavy Ion Collisions," *CERN-PH-TH-2009-026*, pp. 521–562, 2010.

[24] J. Bjorken, "Energy Loss of Energetic Partons in Quark - Gluon Plasma: Possible Extinction of High p T Jets in Hadron - Hadron Collisions," *FERMILAB-PUB-82-059-T*.

[25] D. d'Enterria, "Jet quenching," *Landolt-Bornstein*, vol. 23, p. 471, 2010.

[26] S. Peigne, "Collisional Energy Loss of a Fast Parton in a QGP," *AIP Conf. Proc.*, vol. 1038, pp. 139–148, 2008.

[27] K. Adcox *et al.*, "Suppression of hadrons with large transverse momentum in central Au+Au collisions at $\sqrt{s_{NN}}$ = 130-GeV," *Phys. Rev. Lett.*, vol. 88, p. 022301, 2002.

[28] A. Adare and others (**PHENIX** Collaboration), "Suppression pattern of neutral pions at high transverse momentum in Au + Au collisions at $\sqrt{s_{NN}}$ = 200-GeV and constraints on medium transport coefficients," *Phys. Rev. Lett.*, vol. 101, p. 232301, 2008.

[29] J. Adams and others (**STAR** Collaboration), "Transverse momentum and collision energy dependence of high p_{T} hadron suppression in Au+Au collisions at ultrarelativistic energies," *Phys. Rev. Lett.*, vol. 91, p. 172302, 2003.

[30] C. Adler and others (**STAR** Collaboration), "Centrality dependence of high p_T hadron suppression in Au+Au collisions at $\sqrt{s_{NN}}$ = 130-GeV," *Phys. Rev. Lett.*, vol. 89, p. 202301, 2002.

[31] K. Aamodt and others (**ALICE** Collaboration), "Suppression of Charged Particle Production at Large Transverse Momentum in Central Pb-Pb Collisions at $\sqrt{s_{\mathrm{NN}}}$ = 2.76 TeV," *Phys. Lett.*, vol. B696, pp. 30–39, 2011.

[32] B. Abelev and others (**ALICE** Collaboration), "Centrality Dependence of Charged Particle Production at Large Transverse Momentum in Pb–Pb Collisions at $\sqrt{s_{\mathrm{NN}}}$ = 2.76 TeV," *Phys. Lett.*, vol. B720, pp. 52–62, 2013.

[33] S. Chatrchyan and others (**CMS** Collaboration), "Study of high-p_{T} charged particle suppression in PbPb compared to pp collisions at $\sqrt{s_{\mathrm{NN}}}$ = 2.76 TeV," *Eur. Phys. J.*, vol. C72, p. 1945, 2012.

[34] G. Aad and others (**ATLAS** Collaboration), "Measurement of charged-particle spectra in Pb+Pb collisions at $\sqrt{s_{\mathrm{NN}}}$ = 2.76 TeV with the ATLAS detector at the LHC," *JHEP*, vol. 09, p. 050, 2015.

[35] S. Navin, "Diffraction in Pythia," *LUTP-09-23, MCNET-10-09*, 2010.

[36] P. Collins, "An introduction to Regge theory and high energy physics," *Phys. Rep.*, vol. 50, p. 157, 1979.

[37] M. Deile and others (**TOTEM** Collaboration), "Diffraction and total cross-section at the Tevatron and the LHC," *Springer Proc. Phys.*, vol. 108, pp. 40–45, 2006.

[38] R. D. Weller and P. Romatschke, "One fluid to rule them all: viscous hydrodynamic description of event-by-event central p+p, p+Pb and Pb+Pb collisions at $\sqrt{s}$ = 5.02 TeV," *Phys. Lett.*, vol. B774, pp. 351–356, 2017.

[39] G. Aad and others (**ATLAS** Collaboration), "Observation of Long-Range Elliptic Azimuthal Anisotropies in $\sqrt{s}$ =13 and 2.76 TeV pp Collisions with the ATLAS Detector," *Phys. Rev. Lett.*, vol. 116, no. 17, p. 172301, 2016.

[40] V. Khachatryan and others (**CMS** Collaboration), "Evidence for collectivity in pp collisions at the LHC," *Phys. Lett.*, vol. B765, pp. 193–220, 2017.

[41] B. Abelev and others (**ALICE** Collaboration), "Long-range angular correlations on the near and away side in p-Pb collisions at $\sqrt{s_{\mathrm{NN}}}$ = 5.02 TeV," *Phys. Lett.*, vol. B719, pp. 29–41, 2013.

[42] A. Adare and others (**PHENIX** Collaboration), "Quadrupole Anisotropy in Dihadron Azimuthal Correlations in Central d+Au Collisions at $\sqrt{s_{\mathrm{NN}}}$ = 200 GeV," *Phys. Rev. Lett.*, vol. 111, no. 21, p. 212301, 2013.

[43] B. Alver and others (**PHOBOS** Collaboration), "System size dependence of cluster properties from two-particle angular correlations in Cu+Cu and Au+Au collisions at $\sqrt{s_{\mathrm{NN}}}$ = 200-GeV," *Phys. Rev.*, vol. C81, p. 024904, 2010.

[44] S. Chatrchyan and others (**CMS** Collaboration), "Long-range and short-range dihadron angular correlations in central PbPb collisions at a nucleon-nucleon center of mass energy of 2.76 TeV," *JHEP*, vol. 07, p. 076, 2011.

[45] J. Adam and others (**ALICE** Collaboration), "Enhanced production of multi-strange hadrons in high-multiplicity proton-proton collisions," *Nature Phys.*, vol. 13, pp. 535–539, 2017.

[46] A. Ortiz Velasquez, P. Christiansen, E. Cuautle Flores, I. Maldonado Cervantes, and G. Paić, "Color Reconnection and Flowlike Patterns in *pp* Collisions," *Phys. Rev. Lett.*, vol. 111, no. 4, p. 042001, 2013.

[47] T. Sjöstrand, "Status and developments of event generators," *PoS*, vol. LHCP2016, p. 007, 2016.

[48] T. Sjostrand and P. Z. Skands, "Transverse-momentum-ordered showers and interleaved multiple interactions," *Eur. Phys. J.*, vol. C39, pp. 129–154, 2005.

[49] S. Höche, "Introduction to parton-shower event generators," in *Proceedings, Theoretical Advanced Study Institute in Elementary Particle Physics: Journeys Through the Precision Frontier: Amplitudes for Colliders (TASI 2014): Boulder, Colorado, June 2-27, 2014*, 2015, pp. 235–295.

[50] T. Sjostrand and P. Z. Skands, "Multiple interactions and the structure of beam remnants," *JHEP*, vol. 03, p. 053, 2004.

[51] S. Argyropoulos and T. Sjöstrand, "Effects of color reconnection on $t\bar{t}$ final states at the LHC," *JHEP*, vol. 11, p. 043, 2014.

[52] C. Albajar *et al.*, "A study of the general characteristics of proton - antiproton collisions at $\sqrt{s}$=0.2 to 0.9 TeV," *Nuclear Physics B*, vol. 335, no. 2, pp. 261 – 287, 1990. [Online]. Available: http://www.sciencedirect.com/science/article/pii/055032139090493W

[53] G. Gustafson, "Multiple Interactions, Saturation, and Final States in pp Collisions and DIS," *Acta Phys. Polon.*, vol. B40, pp. 1981–1996, 2009.

[54] T. Sjostrand, S. Mrenna, and P. Z. Skands, "PYTHIA 6.4 Physics and Manual," *JHEP*, vol. 05, p. 026, 2006.

[55] Sjostrand, Torbjorn and Mrenna, Stephen and Skands, Peter Z., "A Brief Introduction to PYTHIA 8.1," *Comput. Phys. Commun.*, vol. 178, pp. 852–867, 2008.

[56] P. Skands, S. Carrazza, and J. Rojo, "Tuning PYTHIA 8.1: the Monash 2013 Tune," *Eur. Phys. J.*, vol. C74, no. 8, p. 3024, 2014.

[57] K. Werner, F.-M. Liu, and T. Pierog, "Parton ladder splitting and the rapidity dependence of transverse momentum spectra in deuteron-gold collisions at RHIC," *Phys. Rev.*, vol. C74, p. 044902, 2006.

[58] H. J. Drescher, M. Hladik, S. Ostapchenko, T. Pierog, and K. Werner, "Parton based Gribov-Regge theory," *Phys. Rept.*, vol. 350, pp. 93–289, 2001.

[59] T. Pierog, I. Karpenko, J. M. Katzy, E. Yatsenko, and K. Werner, "EPOS LHC: Test of collective hadronization with data measured at the CERN Large Hadron Collider," *Phys. Rev.*, vol. C92, no. 3, p. 034906, 2015.

[60] K. Werner, "Core-corona separation in ultra-relativistic heavy ion collisions," *Phys. Rev. Lett.*, vol. 98, p. 152301, 2007.

[61] K. Werner, I. Karpenko, T. Pierog, M. Bleicher, and K. Mikhailov, "Event-by-Event Simulation of the Three-Dimensional Hydrodynamic Evolution from Flux Tube Initial Conditions in Ultrarelativistic Heavy Ion Collisions," *Phys. Rev.*, vol. C82, p. 044904, 2010.

[62] *Design study of the Large Hadron Collider (LHC): a multiparticle collider in the LEP tunnel*, ser. CERN Yellow Reports: Monographs. Geneva: CERN, 1991, the report is replaced by CERN/AC/95-05(LHC). [Online]. Available: http://cds.cern.ch/record/220493

[63] O. S. Brüning, P. Collier, P. Lebrun, S. Myers, R. Ostojic, J. Poole, and P. Proudlock, *LHC Design Report: The LHC Main Ring*, ser. CERN Yellow Reports: Monographs. Geneva: CERN, 2004. [Online]. Available: https://cds.cern.ch/record/782076

[64] M. Benedikt, P. Collier, V. Mertens, J. Poole, and K. Schindl, *LHC Design Report: The LHC Injection Chain*, ser. CERN Yellow Reports: Monographs. Geneva: CERN, 2004. [Online]. Available: http://cds.cern.ch/record/823808

[65] E. Mobs, "The CERN accelerator complex. Complexe des accélérateurs du CERN," Jul 2016, general Photo. [Online]. Available: https://cds.cern.ch/record/2197559

[66] The ALICE Collaboration and K Aamodt and A Abrahantes Quintana and R Achenbach and S Acounis and D Adamová and others, "The ALICE experiment at the CERN LHC," *Journal of Instrumentation*, vol. 3, no. 08, p. S08002, 2008. [Online]. Available: http://stacks.iop.org/1748-0221/3/i=08/a=S08002

[67] K. Aamodt and others (**ALICE** Collaboration), "Centrality dependence of the charged-particle multiplicity density at mid-rapidity in Pb-Pb collisions at $\sqrt{s_{NN}}$ = 2.76 TeV," *Phys. Rev. Lett.*, vol. 106, p. 032301, 2011.

[68] C. H. Christensen, "System-size dependence of the charged-particle pseudorapidity density at $\sqrt{s_{NN}}$ = 5.02 TeV with ALICE," *Nuclear Physics A*, vol. 967, pp. 301 – 304, 2017, the 26th International Conference on Ultra-relativistic Nucleus-Nucleus Collisions: Quark Matter 2017. [Online]. Available: http://www.sciencedirect.com/science/article/pii/S0375947417301914

[69] A. Collaboration, "Definition of the ALICE Coordinate System and Basic Rules for Sub-detector Components Numbering," *ALICE-INT-2003-038*, 2003.

[70] A. Collaboration, F. Carminati, P. Foka, P. Giubellino, A. Morsch, G. Paic, J.-P. Revol, K. Safarík, Y. Schutz, and U. A. Wiedemann, "Alice: Physics performance report, volume i," *Journal of Physics G: Nuclear and Particle Physics*, vol. 30, no. 11, p. 1517, 2004. [Online]. Available: http://stacks.iop.org/0954-3899/30/i=11/a=001

[71] A. Collaboration *et al.*, "Alice: Physics performance report, volume ii," *Journal of Physics G: Nuclear and Particle Physics*, vol. 32, no. 10, p. 1295, 2006. [Online]. Available: http://stacks.iop.org/0954-3899/32/i=10/a=001

[72] B. Abelev *et al.*, "Technical design report for the upgrade of the alice inner tracking system," *CERN-LHCC-2013-024*, 11 2013. [Online]. Available: http://cds.cern.ch/record/1625842

[73] P. Kuijer *et al.*, "The inner tracking system of the alice experiment," *Nuclear Instruments and Methods in Physics Research Section A: Accelerators, Spectrometers, Detectors and Associated*

Equipment, vol. 530, no. 1, pp. 28 – 32, 2004, proceedings of the 6th International Conference on Large Scale Applications and Radiation Hardness of Semiconductor Detectors. [Online]. Available: http://www.sciencedirect.com/science/article/pii/S0168900204010289

[74] G. Dellacasa and others (**ALICE** Collaboration), "Alice time projection chamber: Technical design report," *CERN-LHCC-2000-001*, 2000. [Online]. Available: https://cds.cern.ch/record/451098

[75] A. Matyja *et al.*, "ALICE TPC-design and performance," *Proceedings of Science*, 01 2009.

[76] J. Alme *et al.*, "The ALICE TPC, a large 3-dimensional tracking device with fast readout for ultra-high multiplicity events," *Nuclear Instruments and Methods in Physics Research A*, vol. 622, pp. 316–367, Oct. 2010.

[77] M. Benedikt, P. Collier, V. Mertens, J. Poole, and K. t. C. Schindl, *ALICE forward detectors: FMD, TO and VO: Technical Design Report*, ser. Technical Design Report ALICE. Geneva: CERN, 2004. [Online]. Available: https://cds.cern.ch/record/781854

[78] R. Frühwirth, "Application of kalman filtering to track and vertex fitting," *Nuclear Instruments and Methods in Physics Research Section A: Accelerators, Spectrometers, Detectors and Associated Equipment*, vol. 262, no. 2, pp. 444 – 450, 1987. [Online]. Available: http://www.sciencedirect.com/science/article/pii/0168900287908874

[79] B. B. Abelev and others (**ALICE** Collaboration), "Performance of the ALICE Experiment at the CERN LHC," *Int. J. Mod. Phys.*, vol. A29, p. 1430044, 2014.

[80] K Aamodt and others (**ALICE** Collaboration), "The ALICE experiment at the CERN LHC," *Journal of Instrumentation*, vol. 3, no. 08, p. S08002, 2008. [Online]. Available: http://stacks.iop.org/1748-0221/3/i=08/a=S08002

[81] K. Aamodt and others (**ALICE** Collaboration), "The ALICE definition of primary particles," *ALICE-PUBLIC-2017-005*, Jun 2017. [Online]. Available: https://cds.cern.ch/record/2270008

[82] **ALICE** Collaboration, "ALICE Data taking logbook." [Online]. Available: https://alice-logbook.cern.ch/logbook/

[83] ——, "Reconstructed Run-2 data taking periods." [Online]. Available: https://twiki.cern.ch/twiki/bin/viewauth/ALICE/AliDPGReconstructedDataTakingPeriodsSummary

[84] R. Brun, F. Bruyant, F. Carminati, S. Giani, M. Maire, A. McPherson, G. Patrick, and L. Urban, "GEANT Detector Description and Simulation Tool," 1994.

[85] **ALICE** Collaboration, "Trigger and interaction cross-sections." [Online]. Available: https://twiki.cern.ch/twiki/bin/viewauth/ALICE/EventNormalization#proton_proton_at_sqrt_s_2_76_TeV

[86] J. Otwinowski *et al.*, "pp reference spectra," *ALICE Analysis Note*. [Online]. Available: https://alice-notes.web.cern.ch/node/188

[87] E. Perez Lezama *et al.*, "Transverse momentum spectra of inclusive charged hadrons in pp collisions at $\sqrt{s}$ = 5.02 TeV," *ALICE Analysis Note.* [Online]. Available: https://alice-notes.web.cern.ch/node/472

[88] J. Gronefeld *et al.*, "Transverse momentum spectra of inclusive charged hadrons in pp collisions at $\sqrt{s}$ = 13 TeV," *ALICE Analysis Note.* [Online]. Available: https://alice-notes.web.cern.ch/node/415

[89] ——, "Transverse momentum spectra and nuclear modification factor for charged hadrons in Pb–Pb collisions at $\sqrt{s_{\mathrm{NN}}}$ = 5.02 TeV," *ALICE Analysis Note.* [Online]. Available: https://alice-notes.web.cern.ch/node/473

[90] D. Colella, "ALICE ITS: the Run 1 to Run 2 transition and recent operational experience," in *24th International Workshop on Vertex Detectors (VERTEX2015)*, 2015, p. 3.

[91] M. Ivanov, "Private Communication ."

[92] B. Abelev and others (**ALICE** Collaboration), "Centrality Dependence of Charged Particle Production at Large Transverse Momentum in Pb–Pb Collisions at $\sqrt{s_{\mathrm{NN}}}$ = 2.76 TeV," *Phys. Lett.*, vol. B720, pp. 52–62, 2013.

[93] B. B. Abelev and others (**ALICE** Collaboration), "Production of $\Sigma(1385)^{\pm}$ and $\Xi(1530)^0$ in proton-proton collisions at $\sqrt{s}$ = 7 TeV," *Eur. Phys. J.*, vol. C75, no. 1, p. 1, 2015.

[94] J. Adam and others (**ALICE** Collaboration), "Measurement of pion, kaon and proton production in proton–proton collisions at $\sqrt{s}$ = 7 TeV," *Eur. Phys. J.*, vol. C75, no. 5, p. 226, 2015.

[95] A. A. Bylinkin and A. A. Rostovtsev, "Parametrization of the shape of hadron-production spectra in high-energy particle interactions," *Physics of Atomic Nuclei*, vol. 75, no. 8, pp. 999–1005, Aug 2012. [Online]. Available: https://doi.org/10.1134/S1063778812040047

[96] D. de Florian, M. Epele, R. J. Hernandez-Pinto, R. Sassot, and M. Stratmann, "Parton-to-Kaon Fragmentation Revisited," *Phys. Rev.*, vol. D95, no. 9, p. 094019, 2017.

[97] P. Huhn, "Datenbasierte Effizienzkorrektur zum Nachweis geladener Teilchen im ALICE Experiment," *Johann Wolfgang Goethe-Universität Frankfurt am Main*, Master Thesis, 2017.

[98] F. Sozzi, "Private Communication ."

[99] A. Jaroslav and others (**ALICE** Collaboration), "ALICE luminosity determination for pp collisions at $\sqrt{s}$ = 13 TeV," Jun 2016. [Online]. Available: https://cds.cern.ch/record/2160174

[100] B. Abelev and others (**ALICE** Collaboration), "Measurement of inelastic, single- and double-diffraction cross sections in proton–proton collisions at the LHC with ALICE," *Eur. Phys. J.*, vol. C73, no. 6, p. 2456, 2013.

[101] J. Adam and others (**ALICE** Collaboration), "ALICE luminosity determination for pp collisions at $\sqrt{s}$ = 5 TeV," Jul 2016. [Online]. Available: https://cds.cern.ch/record/2202638

[102] C. Loizides, J. Kamin, and D. d'Enterria, "Improved Monte Carlo Glauber predictions at present and future nuclear colliders," *Phys. Rev.*, vol. C97, no. 5, p. 054910, 2018.

[103] K. Koch and others (**ALICE** Collaboration), "π^0 and η measurement with photon conversions in ALICE in proton-proton collisions at $\sqrt{s}$ = 7 TeV," *Nucl. Phys.*, vol. A855, pp. 281–284, 2011.

[104] S. Acharya and others (**ALICE** Collaboration), "Transverse momentum spectra and nuclear modification factors of charged particles in pp, p-Pb and Pb-Pb collisions at the LHC," *JHEP*, vol. 11, p. 013, 2018.

[105] S. Acharya and others (**ALICE** Collaboration), "Transverse momentum spectra and nuclear modification factors of charged particles in Xe-Xe collisions at $\sqrt{s_{\mathrm{NN}}}$ = 5.44 TeV," *arXiv:1805.04399*, 2018.

[106] B. B. Abelev and others (**ALICE** Collaboration), "Energy Dependence of the Transverse Momentum Distributions of Charged Particles in pp Collisions Measured by ALICE," *Eur. Phys. J.*, vol. C73, no. 12, p. 2662, 2013.

[107] M. Knichel, "Transverse momentum distributions of primary charged particles in pp, p–Pb and Pb–Pb collisions measured with ALICE at the LHC," *Technishe Universität Darmstadt*, PhD Thesis, 2014.

[108] J. Adam and others (**ALICE** Collaboration), "Pseudorapidity and transverse-momentum distributions of charged particles in proton–proton collisions at $\sqrt{s}$ = 13 TeV," *Phys. Lett.*, vol. B753, pp. 319–329, 2016.

[109] R. Hagedorn, "Multiplicities, p_T Distributions and the Expected Hadron $\rightarrow$ Quark - Gluon Phase Transition," *Riv. Nuovo Cim.*, vol. 6N10, pp. 1–50, 1983.

[110] K. Aamodt and others (**ALICE** Collaboration), "Transverse momentum spectra of charged particles in proton-proton collisions at $\sqrt{s}$ = 900 GeV with ALICE at the LHC," *Phys. Lett.*, vol. B693, pp. 53–68, 2010.

[111] V. Khachatryan and others (**CMS** Collaboration), "Transverse momentum and pseudorapidity distributions of charged hadrons in pp collisions at $\sqrt{s}$ = 0.9 and 2.36 TeV," *JHEP*, vol. 02, p. 041, 2010.

[112] C. Albajar *et al.*, "A study of the general characteristics of proton-antiproton collisions at $\sqrt{s}$ =0.2 to 0.9 tev," *Nuclear Physics B*, vol. 335, no. 2, pp. 261 – 287, 1990. [Online]. Available: http://www.sciencedirect.com/science/article/pii/055032139090493W

[113] T. Alexopoulos *et al.*, "Multiplicity dependence of transverse momentum spectra of centrally produced hadrons in pp collisions at 0.3, 0.54, 0.9, and 1.8 TeV center of mass energy," *Physics Letters B*, vol. 336, no. 3, pp. 599 – 604, 1994. [Online]. Available: http://www.sciencedirect.com/science/article/pii/0370269394905789

[114] F. Abe and others (**CDF** Collaboration), "Transverse Momentum Distributions of Charged Particles Produced in $\bar{p}p$ Interactions at $\sqrt{s}$ = 630 GeV and 1800 GeV," *Phys. Rev. Lett.*, vol. 61, p. 1819, 1988.

[115] A. Rossi, G. Vannini, A. Bussière, E. Albini, D. D'Alessandro, and G. Giacomelli, "Experimental study of the energy dependence in proton-proton inclusive reactions,"

Nuclear Physics B, vol. 84, no. 2, pp. 269 – 305, 1975. [Online]. Available: http://www.sciencedirect.com/science/article/pii/0550321375903077

[116] K. Aamodt and others (**ALICE** Collaboration), "Charged-particle multiplicity measurement in proton-proton collisions at $\sqrt{s} = 0.9$ and 2.36 TeV with ALICE at LHC," *Eur. Phys. J.*, vol. C68, pp. 89–108, 2010.

[117] J. Adam and others (**ALICE** Collaboration), "Charged-particle multiplicities in proton–proton collisions at $\sqrt{s} = 0.9$ to 8 TeV," *Eur. Phys. J.*, vol. C77, no. 1, p. 33, 2017.

[118] J. Gronefeld, "Transverse Momentum Distributions and Nuclear Modification in Heavy-Ion Collisions with ALICE at the LHC," *Technishe Universität Darmstadt*, PhD Thesis, 2018.

[119] K. Aamodt and others (**ALICE** Collaboration), "Centrality determination in heavy ion collisions," Aug 2018. [Online]. Available: https://cds.cern.ch/record/2636623

[120] A. Adare and others (**PHENIX** Collaboration), "Scaling properties of fractional momentum loss of high-p_T hadrons in nucleus-nucleus collisions at $\sqrt{s_{NN}}$ from 62.4 GeV to 2.76 TeV," *Phys. Rev.*, vol. C93, no. 2, p. 024911, 2016.

[121] S. Chatrchyan and others (**CMS** Collaboration), "Measurement of the pseudorapidity and centrality dependence of the transverse energy density in PbPb collisions at $\sqrt{s_{NN}} = 2.76$ TeV," *Phys. Rev. Lett.*, vol. 109, p. 152303, 2012.

[122] M. Djordjevic, D. Zigic, M. Djordjevic, and J. Auvinen, "How to test path-length dependence in energy loss mechanisms: analysis leading to a new observable," *arXiv:1805.04030*, 2018.

Appendices

Appendix A

Data and MC

***

pp at $\sqrt{s}$ = 2.76 TeV

Data (LHC11a pass4)

146746, 146747, 146748, 146801, 146802, 146803, 146804, 146805, 146806, 146807, 146817, 146824, 146856, 146858, 146859, 146860

MC (LHC12f1a)

146746, 146747, 146748, 146801, 146802, 146803, 146804, 146805, 146806, 146807, 146817, 146824, 146856, 146858, 146859, 146860

pp at $\sqrt{s}$ = 7 TeV

Data (LHC10d pass2)

122374, 122375, 124751, 125023, 125085, 125097, 125100, 125134, 125296, 125630, 125632, 125633, 125842, 125843, 125844, 125847, 125848, 125849, 125850, 125851, 125855, 126004, 126007, 126008, 126073, 126078, 126081, 126082, 126088, 126090, 126097, 126158, 126160, 126168, 126283, 126284, 126285, 126351, 126352, 126359, 126403, 126404, 126405, 126406, 126407, 126408, 126409, 126422, 126424, 126425, 126432

MC (LHC10f6a)

122374, 122375, 124751, 125023, 125085, 125097, 125100, 125134, 125296, 125630, 125632, 125633, 125842, 125843, 125844, 125847, 125848, 125849, 125850, 125851, 125855, 126004, 126007, 126008, 126073, 126078, 126081, 126082, 126088, 126090, 126097, 126158, 126160, 126168, 126283, 126284, 126285, 126351, 126352, 126359, 126403, 126404, 126405, 126406, 126407, 126408, 126409, 126422, 126424, 126425, 126432

pp at $\sqrt{s}$ = 5.02 TeV

Data (LHC15n pass3)

244340, 244343, 244351, 244355, 244359, 244364, 244377, 244411, 244416, 244418, 244421, 244453, 244456, 244480, 244481, 244482, 244483, 244484, 244531, 244540, 244542, 244617, 244618, 244619, 244626, 244627, 244628

MC (LHC16k5a)

244340, 244343, 244351, 244355, 244359, 244364, 244377, 244411, 244416, 244418, 244421, 244453, 244456, 244480, 244481, 244482, 244483, 244484, 244531, 244540, 244542, 244617, 244618, 244619, 244626, 244627, 244628

pp at $\sqrt{s}$ = 13 TeV

Data (LHC15n pass3)

225000, 225011, 225016, 225026, 225031, 225035, 225037, 225041, 225043, 225050, 225051, 225052, 225105, 225106, 225305, 225307, 225309, 225310, 225313, 225314, 225315, 225322, 225576, 225578, 225579, 225580, 225582, 225586, 225587, 225589, 225609, 225611, 225705, 225707, 225708, 225709, 225710, 225716, 225717, 225719, 225753, 225757, 225762, 226062, 226170, 226220, 226225, 226444, 226445, 226452, 226466, 226468, 226472, 226476, 226483, 226495, 226500

MC (LHC15g3c3)

225000, 225011, 225016, 225026, 225031, 225035, 225037, 225041, 225043, 225050, 225051, 225052, 225105, 225106, 225305, 225307, 225309, 225310, 225313, 225314, 225315, 225322, 225576, 225578, 225579, 225580, 225582, 225586, 225587, 225589, 225609, 225611, 225705, 225707, 225708, 225709, 225710, 225716, 225717, 225719, 225753, 225757, 225762, 226062, 226170, 226220, 226225, 226444, 226445, 226452, 226466, 226468, 226472, 226476, 226483, 226495, 226500

Pb-Pb at $\sqrt{s}$ = 5.02 TeV

Data (LHC15o pass1)

245554, 245545, 245544, 245543, 245542, 245540, 245535, 245507, 245505, 245504, 245501, 245497, 245496, 245454, 245452, 245450, 245446, 245441, 245439, 245411, 245409, 245407, 245401, 245397, 245396, 245353, 245349, 245347, 245346, 245345, 245343, 245259

MC (LHC16g1a, LHC16g1b and LHC16g1c)

245554, 245545, 245544, 245543, 245542, 245540, 245535, 245507, 245505, 245504, 245501, 245497, 245496, 245454, 245452, 245450, 245446, 245441, 245439, 245411, 245409, 245407, 245401, 245397, 245396, 245353, 245349, 245347, 245346, 245345, 245343, 245259

Xe-Xe at $\sqrt{s} = 5.44$ TeV

Data (LHC17n pass1)

280234, 280235

MC (LHC17j7)

280234, 280235
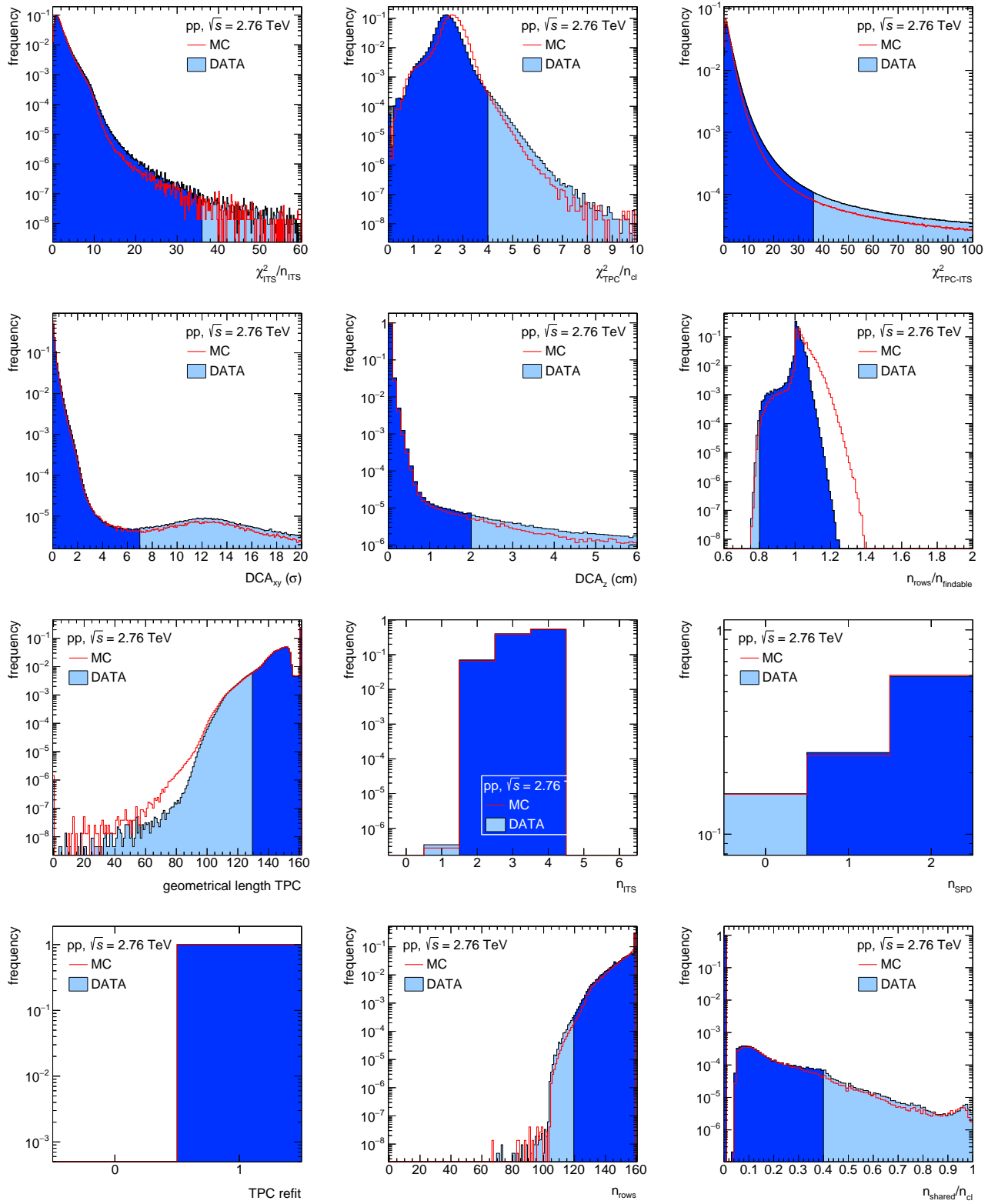
Appendix B

Cut studies

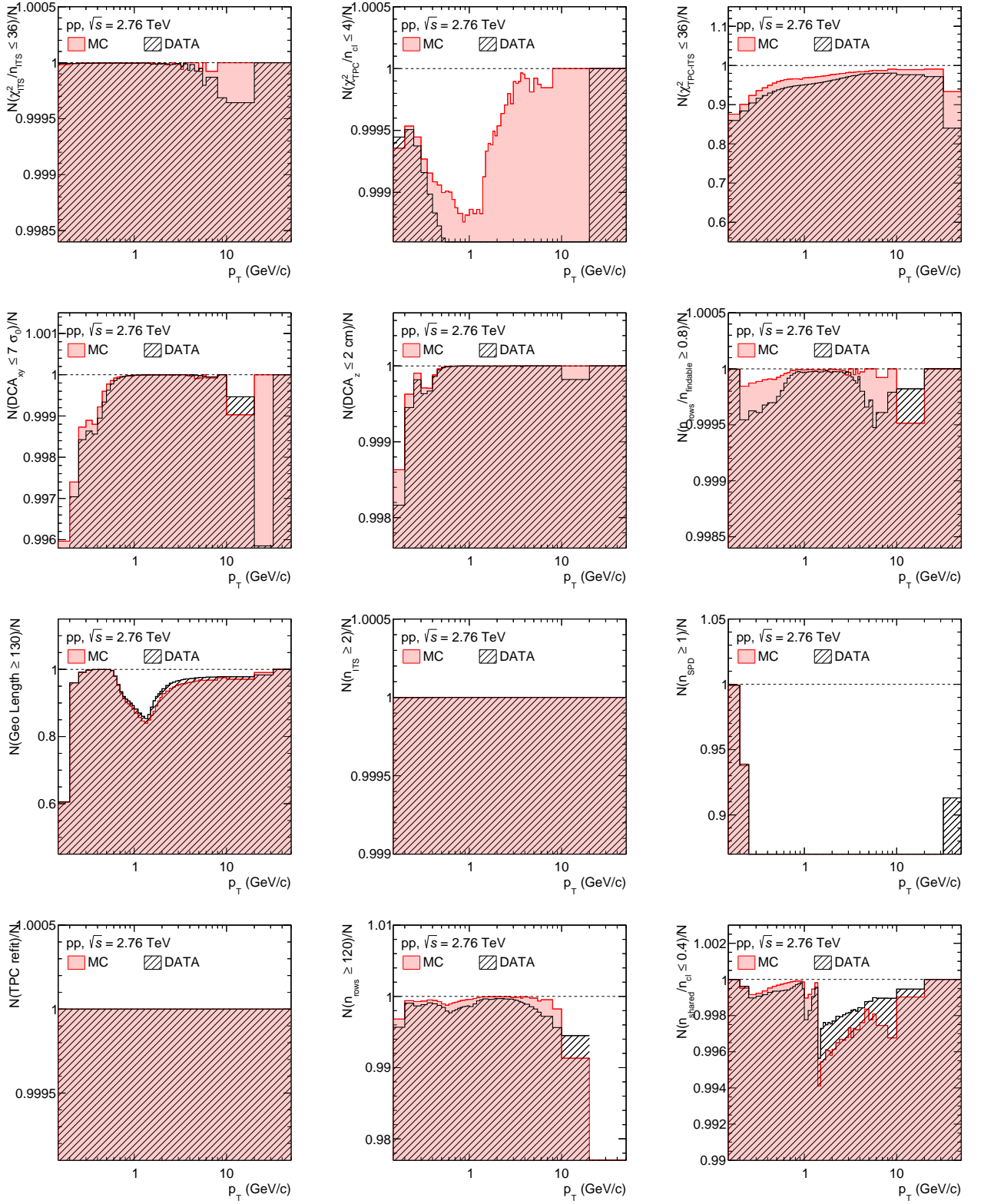Figure B.1: Cut study for pp collisions at $\sqrt{s} = 2.76$ TeV.

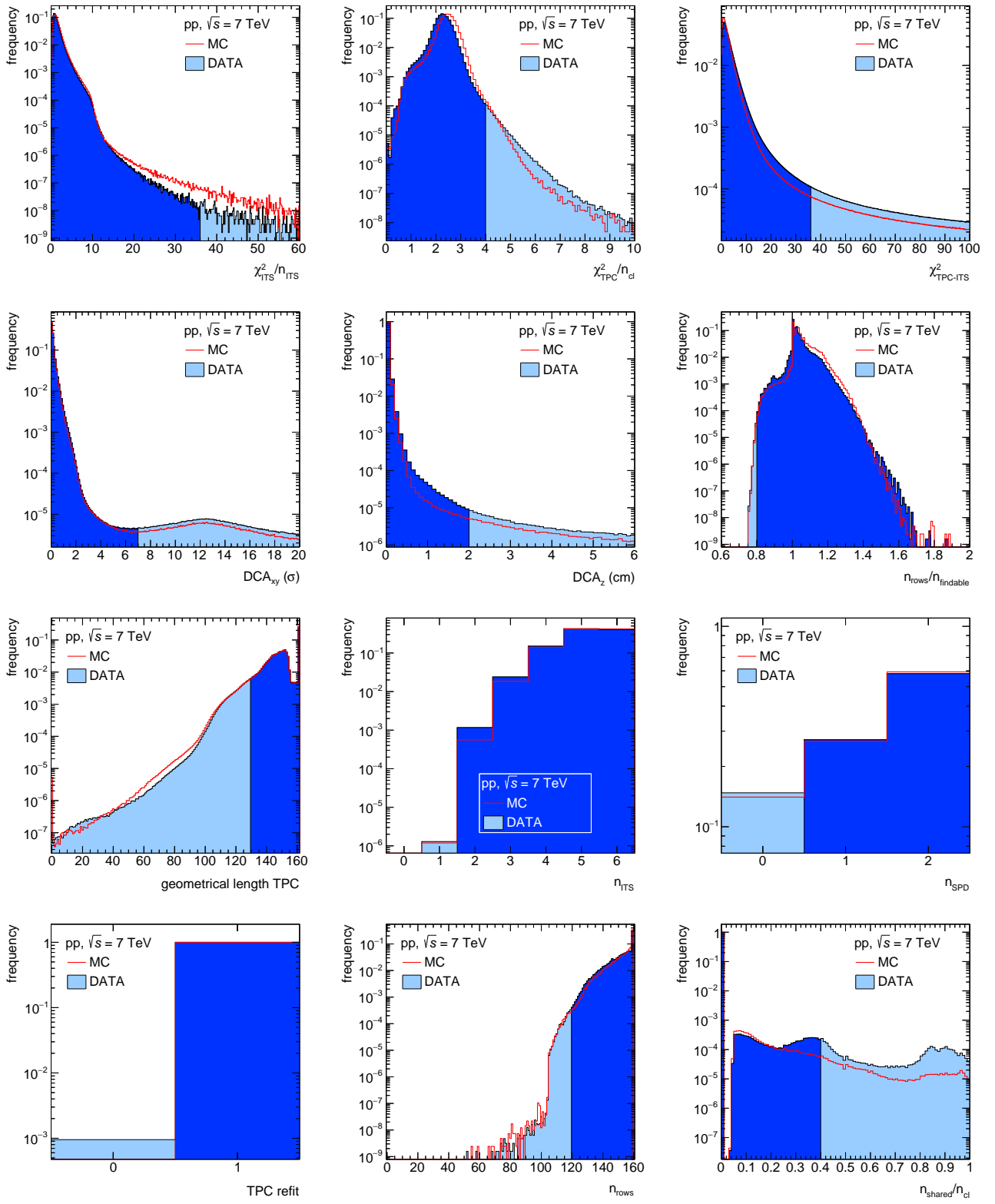Figure B.2: Cut study for pp collisions at $\sqrt{s} = 2.76$ TeV.

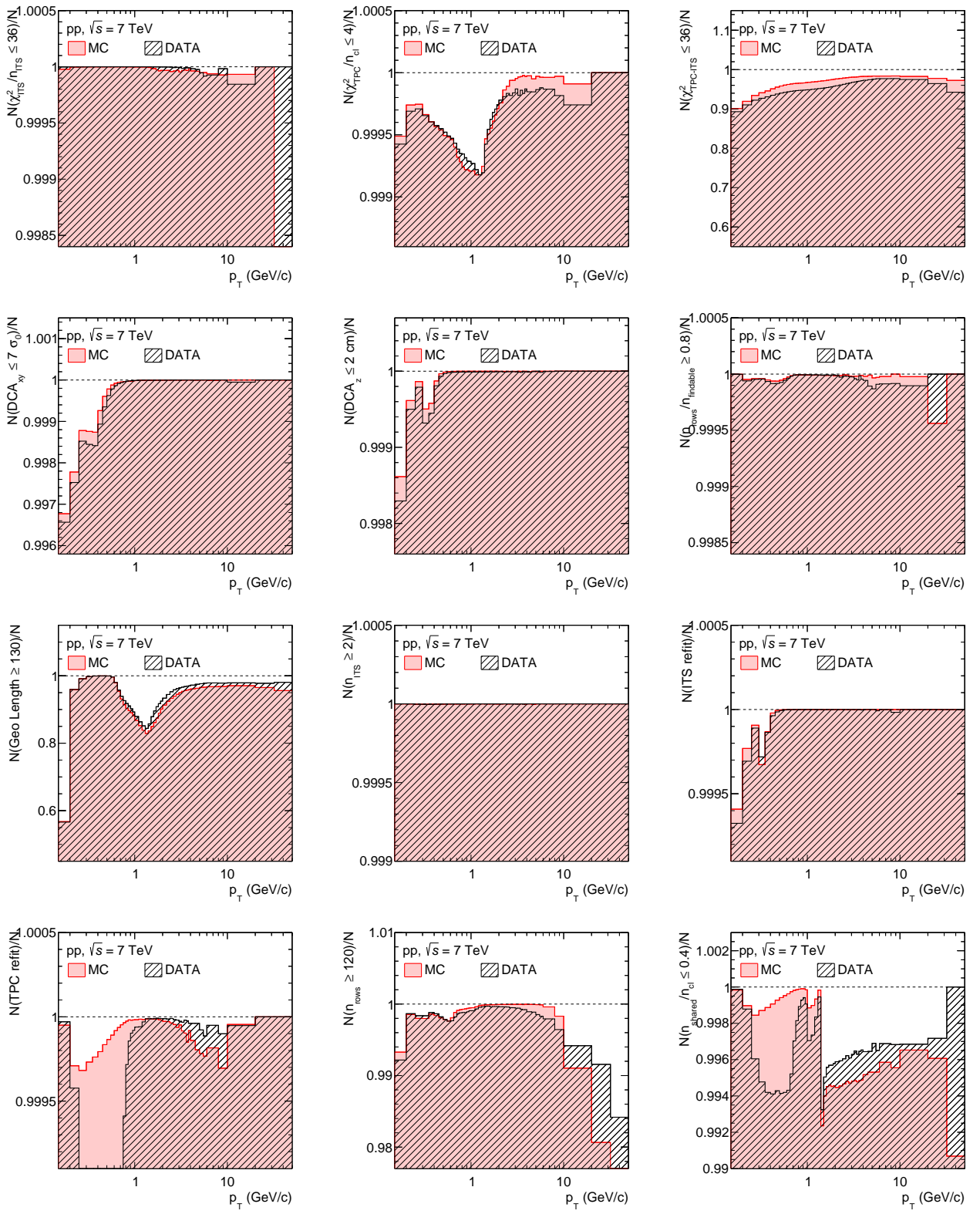Figure B.3: Cut study for pp collisions at $\sqrt{s} = 7$ TeV.

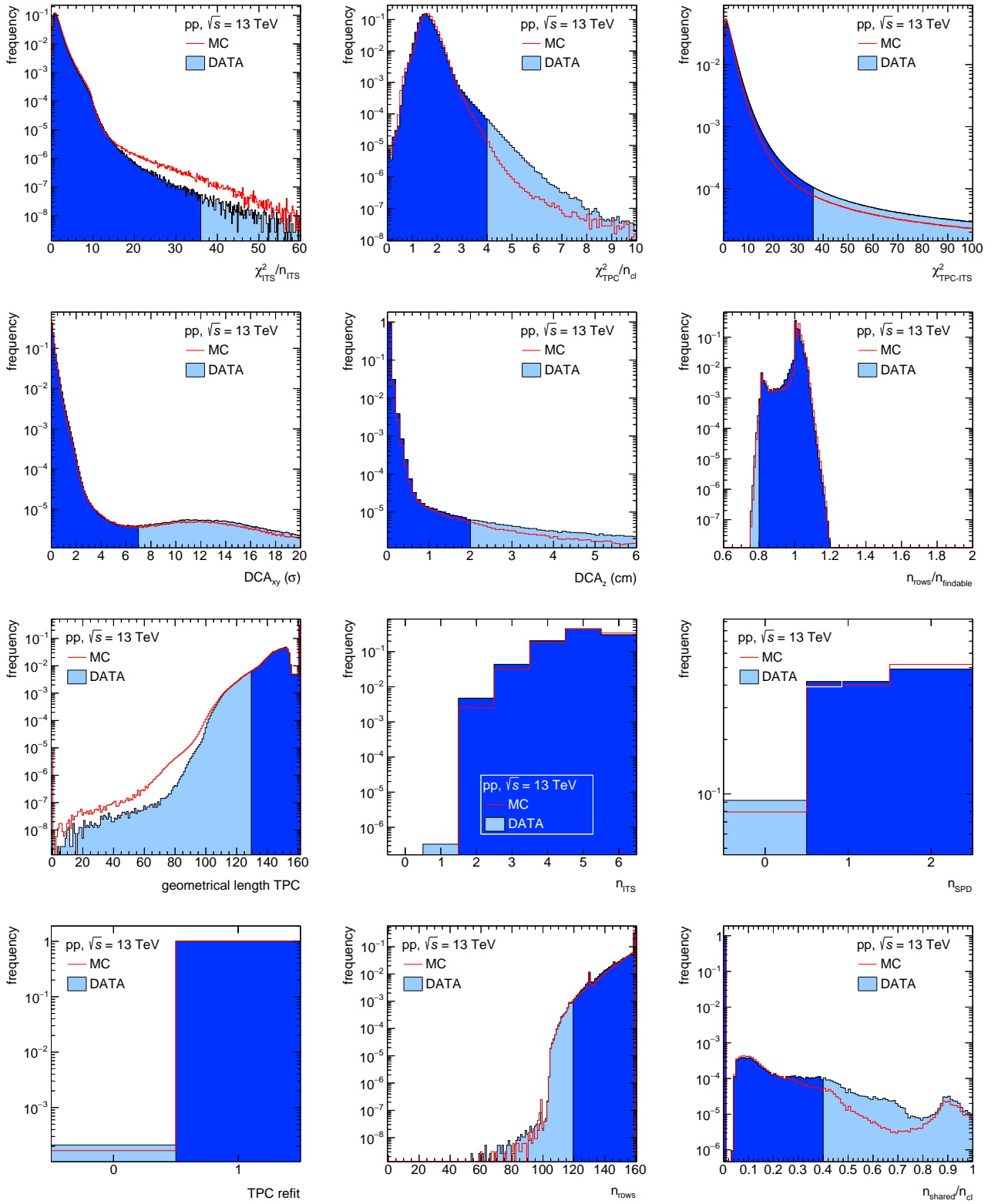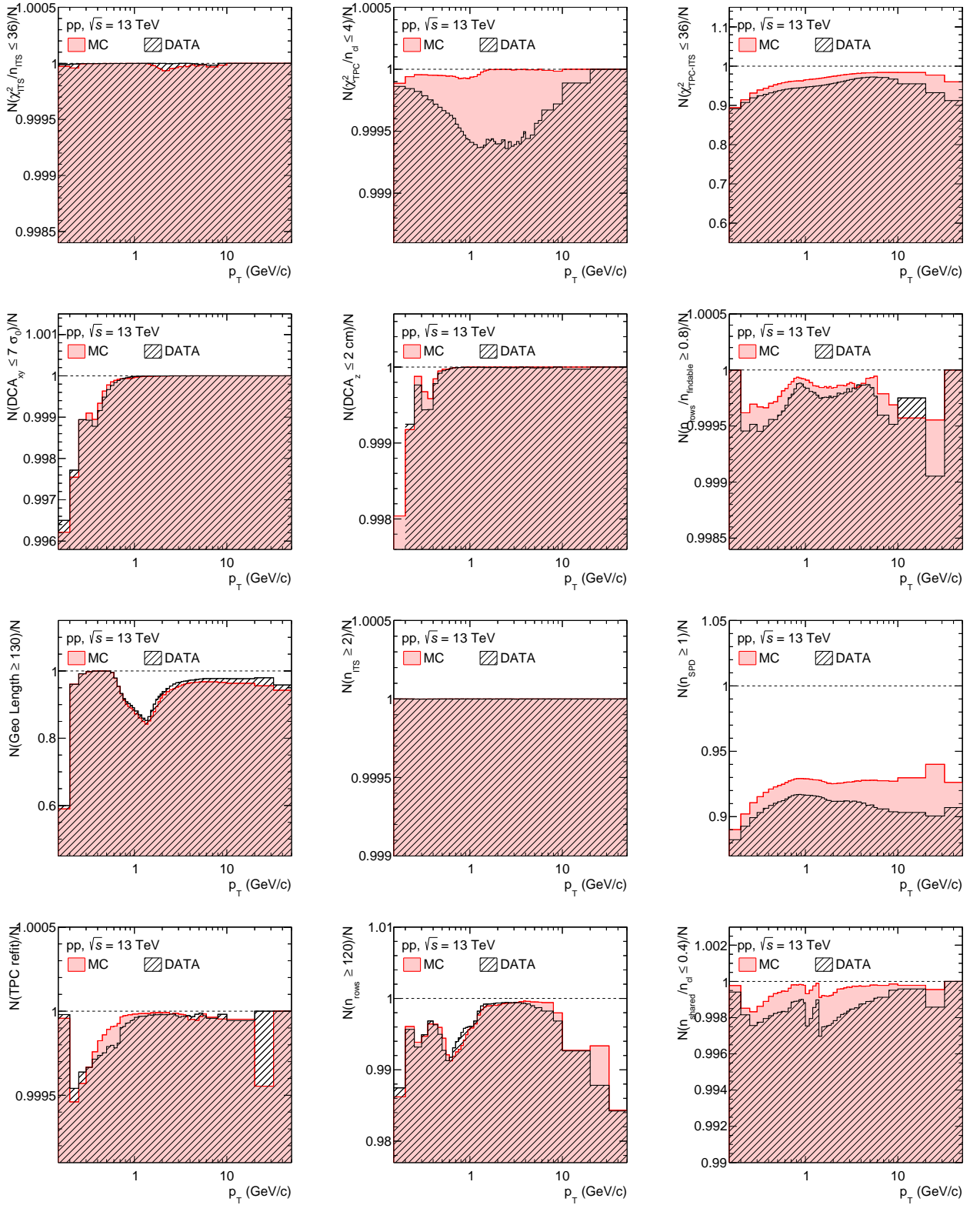Figure B.4: Cut study for pp collisions at $\sqrt{s}$ = 7 TeV.

Figure B.5: Cut study for pp collisions at $\sqrt{s} = 13$ TeV.

Figure B.6: Cut study for pp collisions at $\sqrt{s} = 13$ TeV.

Curriculum Vitae

Edgar Perez Lezama
May 18th 1988, Tehuacán Puebla, Mexico

Education

Since Oct 2016	Awarded with the Giersch-Excellence-Grant 2016 in recognition of outstanding achievements in the doctoral thesis.
Since Feb 2015	Member of HGS-HIRe graduate school.
Since Jan 2015	**PhD**, Institut für Kernphysik, Goethe-Universitt Frankfurt, Germany. **Title**: Transverse momentum of charged particles in proton-proton collisions measured with the ALICE experiment. **GPA**:
Feb 2012-Oct2014	**Master of Science**, Instituto de Ciencias Nucleares, UNAM. **Title**: Measurement of $\phi(1020)$ resonance production in p-Pb collisions at $\sqrt{s_{NN}} = 5.02$ TeV with the ALICE experiment. **GPA**: 9.4 out of 10.0
Aug 2006-Jan 2012	**Bachelor of Science**, Facultad de Ciencias, UNAM. **Title**: Evolution of event shape variables in pp collision in the ALICE experiment. **GPA**: 9.65 out of 10.0

List of Publications

- ALICE Collaboration, *Pseudorapidity and transverse-momentum distributions of charged particles in proton-proton collisions at $\sqrt{s}$ = 13 TeV*, Phys.Lett. B753 (2016) 319-329

- ALICE Collaboration, *Transverse momentum spectra and the nuclear modification factor of charged particles with ALICE*, J. Phys.: Conf. Ser. 832 012009

- ALICE Collaboration, *Transverse momentum spectra and nuclear modification factors of charged particles measured in Pb-Pb coollisions at 5.02 TeV with ALICE at the LHC*, arXiv:1802.09145

- ALICE Collaboration, *Transverse momentum distributions and nuclear modification factor in Xe-Xe collisions at $\sqrt{s_{NN}} = 5.44$ TeV*, arXiv:1805.04399

Talks and posters

Jan 2014 Invited Talk at XXXVII Symposium on nuclear physics, Cocoyoc Mexico
Title: Study of the Pythia 8 $\Delta\eta - \Delta\phi$ correlation in function of multiplicity and
transverse sphericity in proton proton collisions at 7 TeV.

Oct 2015 Poster presentation at Quark Matter 2015, Kobe, Japan
Title: Transverse momentum distribution of charged particles in proton-proton
collision at $\sqrt{s}$ =13 TeV.

March 2016 Talk at the Deutsche Physikalische Gesellschaft (DPG), Darmstadt Germany.
Title: Transverse momentum distributions of charged particles in pp
collisions with ALICE at the LHC.

June 2016 Talk at International School Of Subnuclear Physics, Erice-Sicily, Italy.
Title: Transverse momentum distributions of charged-particles in pp
and Pb-Pb collisions at $\sqrt{s_{NN}} = 5.02$ TeV with ALICE.

Sep 2016 Talk at HotQuarks conference, South Padre Island, USA.
Title: Transverse momentum spectra and the nuclear modification factor of
charged particles at $\sqrt{s}$ =5.02 TeV with ALICE.

Feb 2017 Poster presentation at Quark Matter 2017 conference, Chicago, USA.
Title: Transverse momentum spectra of primary charged particles in
pp collisions measured by ALICE at the LHC.

March 2017 Talk at the Deutsche Physikalische Gesellschaft (DPG), Münster Germany.
Title: Transverse momentum distributions of charged-particles in pp
collisions with ALICE at the LHC.

Feb 2018 Talk at the Deutsche Physikalische Gesellschaft (DPG), Bochum Germany.
Title: Transverse momentum distributions of charged particles in pp
and nuclear collisions with ALICE at the LHC.

May 2018 Poster presentation at Quark Matter 2018 conference, Venice, Italy.
Title: Energy dependence of transverse momentum spectra of primary charged
particles in pp collisions measured by ALICE at the LHC.

July 2018 Talk at International Conference on High Energy Physics, Seoul, South-Korea
Title: Transverse momentum distributions of charged particles in pp and nuclear
collisions with ALICE at the LHC.

Acknowledgements